

**Oceanic variability around Madagascar:
connections to the large-scale Indian Ocean
circulation and its forcing**

Virginia Palastanga

ISBN 90-393-4554-2

**Oceanic variability around Madagascar:
connections to the large- scale Indian Ocean
circulation and its forcing**

Oceanvariabiliteit rond Madagascar:
verbanden met de grootschalige circulatie
in de Indische Oceaan en zijn forcering

PROEFSCHRIFT

ter verkrijging van de graad van doctor aan de Universiteit Utrecht
op gezag van de rector magnificus, prof. dr. W. H. Gispen,
ingevolge het besluit van het college voor promoties
in het openbaar te verdedigen op

maandag 4 juni 2007 des middags om 12.45 uur

door

Virginia Palastanga

geboren op 7 januari 1977 te Argentinië

Promotor: Prof. dr. W. P. M. de Ruijter
Co-promotoren: Prof. dr. ir. H. A. Dijkstra
Dr. P. J. van Leeuwen

This research was funded by the Foundation for Earth and Live Sciences (ALW) of the Netherlands Foundation of Scientific Research (NWO).

Contents

1	Introduction	1
1.1	Oceanic circulation and variability	1
1.2	The Indian Ocean	4
1.2.1	General Circulation	4
1.2.2	Climate variability	7
1.3	The variability around Madagascar	9
1.4	Thesis outline	12
2	The wind stress curl over the South Indian Ocean: seasonal and interannual variability	15
2.1	Introduction	15
2.2	Data and Procedures	17
2.2.1	Data	17
2.2.2	Procedures	18
2.3	Seasonal variability of the wind stress curl	18
2.3.1	Large scale wind stress curl	18
2.3.2	Wind stress curl around Madagascar	21
2.4	Low frequency variability of the wind stress curl	24
2.4.1	Tropical climate events in the Indian Ocean	24
2.4.2	Wind stress curl interannual variability	27
2.5	Summary and discussion	36
3	Low-frequency eddy-variability around Madagascar: links to the Indian Ocean variability	39
3.1	Introduction	39
3.2	Data	41
3.3	SSH and EKE variability around Madagascar	42
3.3.1	SSH interannual variations	44
3.3.2	EKE interannual variations	46
3.4	Large-scale response of the SSH to the IOD	48
3.5	Linking the large-scale IO variability and the mesoscale activity around Madagascar	52
3.5.1	Variability of the local flow fields	54

CONTENTS

3.5.2	Impact on the Mozambique Channel eddy activity	56
3.5.3	Connection to the eddy activity south of Madagascar	59
3.6	Summary and discussion	59
4	Flow structure and variability in the Subtropical Indian Ocean	63
4.1	Introduction	63
4.2	Data	65
4.3	SSH variability from altimetry	65
4.4	Mean flow structure	66
4.5	Stability considerations	73
4.6	Summary and discussion	77
5	Non-linear effects on the circulation around an island, with application to Madagascar	81
5.1	Introduction	81
5.2	The model	84
5.3	Island rule formulation	86
5.3.1	Theory	86
5.3.2	Application to the Mozambique Channel throughflow	89
5.4	Model results	90
5.4.1	Initial experiment	90
5.4.2	Sensitivity experiments	92
5.4.3	Analysis of the island rule	96
5.5	Summary and discussion	99
	Bibliography	103
	Summary	111
	Hartelijk bedankt!	115
	Curriculum Vitae	117

Chapter 1

Introduction

1.1 Oceanic circulation and variability

The winds and buoyancy fluxes are two main forcings of the global ocean circulation, inducing the wind driven circulation in the upper thousand meters of the water column and the deep reaching thermohaline circulation. The global oceanic and atmospheric circulations have a crucial role in climate because together they transport heat from the Equator to the Poles to compensate for differential insolation, maintaining the earth's radiation balance. Due to its high heat capacity, the ocean acts as a reservoir, with heat carried by surface currents to specific regions where it is released back to the atmosphere in latent and sensible form. Understanding the natural causes of oceanic variability is, thus, ultimately relevant for climate and climate change detection.

On the global scale, the winds drive ocean currents by transmitting momentum and vorticity to the oceanic surface layer. The general pattern of the mean wind driven circulation is shown in Fig. 1.1. In each ocean basin, the circulation consists of a system of equatorial currents and of closed cells or gyres, except in the Southern Oceans where the Antarctic Circumpolar Current (ACC) flows eastward around the globe. The existence of large-scale gyres in the circulation was first explained by Sverdrup (1947), who showed a relation between the vertically integrated meridional transport in the oceans interior and the curl of the wind stress at the surface. Over regions where the input of vorticity by the wind is negative (positive), the Sverdrup flow is southward (northward), whereas areas of zero wind stress curl correspond to only zonal flow. The subtropical gyres show an anticyclonic circulation in both hemispheres, with a narrow, intense boundary current on the western side compensated by a slow, broad current in the ocean interior. Examples of western boundary currents are the Gulf Stream in the North Atlantic, the Kuroshio in the North Pacific and the Agulhas Current in the South Indian Ocean. In the northern hemisphere subpolar gyres of cyclonic circulation are also observed.

The thermohaline circulation (THC) is driven by spatial variations in the heat and fresh water surface fluxes, and connects all ocean basins forming the so-called 'ocean conveyor' (Broecker, 1991). An important component of the THC is convection and mixing of water masses in regions with great loss of heat and/or fresh water from the ocean to the atmos-

Introduction

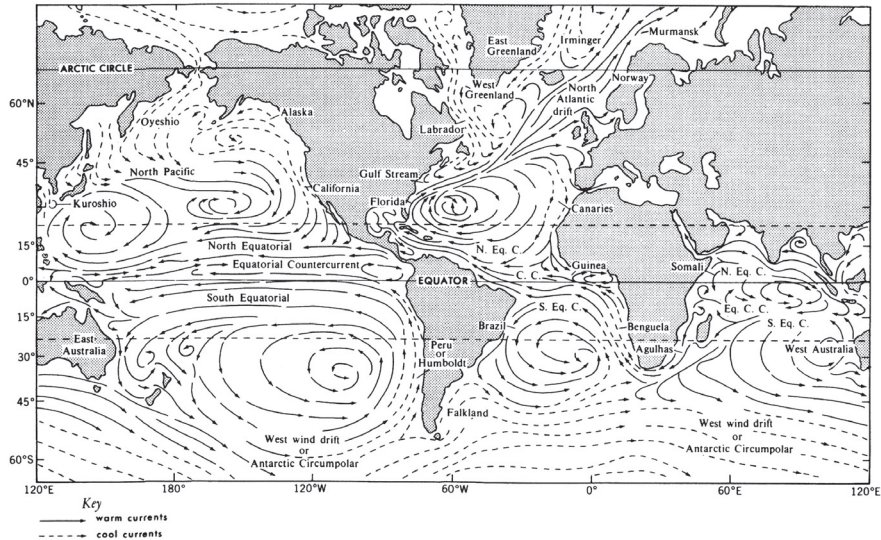


Figure 1.1: Schematic diagram of the global oceans near-surface circulation (from Peixoto and Oort [1992]).

phere. This occurs mainly in the northern North Atlantic, where North Atlantic Deep Water (NADW) is formed, and around the Antarctic continental margins. The NADW spreads southwards in the Atlantic Ocean to join the ACC, from where it enters the other ocean basins and is brought up to the surface by deep upwelling (as sketched in Fig. 1.2). One of the return paths of upper layer waters to the North Atlantic occurs through the Agulhas Current retroflexion around South Africa (Gordon, 1986).

One cause of oceanic variability is direct wind forcing. Non-steady winds generate a broad range of transient phenomena from ripples and gravity waves on the small scales, to long planetary waves that mediate the adjustment of the gyre circulation to variable forcing on the basin scale (Anderson and Gill, 1975). These planetary or Rossby waves are also responsible for the western intensification of the subtropical gyres (Gill, 1982). Rossby waves have been observed in the ocean on a global scale since satellite altimetry data became available (Chelton and Schlax, 1997). They propagate westward with phase speeds of a few centimeters per second, depending on the vertical shear of the mean flow (Killworth et al., 1997). Because of Rossby wave propagation, the variability of the currents over a region is affected by both local and remote wind forcing. In addition, the response of the currents or large-scale sea level to wind forcing is spatially and temporally dependent (Fu and Davidson, 1995). Wind variability on scales larger than 1000 km and periods lower than 300 days force barotropic (depth independent) waves at mid and high latitudes, and thus the sea level variability is a good indicator of the motion in the entire water column. On longer time scales, the response of the ocean is baroclinic, and sea level changes are related to thermocline depth variations. These baroclinic Rossby waves control the ocean response in tropical and extratropical regions (Fu, 2001). For instance, analysis of altimetry data in the subarctic North

Oceanic circulation and variability

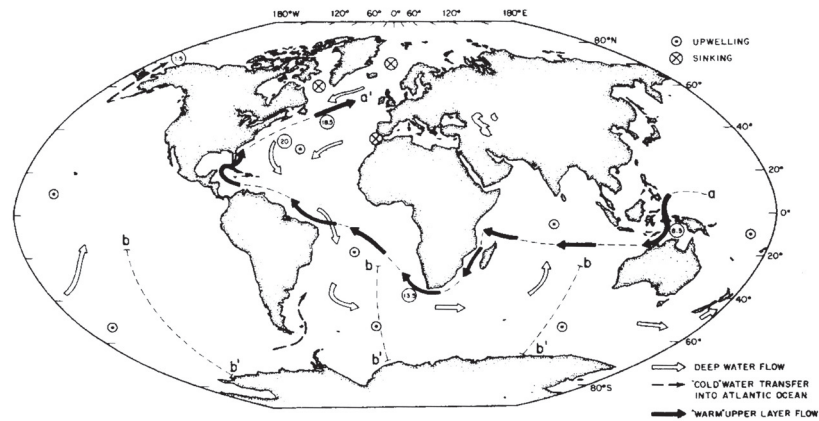


Figure 1.2: Global meridional overturning circulation associated with NADW formation. The warm water route, transporting heat and salt into the Atlantic Ocean, is shown by the solid arrows and indicates a proposed path for return of upper layer water that is required to maintain and export NADW from the Atlantic. After Gordon (1986).

Pacific has identified significant correlations between the large-scale wind stress curl and the sea level variability on annual time scales (Isoguchi and Kawamura, 1997). On interannual time scales, for example, sea level changes along the Kuroshio Extension have been related to the propagation of baroclinic Rossby waves forced by the accumulated effect of the wind stress curl to the east of the current (Qiu, 2002).

A second cause of oceanic variability is related to hydrodynamic instabilities of the mean flow, which constitute the main source of the eddy energy observed throughout the oceans (Gill et al., 1974; Pedlosky, 1987; Wunsch and Stammer, 1995). The ocean's eddy field represents variability with time scales of 20-150 days and spatial scales of 50-500 km. Observations of the eddy variability from satellite altimetry confirm generation of eddies by instabilities and suggest that only in low energy regions can direct atmospheric wind forcing cause eddy formation (Stammer, 1997). In geophysical fluids, two types of hydrodynamic instability are distinguished. The baroclinic instability refers to the conversion of available potential energy in the mean vertical shear into eddy kinetic energy, while barotropic instability implies a transfer to eddies of the kinetic energy in the mean horizontal shear. Simplified models of baroclinic and barotropic instability (Pedlosky, 1987) are quite successful in predicting propagation speeds and growth rates of instabilities consistent with, for example, direct measurements of meanders along the Gulf Stream (Johns, 1988) and the Pacific Equatorial Countercurrent (Philander, 1976). More recently, studies in the Tropical Indian Ocean (Feng and Wijffels, 2003) and the subtropical North and South Pacific (Qiu, 1999; 2003; Qiu and Chen, 2004) found good correlations between the currents instability characteristics and estimates of eddy variability derived from altimetry.

Finally, variability in the ocean may be caused by coupled ocean-atmosphere processes. A prominent example of a mode of ocean-atmosphere coupled variability is El Niño/Southern

Introduction

Oscillation (ENSO). The atmospheric component of ENSO consists of a drop in the pressure difference between Darwin and Tahiti that weakens the trade winds along the equatorial Pacific, while the ocean component is represented by the appearance of warm sea surface temperature (SST) anomalies in the eastern tropical Pacific. In the latter region the SST do not respond passively to wind changes. Because of the upwelling and shallow climatological thermocline there, the ocean's subsurface or thermocline variability forced by basin wind anomalies can strengthen original SST anomalies, which react back onto the atmosphere creating a positive feedback loop between the atmospheric and oceanic variables (Bjerknes, 1969). It is well known that due to atmospheric teleconnections the effects of ENSO are seen almost all over the world (Philander, 1990). In the Indian Ocean, for instance, the summer monsoon is weaker in years following an El Niño (Ropelewski and Halpert, 1987). Oceanic teleconnections from ENSO enter the Indian Ocean by coastal Kelvin waves and Rossby waves propagating through the Indonesian passages (Meyers, 1996; Wijffels and Meyers, 2004). On the other hand, the ocean could control the low frequency (interdecadal) variability of ENSO via Pacific oceanic teleconnections from midlatitudes to the tropics (e.g. Galanti and Tziperman, 2003).

1.2 The Indian Ocean

The Indian Ocean is special in several ways. Situated directly west of the Pacific Ocean, the influence of ENSO is strongly felt, both by atmospheric teleconnections and by direct oceanic inflow through the Indonesian Throughflow. Furthermore, all heat it gains through this throughflow and from the atmosphere has to leave the Indian basin in the south, mainly in the southwest corner. And lastly, it plays a very important role in the global 'ocean conveyor' by transporting both warm surface waters from the Pacific and the waters that have upwelled in the Indian Ocean itself, back into the Atlantic Ocean, partly compensating for the NADW flow out of the Atlantic. This interocean transport is situated near the southern tip of the African continent, where the Agulhas Current retroflects eastward and sheds large Agulhas rings into the South Atlantic. The characteristics of these phenomena depend on both the large-scale circulation in the Indian Ocean, and on its variability.

1.2.1 General Circulation

The surface currents in the Indian Ocean north of 10°S exhibit unique seasonal reversals due to the wind variability of the Indian monsoon (see Schott and McCreary, 2001 for a review). The variations in the wind system during the monsoon seasons can be followed from the climatological sea level pressure fields shown in Fig.1.3. In January, high-pressure systems lie over the Asian continent and in the central subtropical Indian Ocean, separated by a region of equatorial lows (Fig. 1.3a). These induce winds from the northeast over the North Indian Ocean, while in the South Indian Ocean the southeast trades extend north up to 15°S . In July, the low-pressure systems over South Africa and Australia disappear and a continuous belt of high pressures is formed, which induces the Indian subtropical high to be stronger and with its center shifted westward (Fig. 1.3b). Consequently, the trades become stronger and extend from 30°S to 5°S in boreal summer. In particular, between 5° - 10°S they are stronger west of

The Indian Ocean

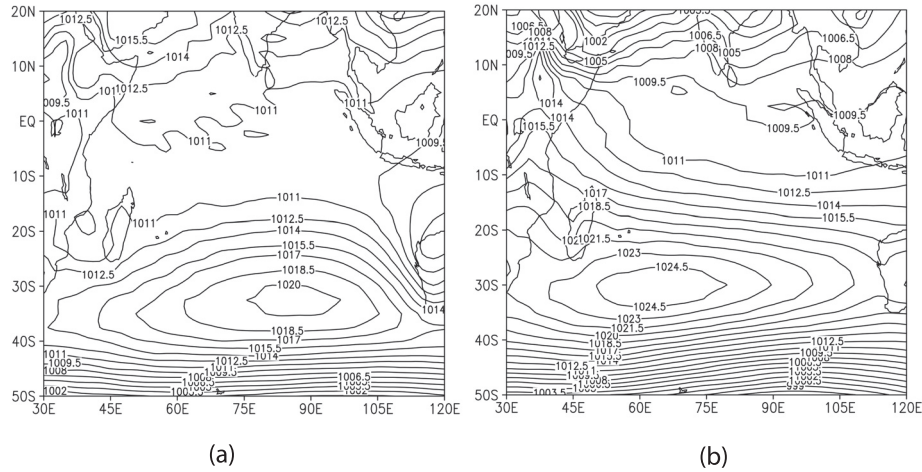


Figure 1.3: Climatological mean sea level pressure in the Indian Ocean from the NCEP Reanalysis data set (Kalnay et al., 1996) for a) January and b) July. Units in mb.

60°E, they deflect to the east near the Equator, and finally turn southwest north of the Equator (Tchernia, 1980). Over the North Indian Ocean the winds are (from the) southwest due to the influence of the summer monsoon.

A scheme of the oceanic surface currents in both seasons is shown in Fig.1.4. The South Equatorial Current (SEC) flows westward between 10°-20°S; driven by the trades throughout the year, it is expected to be stronger and shifted northward in summer. Observations of winds and upper ocean currents showed that the SEC consists of a basic geostrophic current of little seasonal variation, with an additional small Ekman component in summer (Hastenrath and Greischar, 1991). The SEC splits at the eastern Madagascar coast into the North and East Madagascar Currents (NMC and EMC). Hydrographic measurements of these currents did not detect any significant seasonal variation (Swallow et al., 1988; Schott et al., 1988). Only in boreal winter does the current pattern in the tropical Indian Ocean resemble that in other ocean basins. Then, the two westward equatorial currents are separated by the South Equatorial Countercurrent (SECC), which originates around 2°-4°S connected to the convergence of the East African Coastal Current (EACC) and the southward flowing Somali Current (SC) (Fig.1.4a). The situation is different in boreal summer, when the southwest monsoon winds drive a net eastward flow north of the Equator and induce the SC to be northward (Fig. 1.4b). A tropical cyclonic gyre is then formed between the SEC, the EACC-SC and the currents in the North Indian Ocean (Woodberry et al., 1989). The Sverdrup stream function based on seasonal wind stress patterns reproduces well the changes in the interior flow associated with the tropical and subtropical gyre circulations in summer, and the presence of the SECC in winter (see Fig. 1.5).

Another peculiarity of the Indian Ocean is the interchange of tropical warm water from the Pacific Ocean via the Indonesian Passages, called the Indonesian Throughflow (ITF). The driving force of this throughflow is the pressure gradient from the western Pacific Ocean to

Introduction

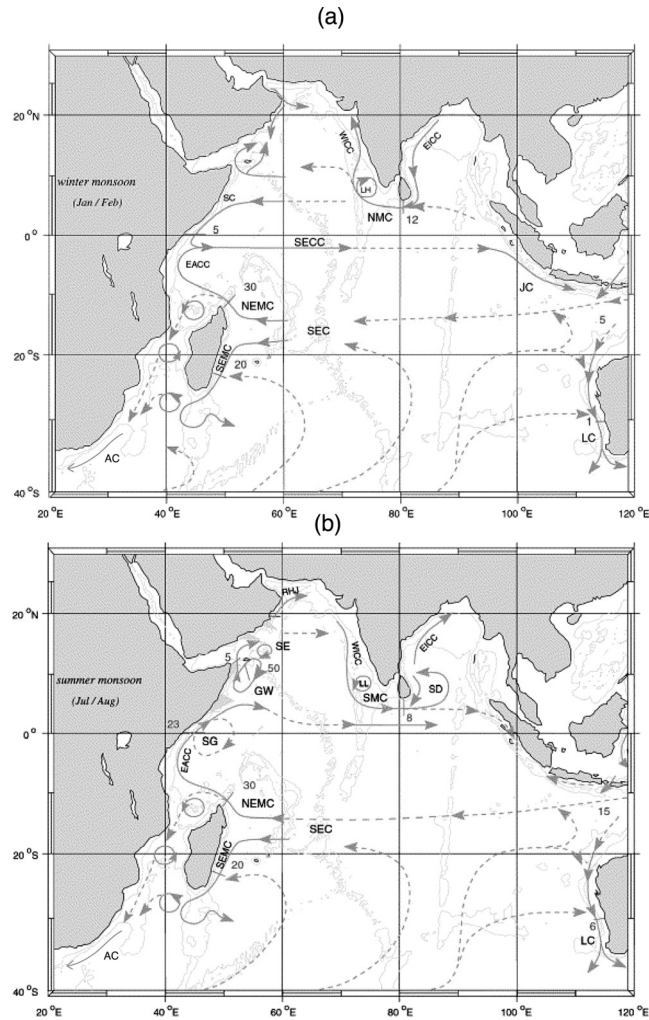


Figure 1.4: Schematics of the surface currents in the Tropical Indian Ocean during the (a) northeast monsoon and b) southwest monsoon, including some transport estimates in Sv ($1 \text{ Sv} \equiv 10^6 \text{ m}^3 \text{ s}^{-1}$). In the South Indian Ocean, the main currents are the South Equatorial Current (SEC), South Equatorial Countercurrent (SECC), North and South Madagascar Current (NMC and SMC), East African Coastal Current (EACC), Somali Current (SC), South Java Current (JC), Leeuwin Current (LC) and Agulhas Current (AC) (adapted from Schott and Mc Creary, [2001]).

the eastern Indian Ocean (Wyrтки, 1987), which can be represented by the sea level difference between Davao and Java (Meyers, 1996). The ITF enters the Indian Ocean basin between 10° - 15° S and most of it is advected in the upper ~ 250 m of the SEC (Gordon, 1986). The ITF water is characterized by a salinity minimum that can be traced in the west along the western side of the Mozambique Channel and the eastern coast of Madagascar, while a second path

The Indian Ocean

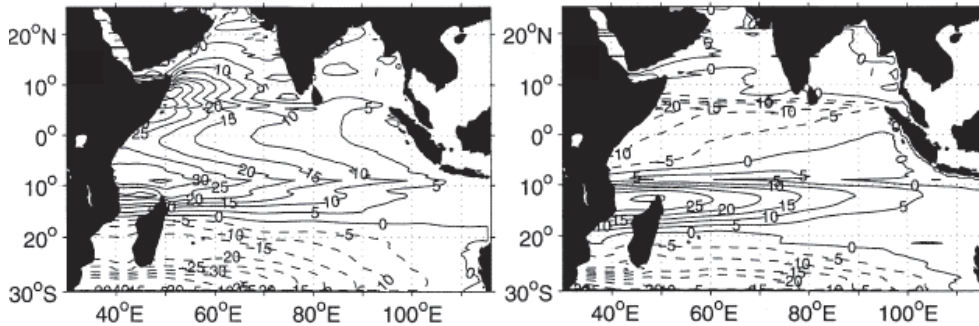


Figure 1.5: *Equivalent Sverdrup transport function in Sv for July (left) and January (right), based on climatological seasonal wind stress curl from the NCEP Reanalysis data set (from Schott and McCreary, [2001]).*

follows the EACC to the North Indian Ocean and returns to the south via the open ocean upwelling region between 5° - 10° S (Song et al., 2004). Ultimately, ITF water exits the Indian Ocean basin via the Agulhas Current retroflexion.

The subtropical Indian Ocean circulation is closed in the west by the Agulhas Current (AC) flowing southward along the African coast (Fig. 1.4). On reaching the southern tip of Africa, the AC exhibits a strong eastward retroflexion with shedding of warm core Agulhas rings (Lutjeharms, 2006). Historical estimates of the AC transport have varied between 9-100 Sv ($1 \text{ Sv} \equiv 10^6 \text{ m}^3 \text{ s}^{-1}$), and more recently they seem to agree on about 75 Sv (Beal and Bryden, 1999; Donohue and Toole, 2003). The largest contribution to the AC transport comes from an anticyclonic recirculation in the southwest of the subtropical gyre (Stramma and Lutjeharms, 1997). The upstream sources of the AC are the flow through the Mozambique Channel and the EMC, which contribute ~ 15 Sv and 20 Sv, respectively (Donohue and Toole, 2003; Ridderinkhof and de Ruijter, 2003). The AC also forms part of the warm water route of the THC, by which water entering the Indian Ocean via the ITF and as deep water along its southern boundary, returns to the North Atlantic (Gordon, 1986). This interocean exchange, known as Agulhas leakage, primarily happens through the shedding of Agulhas rings (de Ruijter et al., 1999). On average 5 to 6 rings per year enter the South Atlantic, each ring carrying a volume transport between 0.5-1.5 Sv (de Ruijter et al., 1999; Schouten et al., 2000). The shedding of Agulhas rings is a local process that may be regulated by variability from upstream regions. This comprise the formation of cyclonic eddies along the AC western flank (van Leeuwen et al., 2000) and southward propagation of anticyclonic eddies from the Mozambique Channel and South Madagascar regions (Schouten et al., 2002a).

1.2.2 Climate variability

Over the last decade, the Indian Ocean interannual variability has been the focus of several investigations concerning both modes of Indian Ocean internal variability (Webster et al., 1999; Behera and Yamagata, 2001; Reason, 2001) and ENSO as external forcing for Indian Ocean climate variability (Reason et al, 2000; Baquero Bernal et al., 2002). The ENSO signal dom-

Introduction

inates the SST interannual variability in the Indian Ocean displaying a basin-scale uniform warming in phase with the peak of an event in the Pacific (Tourre and White, 1995). In the Southwest Indian Ocean, SSTs show significant variability at periods of 4-6 years and significant coherence with ENSO at quasi-biennial periods (Nicholson, 1997). However, these signals are not correlated either with local cloud or latent heat flux anomalies, suggesting that ocean dynamics may be responsible for transferring ENSO effects (Klein et al., 1999). Xie et al. (2002) showed that both ENSO and Sumatra upwelling force subtropical Rossby waves in the Indian Ocean that ultimately control the SST variability in the western Indian Ocean upwelling region between 5° - 10° S, i.e. due to the shallow mean thermocline the SST is responsive to subsurface variability. Another dynamical effect of ENSO in the Indian Ocean is via variations in the Indonesian Throughflow (ITF). Hydrographic observations along a section between Australia and Indonesia showed a decrease (increase) in the ITF transport during El Niño (La Niña), with a peak to trough amplitude of 5 Sv (Meyers, 1996). Modeling studies show that interannual variations in the ITF force Rossby waves in the Indian Ocean in a similar way as the adjustment of the basin circulation to variable wind forcing (Hirst and Godfrey, 1994). Additionally, variations in the ITF indirectly affect the Rossby wave characteristics by changing the ocean's upper layer temperature (Verschell et al., 1995).

An interannual mode of variability with characteristics similar to ENSO was discovered quite recently in the Indian Ocean (Webster et al., 1999; Saji et al., 1999). It consists of cold SST anomalies off Sumatra and warm SST anomalies in the central western basin, hence the name Indian Ocean dipole (IOD). The forcing of the IOD has been widely discussed, some studies stress its dependence on ENSO (Allan et al., 2003; Baquero Bernal et al., 2002); others argue that it may be an internal mode of the Indian Ocean (Webster et al., 1999; Saji et al., 1999; Rao et al., 2002). The IOD is initiated by cooling events along the coast of Sumatra, which induce a decrease in convection over Indonesia and subsequently a northward extension of the trades (Saji et al., 1999). Anomalous easterlies along the Equator force equatorial and coastal Kelvin waves that interrupt the normal heat supply to the east and shallow the thermocline off Sumatra, enhancing the original cold SST (Meyers, 1996). Occasionally, equatorial downwelling Rossby waves enhance the warming in the west (Murtugudde et al., 2000). Equatorial dynamics may play an important role in the reverse of the dipole phase by subsequent Rossby and Kelvin wave reflections (Le Blanc and Boulanger, 2001). However, a subtropical Rossby wave forced by the IOD wind stress curl anomalies in the central-eastern Indian Ocean is essential for the turn about of the mode phase the year following an event (Rao et al., 2000; Feng and Meyers, 2003).

Westward propagating annual and interannual Rossby waves have been observed from satellite altimetry in the subtropical Indian Ocean between 5° - 15° S (Perigaud and Delecluse, 1992; Perigaud and Delecluse, 1993). Both observations and modeling suggest that the waves emanate from the eastern boundary and are strongly modified by the Ekman pumping accumulated throughout the region to the east of a given location (Masumoto and Meyers, 1998). The annual signal appears to be blocked by bottom topography to the east of Madagascar and thus does not influence current variability in the west (Kindle, 1991). Analysis of altimetric sea surface height (SSH), SST and wind stress data showed that the interannual Rossby waves in the Indian Ocean are coupled to the atmosphere, taking between 2-3 years and 3-4 years to cross the basin (White, 2000). In addition, they propagate over a standing Rossby wave displaying opposite thermocline depth or heat content anomalies on the eastern and western

sides of the basin representative of the IOD phases (White, 2000; Jury and Huang, 2004). On the other hand, analysis of the structure of the wind stress curl along 10°S did not show anomalies propagating along the Rossby waves characteristics, but rather alternating anticyclonic and cyclonic events in the central-eastern basin; moreover, these curl events seem to extend further south into the subtropics in response to ENSO forcing (Jury and Huang, 2004). An spectral analysis of SSH data over the Indian Ocean revealed, in addition to the ENSO and IOD signals, an interannual periodicity at around 18-20 months, with maximum amplitude front off Sumatra, and in the central Indian Ocean between 5° - 15°S and in a narrow band between 23° - 24°S (Sakova et al., 2006). This signal may represent an internal mode of variability of the Indian Ocean that then propagates into the Indonesian Throughflow region, and might be involved in the triggering of IOD events.

1.3 The variability around Madagascar

A picture of the SSH variability from altimetry in the South Indian Ocean highlights the highly energetic region south of Africa associated with the Agulhas retroflexion and Agulhas Return Current (Lutjeharms, 2006), and two routes of high variability around Madagascar converging into the Agulhas Current path (Fig. 1.6). As mentioned above, the eddy variability around Madagascar probably influences the interocean exchange between the Indian and South Atlantic Oceans around South Africa. The variability in the former region is intimately related to the dynamics of the Mozambique Channel and the East Madagascar Current (EMC).

Observations in the Mozambique Channel have shown a flow dominated by eddies (Harris, 1972; de Ruijter et al., 2002). This has caused, in part, estimates of the Channels transport to be quite irregular in time (see Di Marco et al., 2002 for an historical review). A mooring array placed in the narrowest section of the Channel during 2000-2001 measured a mean annual transport of 14 Sv, which was achieved by the regular propagation of anticyclonic eddies at frequencies of 4 times/year, or in other words, no western boundary current was detected (Ridderinkhof and de Ruijter, 2003). Eddies in the Mozambique Channel have also been observed with satellite altimetry (Biaostoch and Krauss, 1999; Schouten et al., 2002a). Analysis of 6 years of SSH anomalies with a multi channel singular spectrum analysis showed a variation in the dominant frequency of eddy variability from 7 times/year and 5 times/year in the northern Channel, to about 5 times/year in its center, and 4 times/year in its south (Schouten et al., 2003). The high frequency in the north is related to barotropic instability of the South Equatorial Current at a period of 50 days (Quadfasel and Swallow, 1986), probably the main cause of eddy formation.

Altimetric SSH features at a frequency of 4 to 5 times/year and with amplitudes of 20-30 cm were followed propagating southward from the Mozambique Channel and south of Madagascar into the offshore edge of the Agulhas Current, and eventually into the retroflexion area, where they seem to control the timing of Agulhas rings shedding (Schouten et al., 2002a). Variability at a 4 to 5 times/year frequency was also detected in the central Indian Ocean in the form of westward propagating Rossby waves along the latitude bands of the northern and southern tips of Madagascar (Schouten et al., 2002a), i.e. the 12° and 25°S bands (Fig. 1.6). It is possible that on reaching the island, interaction of these waves with local anomalies and currents leads to formation of eddies. In this way, the eddy variability

Introduction

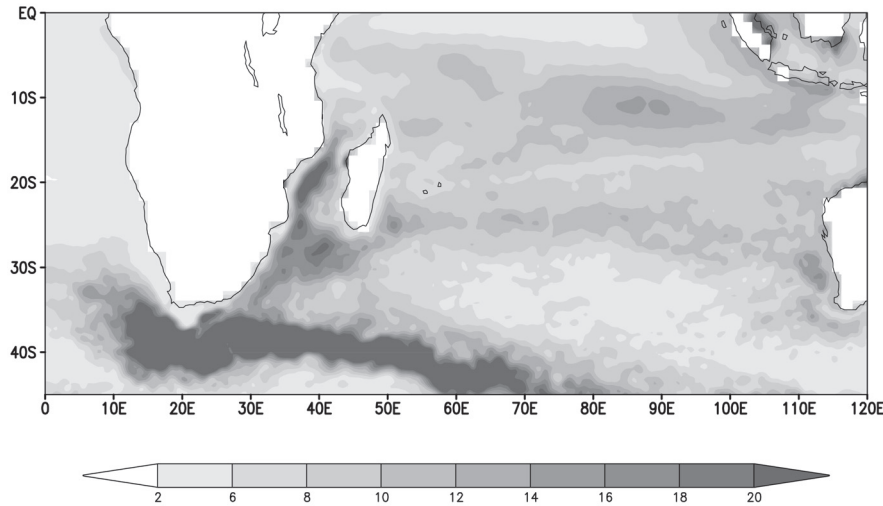


Figure 1.6: *Rms of the weekly sea surface height (SSH) data in the South Indian Ocean from the combined T/P-ERS data set. Data from October 1992 until January 2004 is used. Values lower than 2 cm are not shown. Units in cm. East of Madagascar, two bands of enhanced variability are visible around 12°S and 25°S.*

around Madagascar and consequently that further downstream is not independent of the large-scale Indian Ocean variability (de Ruijter et al., 2005). Furthermore, the 4 to 5 times/year Rossby waves along 12°S could be related to Indian Ocean equatorial wind variability via an ocean wave teleconnection: 4 times per year equatorial Kelvin waves arrive at the coast of Sumatra, where they trigger poleward coastal Kelvin waves that carry the high frequency into the subtropical region; a significant correlation at a lag related to the time it takes the Rossby waves to propagate westward to Madagascar (~ 1.25 year) appears in the rate of eddy formation in the Mozambique Channel (Schouten et al., 2002b). In particular, this correlation suggests that decreases in the eddy activity in early 1996 and 1999 are related to the basin interannual variability due to the occurrence of anomalous equatorial easterlies during the 1994 and 1997 ENSO/IOD events, which inhibited the Kelvin wave signal.

Along the east coast of Madagascar, the EMC carries a southward transport of 20 Sv (Swallow et al., 1988; Donohue and Toole, 2003). One hypothesis is that at its termination point the EMC retroflects with eddies being shed westward, similar to the Agulhas Current (AC) (Lutjeharms et al., 1981). This was supported by analysis of satellite imagery SST and drifters (Lutjeharms, 1988). Still, observations in this region are not enough to conclude about the fate of the EMC, and several intermittent paths are accepted (Quartly and Srokosz, 2004). Both hydrographic observations and altimetry data have shown cyclonic and anticyclonic eddies south of Madagascar propagating (south-) westward towards the Agulhas Current (Gründligh, 1995; Quartly and Srokosz, 2004; de Ruijter et al., 2004).

The eddy variability in the region south of Madagascar is influenced by both 4-5 times/year (Schouten et al., 2002a) and semiannual (Morrow and Birol, 1998) Rossby

The variability around Madagascar

waves propagating along the subtropical band of variability in the Indian Ocean (see Fig. 1.6). While the forcing of the semiannual waves is associated with variations in the thermocline along the eastern boundary (Biol and Morrow, 2001), that of the 4 to 5 times/year Rossby waves has not been identified yet. Semiannual signals could also represent eddies from the Leeuwin Current propagating (north-) westward into the Indian Ocean up to 90°E (Fang and Morrow, 2003). In the west, near 45°E, the Rossby waves amplitude is largely amplified and their phase speed increases (Morrow and Biol, 1998). This may be caused by interaction with the local eddy field and currents, and/or by abrupt changes in the bottom topography (Morrow and Biol, 1998; Schouten et al., 2002a). A recent study combining hydrographic observations and 6 years of altimetry data described the regular appearance of vortex pairs or dipoles in the region south of Madagascar, with significant interannual variability (de Ruijter et al., 2004). The low-frequency variation in the eddy activity might be related to changes in the EMC regime induced by large-scale SSH anomalies from the tropical climate modes, namely ENSO and the IOD. This implies that the eddy variability in the region around South Madagascar may be also influenced by the large-scale tropical Indian Ocean variability, i.e. along the northern band in Fig. 1.6.

It is clear that a large part of the low-frequency or interannual Rossby wave variability observed from satellite altimetry propagating in the Indian Ocean along 12°S towards North Madagascar is related to the tropical Indian Ocean climate variability. Little emphasis though has been given to the impact of these remotely forced interannual anomalies on the circulation around Madagascar, and in particular on the local eddy field. This leads to one of the questions of this thesis:

How do the currents around Madagascar, and subsequently the eddy variability, change in response to remote or local wind forcing, and by the large-scale climate modes (ENSO, IOD)?

On the other hand, subannual Rossby waves arriving at the northern and southern tips of Madagascar are a key control for the eddy variability in that region, and possibly for that of the whole Agulhas system; however, questions regarding the origin of the high-frequency in the basin remain. In particular, the forcing of the 4 to 5 times/year Rossby waves in the subtropical Indian Ocean sector between 20°-30°S has not been investigated. The second question formulated in this thesis is then:

Can we explain the appearance of 4 to 5 times/year variability in the center of the South Indian Ocean subtropical gyre by instability processes related to the mean currents vertical shear?

Finally, history has shown that it is extremely difficult to obtain reliable estimates of the total transport through the Mozambique Channel from observations. A theoretical estimate can be obtained from the linear island rule (Godfrey, 1989) that connects winds over the interior Indian Ocean directly to the transport in the Channel. It is still unclear to what extent this theoretical estimate is adequate, given the highly nonlinear circulation around the island. So, a third question is:

What sets the transport in the Mozambique Channel?

1.4 Thesis outline

Based on the preceding discussion the following four specific questions are addressed in each of the chapters of the present thesis:

- What are the spatial and temporal scales of low-frequency variability of the wind stress curl in the South Indian Ocean?
- What is the connection between the low-frequency eddy variability around Madagascar and the large scale Indian Ocean variability from the IOD or ENSO?
- What is the origin of the variability in the subtropical band of the Indian Ocean around 25°S?
- What sets the transport in the Mozambique Channel, and is the linear island rule adequate?

In Chapter 2 we analyze the wind stress curl variability in the South Indian Ocean using different wind stress products. For large-scale and low-frequency variability analyses winds from the NCEP Reanalysis data set are used, whereas higher resolution scatterometer winds are suitable for studying the wind stress curl characteristics around Madagascar. The seasonal distribution of the curl in the South Indian Ocean from these data and its connection with the well-known seasonal changes in the circulation are presented. The spatial patterns of low-frequency curl variability are identified via empirical orthogonal function (EOF) analysis in the time domain. The relation of the first three EOFs with ENSO and the IOD cycle are discussed in terms of composite analysis of wind curl anomalies over 1948-2003.

Chapter 3 begins with a description of the interannual variability of the SSH and eddy kinetic energy (EKE) in the Mozambique Channel and the regions east and south of Madagascar using 10 years of Topex-Poseidon (T/P)-ERS altimetry data. To understand these low-frequency changes, we use a lagged correlation analysis to study the propagation of large-scale SSH anomalies generated in the eastern Tropical Indian Ocean during the IOD. The Rossby wave propagation between 10°-15°S, as well as the final sea level response around Madagascar, is significantly affected by local wind forcing. Then, the current variability around Madagascar is analyzed by computing geostrophic velocity anomalies on the boundary currents across the satellite tracks. Although we focus on correlations with the IOD, during the last decade the effects of ENSO on the Indian Ocean variability can not be separated from the IOD-impact¹.

Next, the origin of the variability along the 25°S band in the subtropical Indian Ocean is investigated in Chapter 4. A description of the upper layer currents to the east of Madagascar and of the mean vertical shear is presented using the available hydrographic data sets. The baroclinic instability potential of the vertically sheared system is evaluated with a simple 2-layer model. Subsequently, the calculated wavelengths and frequency of the unstable modes can be compared with typical eddy spatial and temporal scales derived from altimetry along these latitudes².

¹The contents of Chapter 3 are based on Palastanga, V., P. J. van Leeuwen, and W. P. M. de Ruijter (2006)

²Chapter 4 is based on Palastanga, V., P. J. van Leeuwen, M. W. Schouten, and W. P. M. de Ruijter (2007)

Thesis outline

In Chapter 5 we return to the analysis of the currents around Madagascar, but from a more conceptual point of view. Steady solutions are derived within a barotropic shallow water model using continuation techniques to test inertial effects on the Mozambique Channel transport. The response to different wind stress patterns (i.e., annual mean, July and January) and wind amplitudes is analyzed. The transport given by the model is compared to the estimate of the Channel's transport from the linear island rule. In particular, the contributions of inertia and friction to the transport are investigated by analyzing the circulation integral of the momentum balance in a circuit connecting the western boundary of the island with the basin eastern boundary. Estimates of the linear island rule using different wind stress products are also presented.

Chapter 2

The wind stress curl over the South Indian Ocean: seasonal and interannual variability

2.1 Introduction

Knowledge of the wind stress curl patterns and variability is relevant for both the ocean circulation and climate variability. The importance of the wind stress curl in setting up the cyclonic and anticyclonic gyres that characterize the large-scale mean ocean circulation has been recognized since Sverdrup's theory (Sverdrup, 1947). In addition, wind stress curl anomalies are one of the forcings of planetary Rossby waves, which transfer information towards the oceans western boundaries (Chelton et al., 1996). These waves have been observed in the Indian Ocean between 10° - 30° S freely propagating (Masumoto and Meyers, 1998; Schouten et al., 2002) and coupled to the atmosphere (White, 2000). Over the last decade, large-scale wind stress anomalies associated to climate modes of the ocean-atmosphere system have been documented across the Indian Ocean basin (Saji et al., 1999; Reason et al., 2000; Reason, 2001). In the subtropics, these wind curl anomalies force Rossby waves that eventually influence the sea surface temperature variability in the western basin due to the anomalous upwelling (Xie et al., 2002). Other aspects of the impact of climatic curl anomalies on the Indian Ocean circulation remain, however, quite unknown.

The wind stress curl over the Indian Ocean has a unique seasonal dependence due to its link to the Indian monsoon. The monsoonal effects are felt most dramatically north of the Equator, where the wind stress changes from northeast in boreal winter to southwest in boreal summer (e.g. Slingo et al., 2005). South of the Equator the seasonal amplitude is small. The center of the subtropical high shifts from 85° E, 33° S in winter to 65° E, 30° S in summer, when it also strengthens (see Fig. 1.3). Consequently, the southeast trades shift northwards and are stronger and more constant in direction between Australia and Madagascar in boreal summer than in boreal winter. Due to the reversal of the trades over the North Indian Ocean only the winter tropical circulation resembles that of the other oceans,

with two westward flowing Equatorial Currents separated by a South Equatorial Countercurrent (SECC) (Fig.1.4a). The SECC originates from the convergence around 2° - 4° S of the northward flowing East African Coastal Current (EACC) and the southward flowing Somali Current (SC) (Schott and McCreary, 2001). In summer, the SC reverses direction and is fed by the EACC, whereas the South Equatorial Current (SEC) strengthens in connection with stronger trades (Hastenrath and Greischar, 1991). Lighthill (1969) estimated the adjustment time of linear equatorial baroclinic modes to the onset of the summer monsoon and found that 40% of the SC transport builds up in about 1 month; although in the real-ocean this time could be even shorter. Schott and McCreary (2001) showed that Sverdrup dynamics adjusted to varying seasonal winds explains the large-scale changes associated with the Indian Ocean tropical gyres. The seasonal Tropical Indian Ocean circulations have also been reproduced in a $1\frac{1}{2}$ -layer model forced with climatological monthly winds (Woodberry et al., 1989).

Indications of interannual variability in the wind stress (curl) over the Tropical Indian Ocean have been found in connection with the Indian Ocean Dipole (IOD) and ENSO modes. A large-scale positive wind curl anomaly is present in the eastern tropical Indian Ocean between 0° - 10° S during the positive phase of the IOD (Saji et al., 1999; Murtugude et al., 2000; Huang and Kinter III, 2002). Using a composite analysis of six extreme IOD events, Saji et al. (1999) described the appearance of moderate southeasterly anomalies in the eastern Tropical Indian Ocean at the beginning of a positive event in boreal spring, followed in September-October (i.e. at the peak of the event) by a strengthening and northward shift of the trades, which induces anomalous easterlies along the Equator. In the subtropical Indian Ocean between 15° - 25° S anomalous northwesterlies appear from September-October-November (SON) to DJF (Huang and Kinter III, 2002). In addition, Huang and Kinter III (2002) found that during IOD events that were not ENSO years, there was a broader strengthening of the trades across the basin in the early stages of the IOD evolution, similar to a strong monsoon year. Reason et al. (2000) carried out an extensive analysis of ENSO signals across the Indian Ocean based on seasonal composites of different oceanic and atmospheric variables, including surface wind anomalies. During the OND season previous to a peak of El Niño (La Niña) and during the event peak in JFM, strong south-easterly (north-westerly) wind anomalies appear in the eastern Tropical Indian Ocean, while in the western-central Indian Ocean wind anomalies point to a shift in the tropical South Indian Ocean Walker circulation, with enhanced (reduced) convection east of Madagascar. Using a regression analysis with IOD and ENSO indices, Saji and Yamagata (2003) analyzed ENSO events that did not co-occur with the IOD, and vice versa. They also documented anomalous southeasterlies in the central-eastern Indian Ocean during El Niño in SON and DJF, but with less amplitude than those by Reason et al. (2000). Rao et al. (2002) showed that while El Niño induces a weakening of the equatorial westerly winds from October to December, during a positive IOD these winds completely reverse, causing strong and prolonged thermocline variations in the Tropical Indian Ocean that sustain the IOD mode.

Another dipole of interannual variability, independent of the IOD and phase locked to the austral summer season, has been documented in the subtropical Indian Ocean around 30° S (Reason, 2001). Analysis with an ocean general circulation model (OGCM) suggests that this mode is forced by an atmospheric $3/4$ wave pattern in the Southern Hemisphere, leading to a southward shift of the atmospheric anticyclone in the subtropical Indian Ocean and a strengthening of the trades during positive events, and vice versa during negative events

Data and Procedures

(Hermes and Reason, 2005). A significant multidecadal signal consistent with a weakening of the atmospheric subtropical anticyclone from 1900 to 1941, and a strengthening in 1963-83 has been reported by Allan et al. (1995). The local atmospheric forcing of this multidecadal oscillation could be part of a global decadal mode of the Southern Hemisphere (Reason and Lutjeharms, 2000).

There is thus enough evidence of low frequency variability in the winds over the South Indian Ocean; nevertheless, a detailed description of the spatial and temporal scales of wind stress curl variability is missing. In view of the strong connection of curl anomalies and ocean circulation variability, one goal of this Chapter is to analyze the interannual variability of the curl over the South Indian Ocean, with emphasis on signals from the IOD and ENSO. To achieve this goal we use winds from a reanalysis data set, which spans a period of over 50 years. Previous analyses of the seasonal variability of the wind stress curl over the Indian Ocean have been based on coarse resolution wind stress products (Hellerman and Rosenstein, 1983) and reanalysis data from weather prediction models (Schott and McCreary, 2001; Slingo et al., 2005). In recent years, the advent of wind data from onboard satellite scatterometers has provided an unprecedented temporal and spatial coverage of the wind field over the global oceans. Moreover, due to its high-resolution, this data set enables a better representation of the wind stress curl field. In particular, the curl computed from scatterometer winds reveals small-scale features near large-scale islands that could not be resolved by other means (Chelton et al., 2004). A second goal of this Chapter is to describe the seasonal variability of the large-scale wind stress curl, and in particular that for the region around Madagascar based on high-resolution scatterometer winds. A complete description of the different wind data sets and methods used in this study is presented in Section 2.2. We discuss the patterns of wind stress curl variability on seasonal and interannual time scales in Section 2.3 and Section 2.4, respectively. Finally, we summarize and discuss the results of this Chapter in Section 2.5.

2.2 Data and Procedures

2.2.1 Data

We use winds from the two missions of the European Remote Sensing (ERS) satellite scatterometer (i.e. ERS-1 and ERS-2), which operated during the period 1991-2000. The ERS scatterometer samples surface wind vectors across a 500 km swath at 50 km resolution, with 40% coverage of the global ocean every 24 hours. Scatterometers infer surface wind speed and direction at any given location under all weather and cloud conditions. Monthly means of wind stress and stress curl estimates over a $1^\circ \times 1^\circ$ grid were obtained from the Centre ERS d'Archivage et Traitement (CERSAT, France)¹. This product covers the period March 1992 to December 2000.

The SeaWinds scatterometer onboard the QuikSCAT satellite (QuikSCAT) has been in operation since July 1999. QuikSCAT presents greater spatial and temporal coverage than ERS scatterometers, as it samples wind vectors with 25 km resolution over a 1600 km swath that covers 90% of the ocean surface daily. Monthly means of wind stress and wind stress

¹More information can be found at the CERSAT website: <http://www.ifremer.fr/cersat>.

curl spanning the period August 1999-June 2006 are also processed and provided over a $0.5^\circ \times 0.5^\circ$ grid by CERSAT. We use these data to investigate the wind stress variability in the region around Madagascar.

Monthly means of zonal and meridional momentum flux for the 56 years period 1948-2003 were obtained from the National Centers for Environmental Prediction (NCEP) reanalysis data (Kalnay et al., 1996). These data are given on a Gaussian grid, with approximately 2° horizontal resolution. Note that NCEP and scatterometers winds can be considered independent data sets; only since January 2002 the NCEP model started assimilating QuikSCAT winds.

2.2.2 Procedures

Seasonal means were obtained by taking three-month means for December-January-February (DJF), MAM, JJA, and SON. In this Chapter, seasons always refer to those in the Northern Hemisphere. To compute wind stress curl anomalies at interannual time scales the seasonal cycle was removed from the monthly mean data by subtracting climatological monthly means from individual months. For the analysis in Section 2.4 wind stress curl anomalies were band pass filtered to concentrate on the interannual band. A Lanczos filter (Duchon, 1979) with cutoff frequencies of 0.01 months^{-1} and $0.0625 \text{ months}^{-1}$ was applied to the monthly means, i.e. to keep variations between 16 months and 8 years. The minimum number of weights of the filter to assure unit response at the band center is 53. Therefore, the filtered anomalies span the period March 1950-October 2001.

To determine the spatial modes of interannual variability, empirical orthogonal function (EOF) analysis in the time domain (Richmann, 1986) were performed on the filtered wind stress curl anomalies. After obtaining the EOFs time series or principal component (PC) loadings, the original time series can be projected onto them to obtain the PC scores. The latter represent spatial patterns whose variance accounts for a percentage of the total spatial variance of the original field.

2.3 Seasonal variability of the wind stress curl

2.3.1 Large scale wind stress curl

The annual mean wind stress curl from ERS shows negative curl north of 17°S and positive curl to its south, with maxima in the subtropical Indian Ocean southwest of Australia around 35°S and in the central basin between 35° - 40°S (Fig. 2.1a). NCEP data for different time periods display a similar pattern (not shown). The line of zero wind stress curl along 17°S denotes the limit between the Indian Ocean gyre circulations, namely the cyclonic tropical gyre and the anticyclonic subtropical gyre between 17° - 50°S . Due to the Indian monsoon variability, it is more meaningful to look at the mean curl distribution per month. In July, the mean wind stress curl resembles the annual mean (Fig. 2.1b), except that curl maxima occur over the western part of the basin. The negative curl in the Arabian Sea is associated with the development of the Findlater Jet during the Southwest monsoon (Schott and McCreary, 2001), whereas the positive (anticyclonic) curl centered around 50°E , 40°S reflects the western location of the South Indian Ocean high-pressure cell that also strengthens in this season

Seasonal variability of the wind stress curl

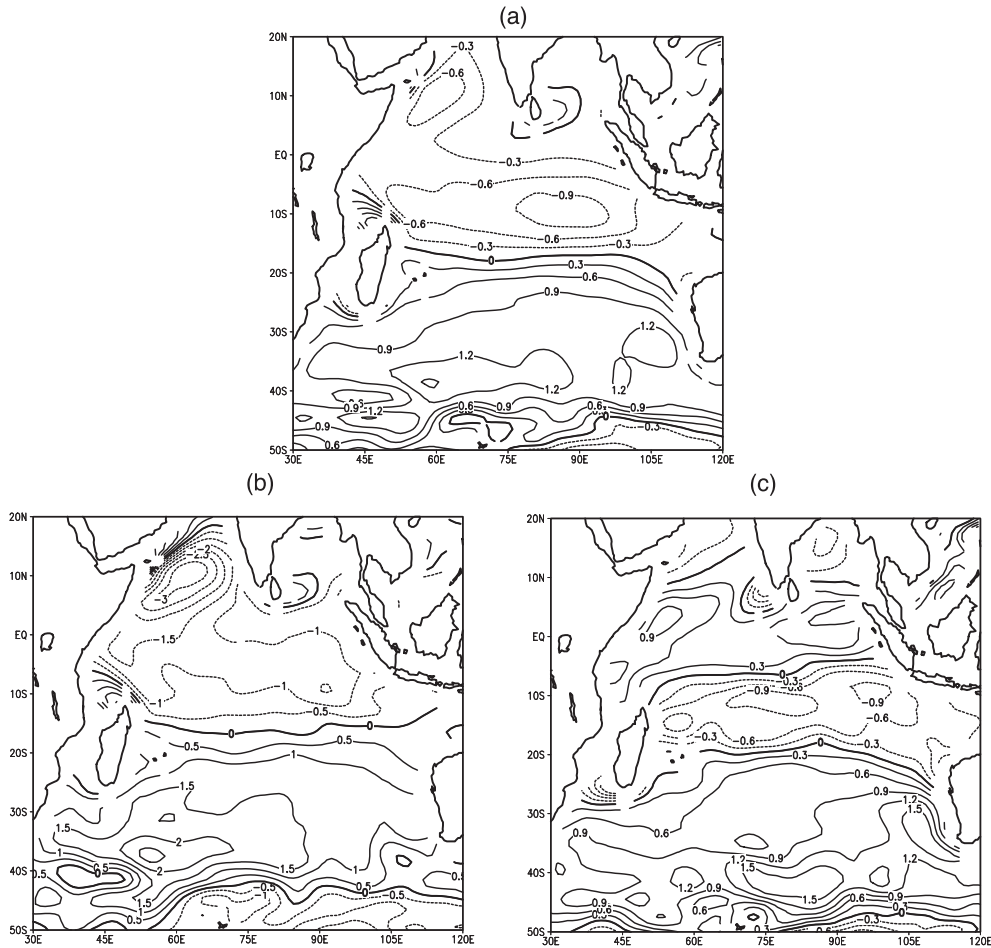


Figure 2.1: Mean wind stress curl in the Indian Ocean estimated with ERS scatterometer wind stress for the a) annual mean, b) July and c) January. Units in $10^{-7} \text{ Pa m}^{-1}$. The annual mean wind pattern drives the horizontal gyre circulation of the Indian Ocean, with a distinct anticyclonic subtropical gyre between, roughly, 17°S and 50°S , and a tropical gyre north of 17°S . The circulation in July resembles the annual mean, while the January wind pattern induces cyclonic circulations between 10°S and 20°S and in the North Indian Ocean, separated by the South Equatorial Countercurrent along $2^{\circ}\text{-}4^{\circ}\text{S}$.

(e.g. Fig. 1.3b). Consequently, the anticyclonic subtropical gyre circulation intensifies; in particular, the SEC is found slightly to the north relative to its annual mean position (Woodberry et al., 1989) and more organized in the western side (Schott and McCreary, 2001). In January, a region of negative (cyclonic) curl extends east of Madagascar between $\sim 7^{\circ}\text{-}20^{\circ}\text{S}$, while over the rest of the basin the curl is positive, except for some regions in the North Indian Ocean (Fig. 2.1c). Also, the maximum southern anticyclonic curl shifts eastward in agreement with the location of the subtropical high in winter (Fig. 1.3a) and the presence

The wind stress curl over the South Indian Ocean: seasonal and interannual variability

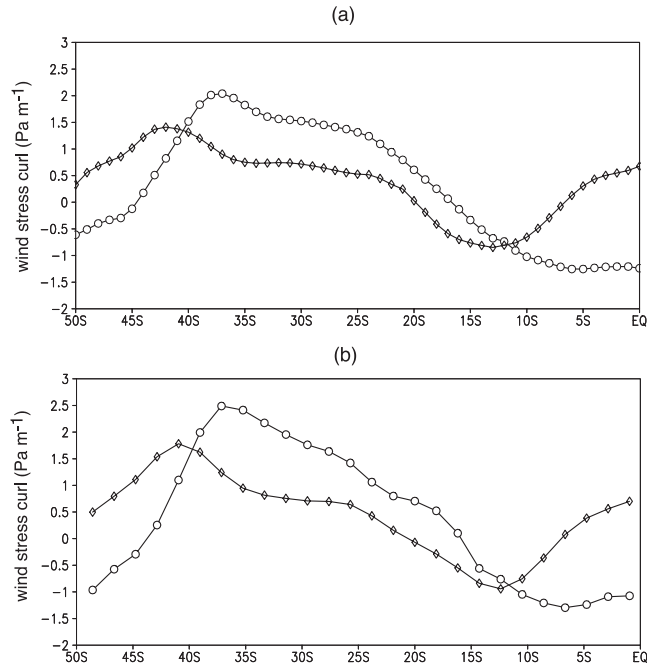


Figure 2.2: Zonal average of the wind stress curl in the South Indian Ocean between 50° - 90° E for January (triangles) and July (circles), based on a) ERS scatterometer winds and b) NCEP model winds. From January to July the maximum wind stress curl shifts from 41° S to 37° S and the zero wind stress curl from 20° S to 15° S.

of a low-pressure system over Australia that induces southerly winds off the western coast (Tchernia, 1980). Overall, the winter curl pattern over the North and South Indian Ocean between 7° - 20° S forces the cyclonic circulations associated with the equatorial currents and the eastward flowing SECC.

Figure 2.2a illustrates a zonal average of the wind stress curl over the South Indian Ocean for January and July. The latitudinal shift of the zero subtropical wind stress curl between winter and summer, as well as the bulk of negative curl which forces the two tropical gyres in winter, are clearly seen. These features are also present in a zonal average from NCEP (Fig. 2.2b), although the latter shows sharper meridional curl gradients than ERS, especially in July. Further differences between ERS and NCEP are related to the magnitude of the extremes, which tend to be larger in NCEP. Over the basin extension, the larger differences between both data sets appear south of 300° S. For example, in July NCEP shows a region of anticyclonic curl from 50° E to 100° E, with maximum curl between 60° - 70° E (not shown). Discrepancies between NCEP winds and satellite observations might be related to differences in the data horizontal resolutions, as well as the scarcity of observations assimilated by the NCEP model over the southern Indian Ocean and/or limitations in model parameterizations, i.e. of sea surface temperature.

Based on NCEP winds, Schott et al. (2001) showed that the meridional Sverdrup trans-

port in the Indian Ocean between 20°N-30°S gives a good representation of the large-scale seasonal changes in the interior circulation (Fig. 1.5). Because ERS data offer higher meridional resolution than previous data sets, we use these data to compute the relation between the zonal Sverdrup transport and the meridional structure of the wind stress curl². The seasonal changes in the zonal Sverdrup transport in the South Indian Ocean between 0°-40°S are shown in Fig.2.3. In February, three westward cores east of 90°E converge into a maximum westward core in the central basin along 18°S that corresponds well with the location of the SEC (Fig. 2.3a). A second westward core is seen east of South Madagascar between 25°-30°S, and north of 15°S the transport is eastward and maximum along 7°S. In August, the zonal transport is westward between 5°-35°S, with a primary core between 15°-20°S in the east and a secondary core along 20°S in the west (Fig. 2.3b). This pattern suggests a slight northward shift of the SEC relative to the winter pattern, consistent with previous analyses (Woodberry et al., 1989). There is also a maximum westward transport north of Madagascar, which is not observed in winter. Hydrographic observations of the North Madagascar Current (NMC) did not detect any significant seasonal variability (Swallow et al., 1988); still, such a maximum wind driven transport could induce variations in the flow through the Mozambique Channel. An analysis of ocean general circulation model simulations described a strong seasonal signal in the flow through the Mozambique Channel, varying from ~0 Sv in February/March to 20 Sv in August (Biastoch et al., 1999). This signal was related to the meridional shift of the trades in summer, as well as a maximum in the southward Ekman transport due to the wind stress at the northern tip of Madagascar. However, observations of the flow field in the narrows of the Mozambique Channel did not show seasonal variability either (Ridderinkhof and De Ruijter, 2003).

2.3.2 Wind stress curl around Madagascar

The curl patterns around Madagascar change sign with the onset of the Southwest monsoon in May, when southeasterly winds east of Madagascar strengthen and extend northward toward the African coast. In the Mozambique Channel the influence of the monsoon is felt until 15°-20°S, due to the effect of the meridional gradient between the northern and southern African high-pressure cells on the circulation ~800 km offshore of Africa (Tchernia, 1980). Recently, Chelton et al. (2004) conducted a global analysis of the mean wind stress curl from 25 km resolution QuikSCAT winds. They reported small-scale curl features at Madagascars northern and southern tips associated with island induced wind shadows and island corner accelerations, respectively. Although seasonal changes in the curl might be an important forcing of local circulations, this issue has not been investigated in the region of the Mozambique Channel. For example, Chavanne et al. (2002) found that the Hawaiian Islands in the Pacific Ocean induce anomalies in the low-level winds that can cause cyclonic and anticyclonic eddies observed in the lee of the islands. Here we present a discussion of the patterns of wind stress and wind stress curl around Madagascar from 50 km resolution

²The meridional Sverdrup transport, V_{Sv} , is related to the curl of the wind stress, $\vec{\tau}$, by $V_{Sv} = curl(\vec{\tau})/\beta\rho_0$, where β is the variation of the Coriolis parameter with latitude and ρ_0 the mean density of the water column. By mass continuity, the zonal Sverdrup transport, U_{Sv} , at a given point is found by zonal integration of the meridional gradient of the curl of τ from the basin eastern boundary E_b to x , i.e. $U_{Sv} = -\int_{E_b}^x \frac{\partial V}{\partial y} dx' = -\frac{1}{\beta\rho_0} \int_{E_b}^x \frac{\partial[curl(\vec{\tau})]}{\partial y} dx'$ (see Pedlosky, 1987).

The wind stress curl over the South Indian Ocean: seasonal and interannual variability

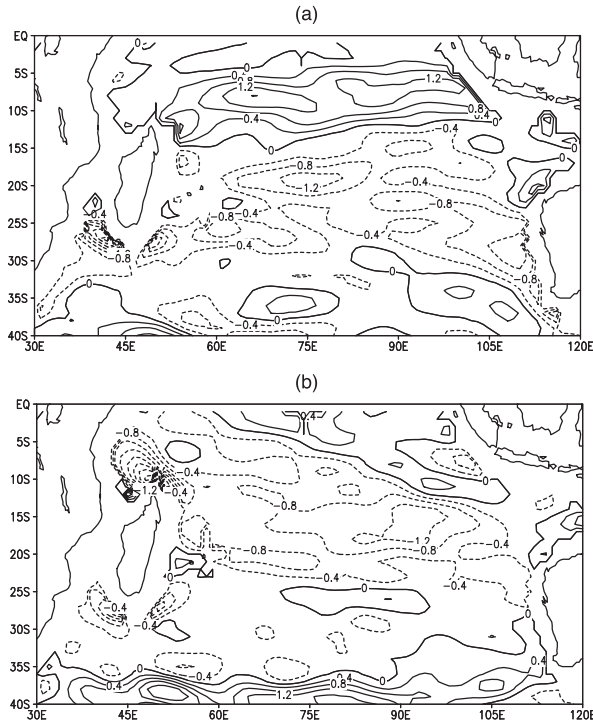


Figure 2.3: Estimate of the zonal component of the Sverdrup transport based on ERS scatterometer winds over the sector $[30^{\circ}\text{--}120^{\circ}\text{E}, 0^{\circ}\text{--}40^{\circ}\text{S}]$, for a) February and b) August. The integral is carried along latitude circles between the first points close to the land mask in the eastern and western borders. Units in Sv. In February three westward cores east of 90°SE converge into the central Indian Ocean and the transport is eastward north of $\sim 12^{\circ}\text{S}$. The latter disappears in August.

QuikSCAT winds for February, May, August and November.

In February, easterly winds are maximum south of Madagascar, and thus, negative curl extends from 27°S to 10°S to the east of Madagascar and from 27°S to 18°S in the Mozambique Channel (Fig. 2.4a). With the onset of the Southwest monsoon in May (Fig. 2.4b), the line of zero curl shifts northward to 18°S ; to its south the curl is positive, as well as in the southwestern Mozambique Channel. At Madagascar's northern tip, positive curl appears due to the wind shadow that the island induces on the northward extended trades. This feature is present from April to November (see also Fig. 2.5). During the peak of the summer monsoon (Fig. 2.4c), there is positive curl in the Mozambique Channel south of $\sim 15^{\circ}\text{S}$, except for the south (-eastern) region. Negative curl present in the northern Mozambique Channel forms a dipole pattern with the positive curl to the northwest of the island (Chelton et al., 2004). The decay of the Southwest monsoon starts in September. In November the line of zero curl is still located around 15°S and the curl around Madagascar is predominantly positive, except for the island's southern tip, where negative (cyclonic) curl dominates (Fig. 2.4d).

Figure 2.5 illustrates the seasonal variability of the wind stress curl dipole observed west

Seasonal variability of the wind stress curl

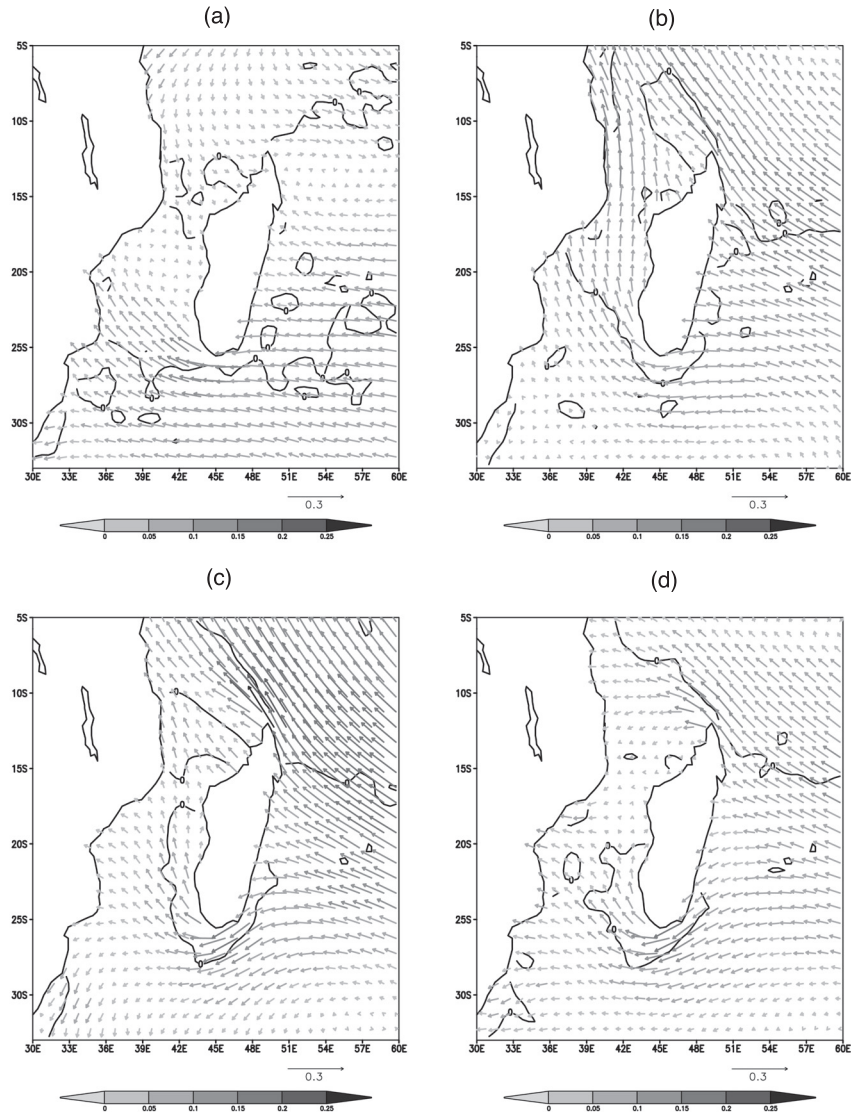


Figure 2.4: Wind stress vectors in the region around Madagascar estimated from monthly averages of QuikSCAT data for a) February, b) May, c) August, and d) November. Contours of zero wind stress curl are superimposed in black. Units in 10^{-7} Pa . The arc length vector in the right bottom of each panel indicates wind stresses of $0.3 \times 10^{-7} \text{ Pa}$ magnitude. The curl around Madagascar is predominantly cyclonic (anticyclonic) in February (November), except around Madagascar's southern tip. With the onset of the southwest monsoon (May) and during its mature phase (August), a curl dipole structure develops northwest of Madagascar's northern tip.

The wind stress curl over the South Indian Ocean: seasonal and interannual variability

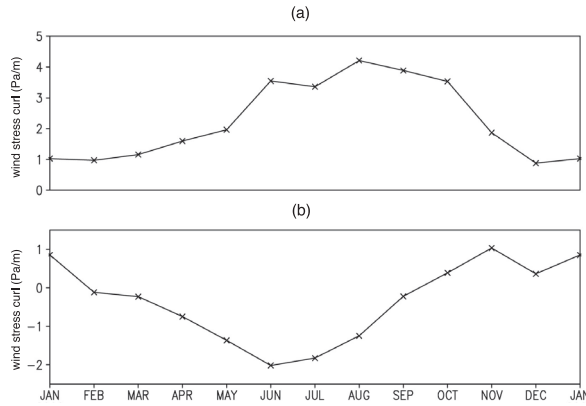


Figure 2.5: Monthly wind stress curl as a function of calendar month averaged a) over the positive core of the dipole northwest of Madagascar [45° - 48° E, 10° - 12° S], b) over its negative core [44.5° - 45.5° E, 12° - 14° S]. Units in $10^{-7} Pa m^{-1}$. The dipole structure, with anticyclonic curl to the north and cyclonic curl to the south, is present from May to August.

of Madagascar’s northern tip. The dipole feature reaches its maximum in June, although the anticyclonic curl shows a maximum of over $4 \times 10^{-7} Pa m^{-1}$ in August. This anticyclonic curl drives an Ekman transport divergence that may induce vertical water motions at the bottom of the Ekman layer. The associated upwelling velocity can be estimated as $w = 1/\rho_0 \text{curl}(\vec{\tau}/f)$, where ρ_0 is an average density, f is the coriolis parameter and $\vec{\tau}$ is the wind stress. Based on $\rho = 1025 \text{ kg m}^{-3}$ and monthly means of the wind stress curl the latter yields a maximum vertical velocity of 1.5 m day^{-1} near 47° E, 11° S. Chavanne et al. (2002) suggested that vertical motions in the thermocline of the order of 3 m day^{-1} can force geostrophic anticyclonic eddies in the lee of the Hawaiian Islands, which might superimpose on eddies formed by instabilities of the North Equatorial Current. In the northern part of the Mozambique Channel anticyclonic eddies are formed by barotropic instability of the SEC at frequencies of 7 times/year (Quadfasel and Swallow, 1986). These eddies drift southward into the Mozambique Channel, where they seem to dominate the flow (Ridderinkhof and De Ruijter, 2003). Compared to the small-scale structures reported by Chavanne et al. (2002), the curl dipole northwest of Madagascar displays a large-scale feature constrained in zonal extension by the African continent. Nonetheless, its possible influence on the forcing of regional mesoscale or Ekman-like circulations needs to be further investigated, i.e. using higher resolution QuikSCAT winds.

2.4 Low frequency variability of the wind stress curl

2.4.1 Tropical climate events in the Indian Ocean

The occurrence of very strong IOD events over the last decade motivated a lot of studies on the characteristics and dynamics of this interannual mode of the Tropical Indian Ocean (Webster et al., 1999; Saji et al., 1999; Murtugudde et al., 2000; Rao et al., 2002, among others). In

addition, there has been an active debate regarding the interdependence between the IOD and ENSO (Baquero Bernal et al., 2002; Saji and Yamagata, 2003; Allan et al., 2001). Wind stress (curl) anomalies related to both the IOD and ENSO have been documented in the tropical-subtropical Indian Ocean during the peak of these events (Saji et al., 1999; Huang and Kinter III, 2002; Reason et al., 2000). Before discussing in detail the interannual variability of the wind stress curl in the South Indian Ocean, we present a short overview of some of the findings concerning the IOD and discuss its co-occurrence with ENSO.

The positive IOD phase is characterized by a cold sea surface temperature anomaly (SSTA) front off Sumatra and a warm SSTA in the central-western Tropical Indian Ocean, accompanied by anomalous equatorial easterlies and equatorward extended trades (Saji et al., 1999). Anomalous atmospheric convection over the eastern-central basin acts as local feedback process onto the original SSTA (Webster et al., 1999). A subsurface dipole of heat content or sea level anomalies is also observed (Huang and Kinter III, 2002; Rao et al., 2002). Furthermore, equatorial-tropical dynamics during the dipole development enhance the cooling in the east and the warming in the west (Le Blanc and Boulanger, 1999; Murtugudde et al., 2000). In the subtropics, a downwelling Rossby wave forced by subtropical wind curl anomalies propagates toward the western boundary and brings the turnabout of the dipole the following year of an event (Rao et al., 2002; Feng and Meyers, 2003).

An IOD index based on the difference of SSTA between the western Tropical Indian Ocean and the southeastern Tropical Indian Ocean as suggested by Saji et al. (1999) is shown in Fig. 2.6. The time series of the Southern Oscillation Index (SOI), defined as the difference between monthly sea level pressure at Darwin, Australia (130.8°E, 12.4°S) and Tahiti, French Polynesia (149°W, 14°S) is also presented. It is clear that the positive (negative) IOD phases in 1994 and 1997 (1996 and 1998) have been the strongest of the period 1951-2003. IOD events show a strong seasonal locking, starting typically in May-June, peaking in September-October, and fading in December (Saji et al., 1999).

A spectral analysis of the IOD index indicates dominant variability at a period of 3 years ($0.026 \text{ months}^{-1}$), with a secondary peak at a period of 1.5 years ($0.053 \text{ months}^{-1}$), both significant at the 90% confidence level (Fig. 2.7). The correlation between the IOD and ENSO indices is low (-0.3), in agreement with Saji et al. (1999), who found a weak correlation between the IOD index and the Niño 3 region SST (≤ 0.35). However, Allan et al. (2001) showed that the correlation of seasonally stratified values of the IOD index with the SST over the Niño 3 region, as well as with the SOI, is significant in SON (-0.59). According to Allan et al. (2001) the ENSO signal in the Indian Ocean is essential to explain the forcing mechanism of the IOD.

There is evidence of strong IOD events that did not occur during ENSO years, like those in 1961 and 1967 (Saji et al., 1999). For example, Rao et al. (2002) classified strong IOD events for the last 134 years and found that 65% of them occurred when there was no ENSO in the Pacific. To clarify the different information concerning the occurrence of simultaneous IOD/ENSO events, we summarize in Table 2.1 the years over the period 1950-2003 which were IOD and/or ENSO. An IOD year corresponds to the year of the peak of an event (i.e. in SON) based on the index in Fig. 2.6, on Rao et al. (2002) and on Saji and Yamagata (2003), whereas an ENSO year is associated with the year in which an event starts (i.e. at the latest in October-December), as classified by Reason et al. (2000) and the Climate Prediction Center (on their website www.cdc.noaa.gov). Because the peak of ENSO occurs typically around

The wind stress curl over the South Indian Ocean: seasonal and interannual variability

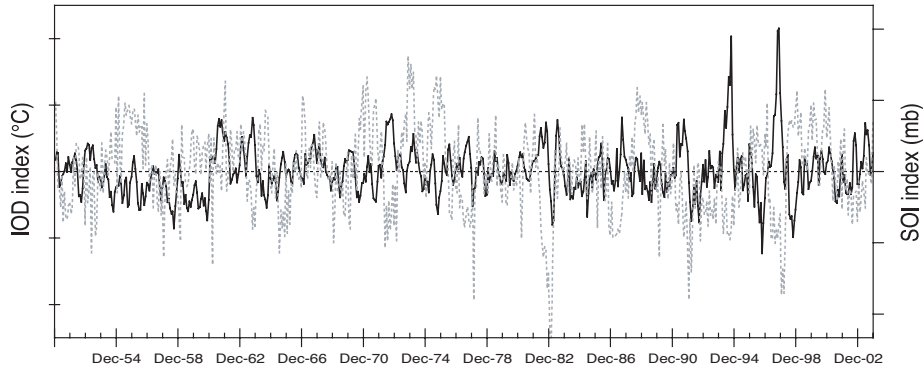


Figure 2.6: Time series of the Indian Ocean Dipole (IOD) Index (black line) and the Southern Oscillation Index (SOI) (grey line) over the period 1951-2004. The IOD index is estimated as the difference between the SST in the tropical western Indian Ocean [50°-70° E, 10°S-10°N] and the tropical south-eastern Indian Ocean [90°-110° E, 0°-10°N] (Saji et al., 1999). The SOI is defined as the difference between time series of monthly sea level pressure at stations in Darwin, Australia (130.8° E, 12.4° S) and Tahiti, French Polynesia (149° W, 14° S).

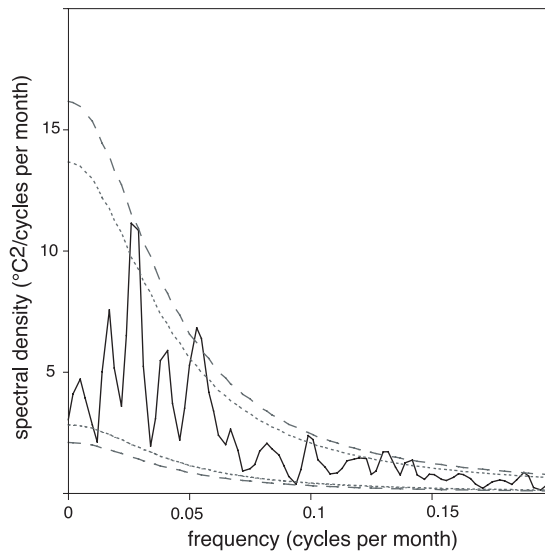


Figure 2.7: Spectral density $^{\circ}C^2 / cpm$ ($cpm = \text{cycles per month}$) versus frequency (cycles per month) of the IOD index time series. Spectral peaks were tested for significance with a red noise spectrum and its confidence bands at the 90% (short dashed line) and 95% (long dashed line) significant levels. A peak at a period of 3 years is significant at the 90% level, whereas a peak around a period of 1.5 years is significant at the 95% level.

DJF, an event also spans the following year, usually at the latest until July, unless otherwise noted (see Table 2.1 for more details). Note also that some ENSO years correspond to long duration or protracted events. These ENSO types are connected to multidecadal signals of the climate system, and display significantly different characteristics and impacts than typical El Niño/La Niña years (Allan et al., 2003). Overall, Table 2.1 shows that there have been 10 positive IOD events (IOD+), of which 4 (i.e. 1953, 1961, 1967, and 1983) occurred during no normal or protracted El Niño episodes, and 15 negative IOD events (IOD-), of which 7 (i.e. 1958-1960, 1989, 1992, 1993, and 1996) were no normal or protracted El Niña years. Therefore, over the last 50 years about 44% of the IOD events occurred during no-ENSO or in anti-phase with ENSO. In particular, the IOD- events in 1954-1955, 1974-1975 and 1998 occurred during protracted La Niña events, while the IOD phases in 1992, 1993 and 1994 co-occurred with the 1991-1995 protracted El Niño.

2.4.2 Wind stress curl interannual variability

Variance

Figure 2.8 presents the standard deviation of wind stress curl anomalies (i.e. only the seasonal cycle was removed from the monthly mean curl) for the period 1948-2003. Four centers of variability are present in the South Indian Ocean: off southwest Sumatra, in the eastern subtropical basin between 90°-100°E, in the western-central basin between 20°-26°S, and in front of the Australian coast. Inspection of the seasonally stratified interannual variance indicates that the annual mean resembles most the variability during SON. The variance in DJF is also high, with the largest variability in the central Indian Ocean between 15°-25°E, in front of Australia and southwest of Madagascar. The interannual variability is comparatively weaker during MAM and JJA (not shown).

EOF analysis

To identify the spatial structures that characterize the wind stress curl interannual variability, we performed an EOF analysis of band passed wind stress curl anomalies (see Section 2.2.b) over the Indian Ocean sector (30°-120°E, 0°-40°S). The first leading EOF account for 10.3% (EOF1), 8.7%(EOF2) and 7.1% (EOF3) of the total spatial variance. The fact that they explain a relatively small fraction of the total variance might be related to noise in the wind stress curl field over the basin domain, or to the coarse estimation of the curl from the NCEP data set. According to North's rule of thumb (North et. al, 1982) the first three EOFs are statistically independent (Fig. 2.9).

Figure 2.11 shows the first three EOFs plotted in terms of maps of SON seasonally stratified wind stress curl anomalies over the Indian Ocean domain correlated onto the amplitude time series of the corresponding EOF. The leading EOF in the South Indian Ocean displays a cyclonic center in the central-western Indian Ocean along 40°S, and a southeast north-west oriented center of anticyclonic curl in the Tropical Indian Ocean, with a smaller region of anticyclonic curl around South Madagascar (Fig. 2.10a). The mode is active basically throughout the year. The second EOF shows an anticyclonic curl anomaly extending front of the coast of Sumatra and a cyclonic curl anomaly centered on 85°E, 10°S, while anticyclonic curl is found broadly between 15°-40°S (Fig. 2.10b). The highest correlations for

The wind stress curl over the South Indian Ocean: seasonal and interannual variability

Years	Indian Ocean	Pacific Ocean
1950		weak La Niña
1951		vweak El Niño
1953	IOD+	
1954-56		protracted La Niña
1954	IOD-	
1955	IOD-	
1957		strong El Niño
1958	IOD-	
1959	IOD-	
1960	IOD-	
1961	IOD+	weak La Niña
1963	IOD+	strong El Niño
1964	IOD-	weak La Niña
1965		strong El Niño
1967	IOD+	weak La Niña
1968		weak El Niño
1969		weak El Niño
1970-71		strong La Niña
1971	IOD-	
1972	IOD+	strong El Niño
1973-76		protracted La Niña
1974	IOD-	
1975	IOD-	
1976		weak El Niño
1977	IOD+	weak El Niño
1982	IOD+	strong El Niño
1983	IOD+	weak La Niña
1984	IOD-	weak La Niña
1986-87		strong El Niño
1988		strong La Niña
1989	IOD-	
1991-95		protracted El Niño
1992	IOD-	
1993	IOD-	
1994	IOD+	
1995		weak La Niña
1996	IOD-	
1997	IOD+	strong El Niño
1998-2001		protracted La Niña
1998	IOD-	
2002		strong El Niño

Table 2.1: *Years of IOD and ENSO phases. An IOD year corresponds to the year of the peak of an event in SON. Strong IOD events are shown in bold based on Rao et al. (2002). An ENSO year represents the year of the onset of an event; as typically the peak of ENSO is reached in December-February, each event spans the following year at the latest until July. Exceptions were the long duration 1970-71 La Niña and 1986-87 El Niño, which finished in early 1972 and 1988, but do not correspond to protracted events (Allan et al., 2003). The classification of strong ENSO years is according to Reason et al. (2000); all other ENSO events are classified as weak or protracted.*

this mode occur in SON and DJF. The third EOF displays a north-south dipolar structure in the subtropical Indian Ocean east of Madagascar, with its axis around 25°S and maximum negative (positive) correlations around 15°S (30°S) (Fig. 2.10c). The maximum correlations are observed both in JJA and SON.

Low frequency variability of the wind stress curl

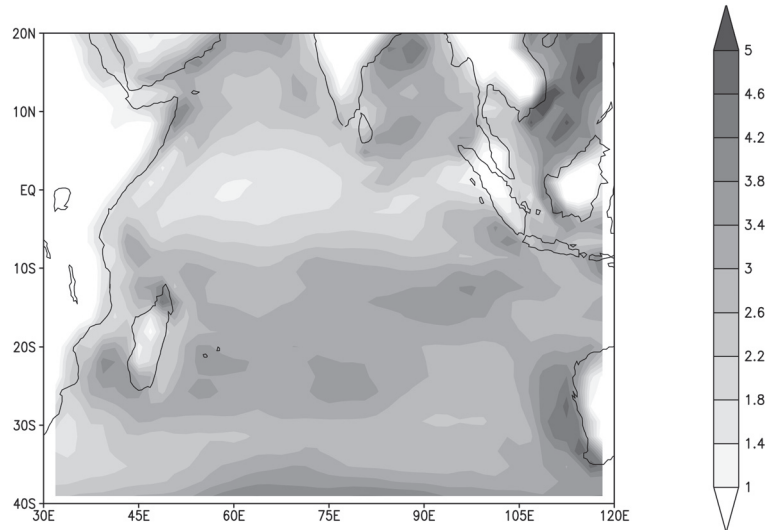


Figure 2.8: Standard deviation of the wind stress curl anomalies from NCEP model for 1948-2003. Only the seasonal mean was removed. There is a region of high variability in the Subtropical Indian Ocean to the east of Madagascar. For convenience the units of the curl variability are expressed in $10^{-8} Pa m^{-1}$.

The PCs of the three EOFs are shown in Fig. 2.11. In order to detect the dominant variability of the PCs, a spectral analysis was applied (not shown). The leading mode (EOF1) is dominated by quasi-biennial (QB) variability (i.e. 2-2.5 years). In addition, direct inspection of the PC1 (Fig. 2.12a) suggests the presence of interdecadal variability as well (i.e. the QB tendency seems to be stronger for the period 1970-1990). The spectrum of PC2 shows three significant peaks at periods of 3 years, 2 years and 1.5 years, while the PC3 has a primary peak at a period of 3.7 years and two secondary peaks in the QB range.

The pattern of EOF1 suggests that this mode is associated with changes in the large-scale Indian Ocean winds through a weakening of the center of the subtropical high in the south (see e.g. Fig. 2.1) and the trades in the tropical region. The forcing of this mode could be connected with the QB component of ENSO (Reason et al., 2000) or the tropospheric biennial oscillation (TBO) that regulates the strength of the monsoon (Meehl et al., 2003). On the other hand, EOF2 and EOF3 show significant interannual variability in the same range as that detected for the IOD (Fig. 2.7). Inspection of the times at which the PC2 (Fig. 2.11b) was active (i.e. events that are above (below negative) one standard deviation) reveals a predominance of ENSO and IOD events. In addition, there is a significant correlation between the PC2 and both IOD and SOI indices (± 0.45). The time series of the EOF3 (Fig. 2.11c) shows a relation between its positive phase and La Niña events, while its negative phase does not show any preference between IOD and ENSO phases, or other events.

A rotation analysis of the first twenty EOFs was performed using the varimax methodology (Richman, 1980). The spatial patterns of the first three rotated EOFs are similar to those

The wind stress curl over the South Indian Ocean: seasonal and interannual variability

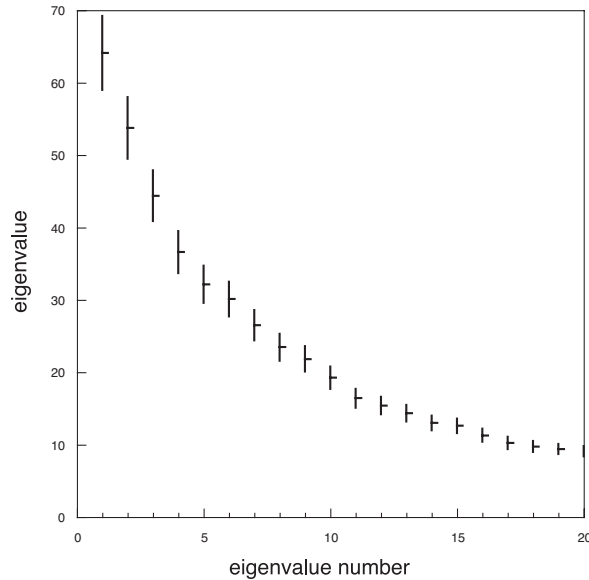


Figure 2.9: First twenty eigenvalues from an EOF analysis of band pass filtered wind stress curl anomalies. The eigenvalues are proportional to the fraction of the variance accounted for by each eigenvector. The error bars represent the standard error (one standard deviation error due to the sampling) according to North et al. (1982). It indicates that the first three EOF are statistically independent of each other.

shown in Fig. 2.10. After rotation, the first mode explains 80% of the variability of EOF1, but has a more localized center of variability in the south, with maximum correlations around 75°E (not shown). The second and third rotated modes are correlated to both EOF2 and EOF3, thus, they show the signature of the IOD forcing in the tropical Indian Ocean. Only the third rotated EOF displays significant negative correlations in the latitude band to the east of Madagascar up to 75°E, but compared to (Fig. 2.10c), positive correlations to south of 25°S are no significant. Therefore, the analysis indicates that the spatial patterns of the first three EOFs are robust. However, the spectral variability of the time series of the second and third modes lies in a broad range between 3-3.5 years and 2-2.5 years and the connections with individual ENSO and IOD events are less clear than with their unrotated counterparts. Thus, in the following, we investigate the temporal variability of EOF2 and EOF3 (non rotated) through a composite analysis of (unfiltered) wind stress curl anomalies at the times in which the modes were active.

Composites

For EOF2, 9 (13) out of 12 (16) years in which the negative (positive) phase was active, coincided with El Niño/IOD+ (La Niña/IOD-) events. Figure 2.12 shows a composite of wind stress curl anomalies at the times in which the negative phase was active from SON to JJA the following year. In SON an anticyclonic curl anomaly lies in the central-eastern

Low frequency variability of the wind stress curl

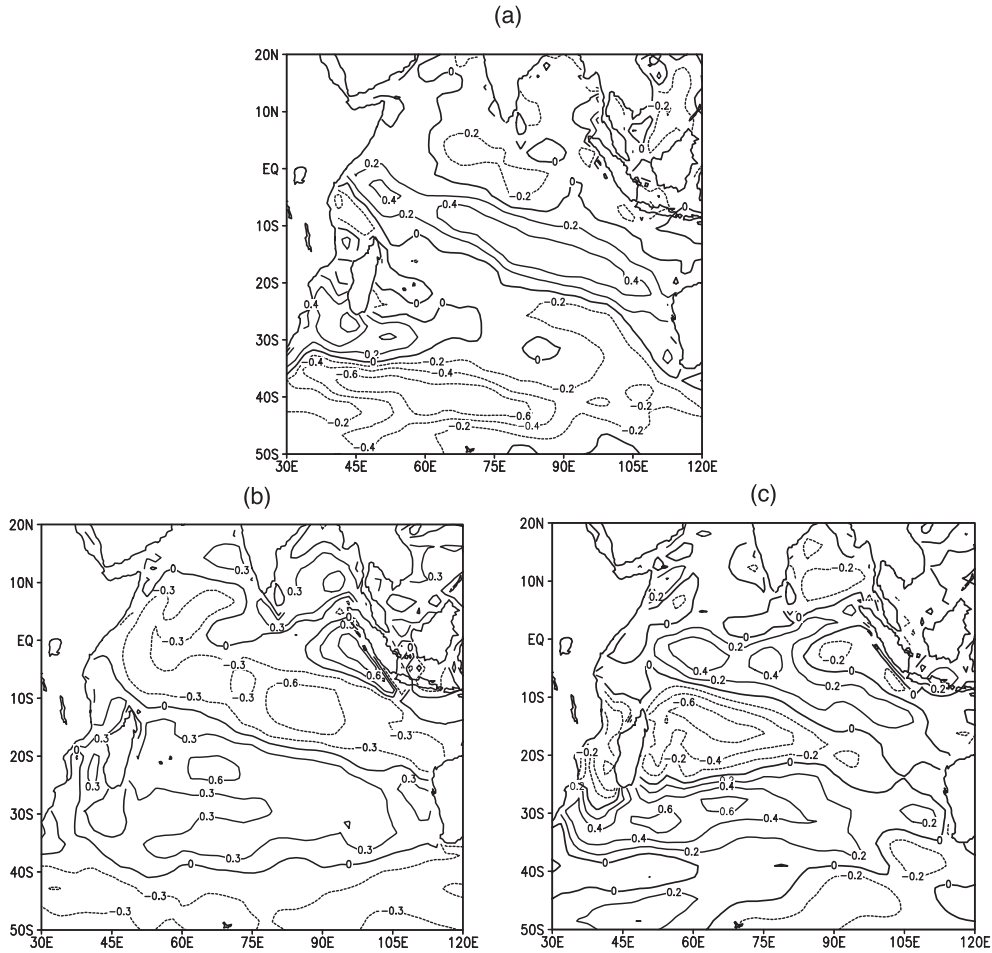


Figure 2.10: Correlation maps between band pass filtered wind stress curl anomalies and the time series or PC loadings of a) EOF1 (10.3%), b) EOF2 (8.7%) and c) EOF3 (7.1%). The time series were seasonally stratified (i.e. DJF, MAM, JJA and SON), and only the correlations for the SON-season are shown. Correlations higher than 0.3 are significant at the 95% confidence level based on a t-Student distribution for the correlation coefficient. Contour interval 0.2 (a, c) and 0.3 (b). The first pattern shows significant correlations in the Tropical Indian Ocean and over the southern basin around 40°S; the second pattern displays significant correlations in the eastern Tropical Indian Ocean; and the third pattern shows a large north-south dipole structure to the east of Madagascar.

Tropical Indian Ocean with its core around 12°S, while negative curl anomalies extend in front of Sumatra up to the Equator. These signals, related to equatorward extended trades and stronger southeast winds along Sumatra’s coast, are expected for a mature IOD+ (Saji et al., 1999; Huang and Kinter III, 2002). In DJF, the core of the anticyclonic curl and the coastal cyclonic curl shifts westward and southwestward, respectively (Fig. 2.12b). Notice that

The wind stress curl over the South Indian Ocean: seasonal and interannual variability

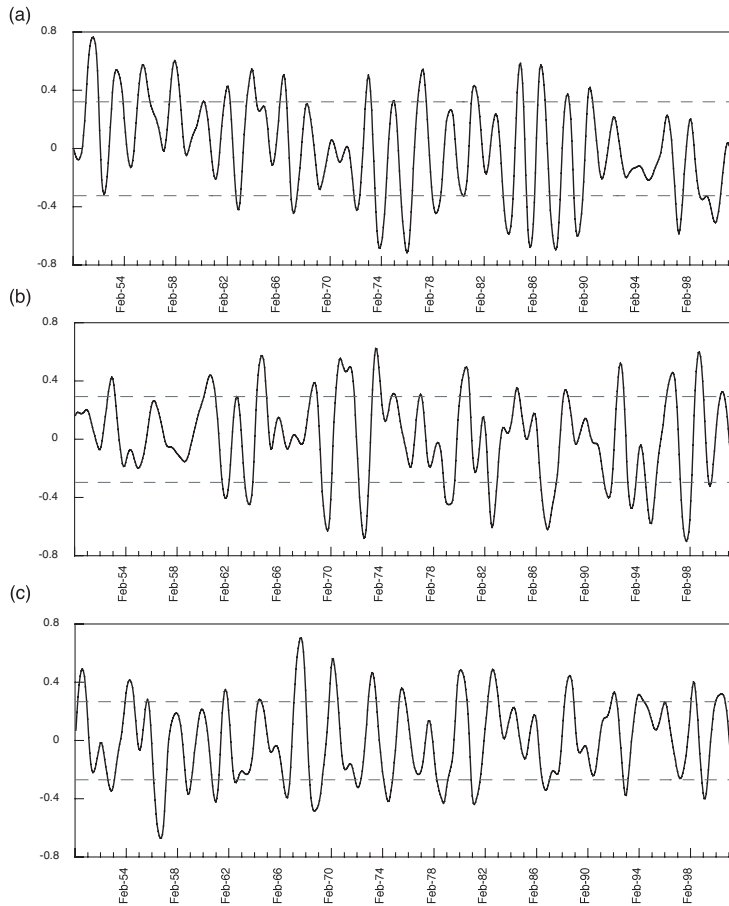


Figure 2.11: Principal component (PC) loadings of a) EOF1 (10.3%), b) EOF2 (8.7%) and c) EOF3 (7.1%). The PC loadings are obtained by dividing each eigenvector by the root mean square of the corresponding eigenvalue. The dashed grey lines denote the standard deviation of each PC. The PC1 presents significant variability at a period of around 2 years, while the PC2 and PC3 shows, in addition to quasi-biennial oscillations, significant interannual variability at periods of 3 years and 3.7 years, respectively.

east of Madagascar positive (negative) curl anomalies resemble the signature of EOF3 (Fig. 2.10c). In the next season, negative curl anomalies extend northeast of Madagascar and along the African coast (Fig. 2.12c), suggesting stronger southeasterlies during the development of the Southwest monsoon following an El Niño/IOD+. In JJA, during the peak of the monsoon, the cyclonic curl anomaly persists in the western Tropical Indian Ocean at both sides of the Equator, suggesting in particular stronger southeast winds northeast of Madagascar (Fig. 2.12d). Analysis of the mode's positive phase (i.e.during La Niña/IOD- events) shows similar anomalies in SON and DJF, although of relatively less amplitude (not shown).

Low frequency variability of the wind stress curl

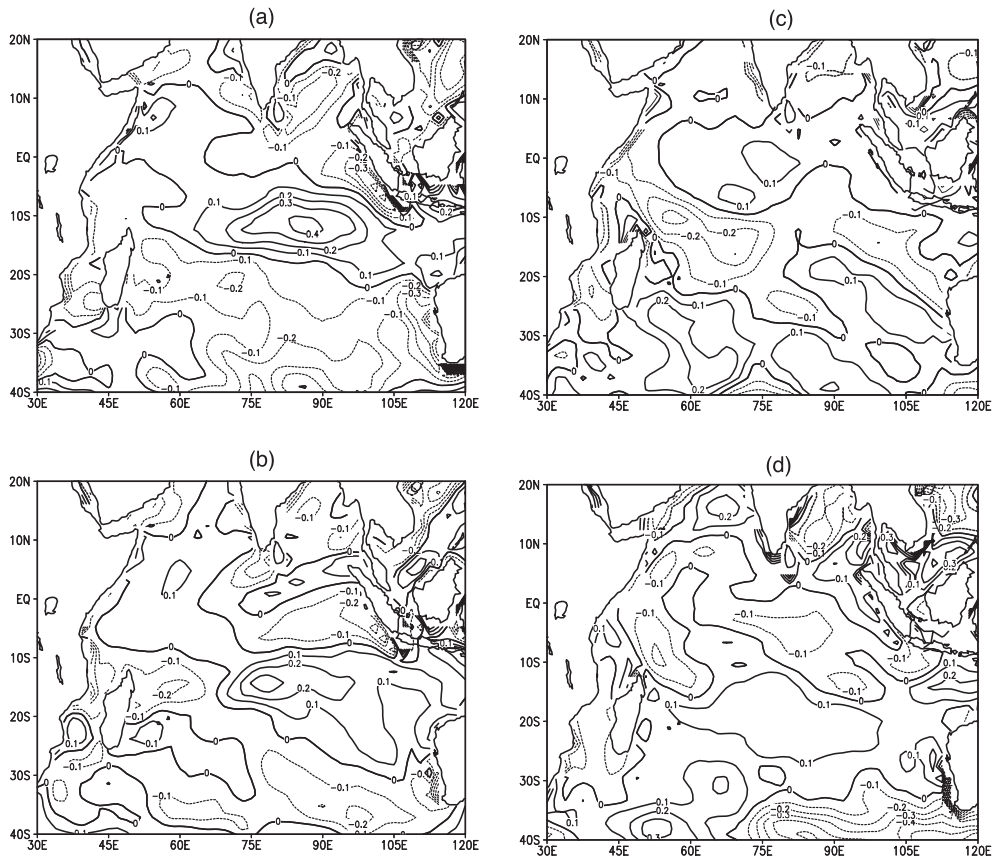


Figure 2.12: Composite of unfiltered wind stress curl anomalies during IOD+ and El Niño events in which the neagative phase of EOF2 was active, namely in 1961, 1963, 1969, 1972, 1982, 1987, 1994, 1997 for (a) SON, b) DJF, c) MAM and d) JJA. Units in $10^{-7} \text{ Pa m}^{-1}$.

The composite shown in Fig. 2.12 corresponds to years that were strong IOD+ and strong El Niño. It is interesting to analyze whether similar curl patterns appear during IOD and ENSO events that were not simultaneous (see Table 2.1). A composite based on three IOD+ events that were not ENSO years (i.e. 1953, 1961, and 1967) indicates similar curl anomalies in SON in the eastern Tropical Indian Ocean, with maximum anticyclonic curl north of 10°S , and anomalies fading off in the following seasons (not shown). During purely El Niño years, the maximum anticyclonic curl is found in the eastern Indian Ocean south of 10°S , with negative curl anomalies southwest of Sumatra (Fig. 2.13a). The anomalies weaken and extend southwestward in DJF (Fig. 2.13b). These patterns suggest that the influence of ENSO on the Indian Ocean equatorial zonal winds is much weaker than that during (simultaneous) IOD+ events, as previously suggested by Rao et al. (2002). Moreover, during purely El Niño events there are not curl anomalies along the western Indian Ocean in the region of the Southwest monsoon. During purely La Niña years, a cyclonic curl anomaly lies in the

The wind stress curl over the South Indian Ocean: seasonal and interannual variability

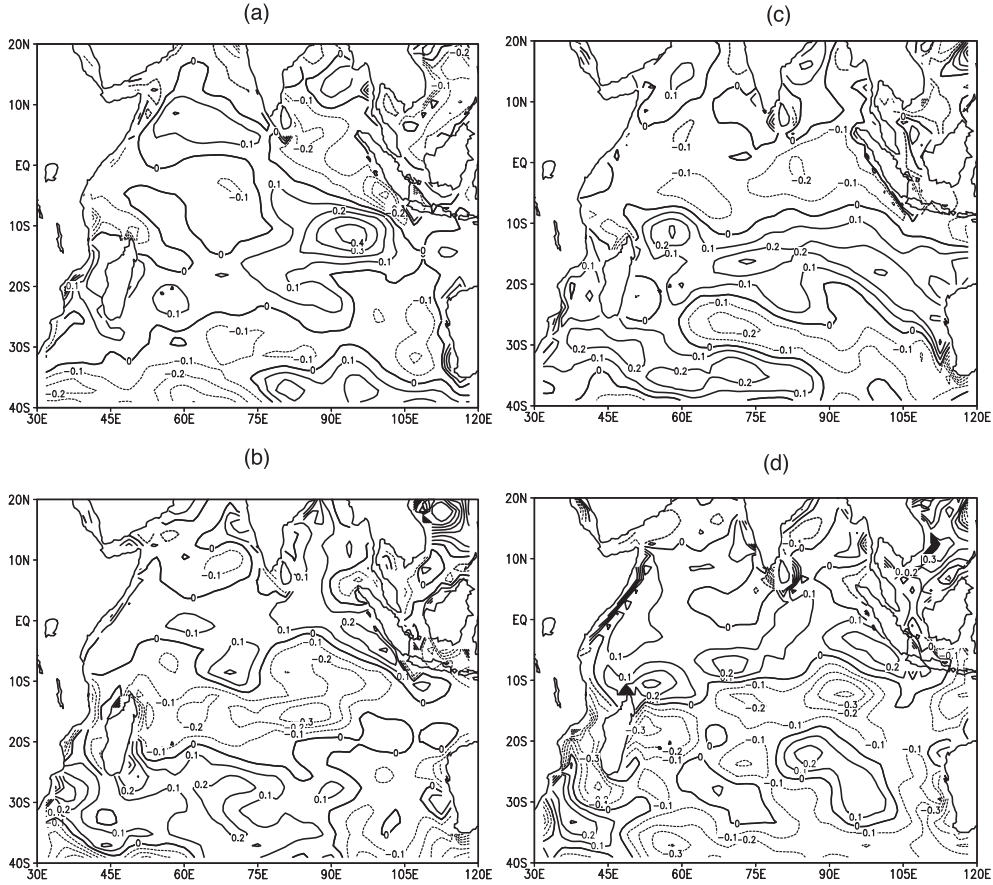


Figure 2.13: Composite of unfiltered wind stress curl anomalies for El Niño events that were not IOD+ years (i.e. 1951, 1957, 1965, 1969, 1976, 1987, and 2002) for SON (a) and DJF (c), and for La Niña events that were not IOD- years (i.e. 1950, 1970, 1988, and 1995) for SON (b) and DJF (d). Units in $10^{-7} \text{ Pa m}^{-1}$.

subtropical Indian Ocean with its core around 15°S (Fig. 2.13c). In addition, negative curl anomalies extend in the subtropical band $10^{\circ}\text{-}20^{\circ}\text{S}$ up to Madagascar (Fig. 2.13d) which, together with positive curl anomalies to the south form a dipole pattern similar to EOF3 positive phase (Fig. 2.10c). Indeed, the positive phase of EOF3 has been active in 17 years, of which 7 were normal El Niño years and 6 were protracted La Niña years (Fig. 2.11c). Analysis of wind stress curl anomalies during the former events indicates that the curl dipole pattern east of Madagascar initiates in SON and is fully developed between $10^{\circ}\text{-}30^{\circ}\text{S}$ in DJF (not shown).

Patterns of wind stress curl anomalies during protracted La Niña years are more difficult to analyze due to the irregularity of these events (Allan et al., 2003). Still, the curl distribution in the eastern Tropical Indian Ocean at the beginning of a protracted event is similar to that of

Low frequency variability of the wind stress curl

a typical La Niña. The PC3 indicates that during the second/third year of a protracted El Niña significant curl anomalies appear in the subtropical region to the east of Madagascar. This is illustrated in a composite of three protracted events: negative curl anomalies extend across the Indian Ocean basin between 10°-25°S, while a center of positive anomalies is present between 35°-40°S (Fig. 2.14).

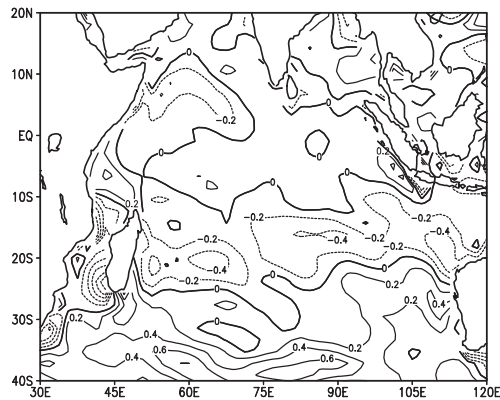


Figure 2.14: Composite of unfiltered wind stress curl anomalies associated with active peaks of the positive phase of EOF3 during protracted La Niña events in 1954-1956, 1973-1976, and 1998-2001. Composites for each event were computed as three monthly averages around October 1955, September 1975, and August 2000. Units in $10^{-7} \text{ Pa m}^{-1}$. The negative curl anomalies extend in the subtropical band 10°-25°S including the Mozambique Channel.

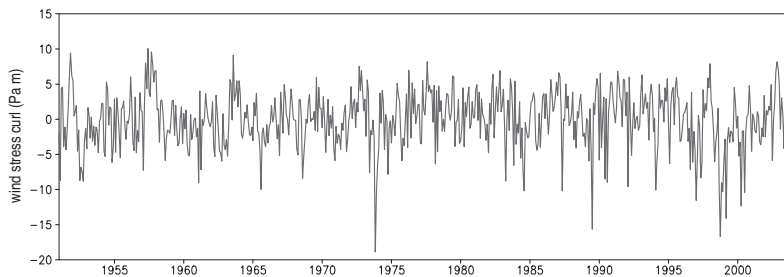


Figure 2.15: Time series of wind stress curl anomalies averaged over the center of maximum variability in eastern subtropical Indian Ocean [90°-100°E, 11°-16°S]. Units in 10^{-7} Pa m . It shows large negative peaks in November 1973, July 1989, October 1998, and April 2000.

The connection of the third mode with protracted La Niña events suggests the presence of decadal variability in the subtropical wind stress curl. Inspection of the curl anomalies averaged over the center of subtropical variability present in Fig. 2.8 (i.e. over 90°-100°E, 10°-15°S) reveals large amplitude negative peaks during protracted La Niña events in 1973,

1998 and 2000, and during the onset of the 1989 IOD- (Fig. 2.15). In addition, the occurrence of the protracted El Niño in 1991-1995, as well as IOD- events in 1992, 1993, and 1996, possibly induced a higher frequency of negative curl extremes in the first half of last decade. The correlation between the subtropical wind curl anomalies averaged over 70°-100°E, 10°-15°S and the SOI index is significant over the last decade (-0.6), with the curl lagging the SOI by 3 months.

2.5 Summary and discussion

In the first part of this Chapter we examined the seasonal variability of the wind stress curl over the Indian Ocean. ERS scatterometer winds reproduce the same large-scale patterns as seen from NCEP reanalysis data, although ERS high resolution produces smoother meridional gradients in the curl field. Observational (Schott and McCreary, 2001) and modeling (Woodberry et al., 1989) studies have shown that the changes in the Tropical Indian Ocean gyre circulations follow the seasonal curl reversals in agreement with Sverdrup dynamics. Analysis of the zonal component of the Sverdrup transport using ERS winds suggests a latitudinal variation in the core of the South Equatorial Current (SEC) between seasons. In February, three westward cores present in the basin east of 90°E seem to converge in the central basin into the SEC flow around 18°S, while in August a main westward core is found between 15°-20°S. Also, in the latter season maximum westward transport appears at Madagascar's northern tip. This wind driven flow could have an impact on the seasonal variations in the Mozambique Channel transport as seen from numerical model analysis (Biaostoch et al., 1999). It is puzzling though that such seasonal variation has not been observed from moored current meter arrays (Swallow et al., 1988; Ridderinkhof and De Ruijter, 2003).

The wind stress and wind stress curl around Madagascar were analyzed using 7 years of QuikSCAT winds. In particular, these high-resolution data enable to resolve small-scale curl features around islands (Chelton et al., 2004). Around Madagascar's southern tip the curl is cyclonic throughout the year, which might help establishing a permanent upwelling region there. Di Marco et al. (2000) described an upwelling event at Madagascar's southern coast and attributed it to upwelling favorable winds in February-March 2000, though another cause could be frictional interaction between the East Madagascar Current (EMC) and the continental slope as proposed by Lutjeharms and Machu (2000). Near Madagascar's northern tip a large-scale curl dipole is present from May to August. It forms as a consequence of the trade winds shadow behind Madagascar during the Southwest monsoon and the cyclonic curl that remains in the northern part of the Mozambique Channel from the previous season. The anticyclonic component of the dipole remains until November. Its possible impact on the regional circulation and/or interaction with eddies formed in the northern Mozambique Channel by barotropic instabilities of the SEC (Quadfasel and Swallow, 1986) needs to be clarified.

Changes in the wind stress curl induce variability in the ocean circulation on different time scales. Contrary to the seasonal variability of the gyres circulation associated with the wind monsoonal reversals (Woodberry et al., 1989; Hastenrath and Greischar, 1991), large-scale current variability in response to interannual curl anomalies have not been studied in the South Indian Ocean. Furthermore, a description of the spatial patterns and frequencies of

Summary and discussion

non-seasonal large-scale curl variability has been lacking. In the second part of this Chapter we performed an empirical orthogonal function (EOF) analysis in the time domain (T-EOF) to describe the first three modes of low frequency wind stress curl variability. Note that the EOF analysis using T-mode decomposition clusters spatial patterns that are recurrent in time (Richman, 1980). To investigate the characteristics of the modes temporal variability, additional methodologies like spectral analysis of the mode's principal component, or correlations with well-known climate indexes, are necessary.

The leading curl mode describes variations in the strength of the southern Indian Ocean winds and along the northward extension of the trades in the tropics, with dominant variability at quasi-biennial (QB) time scales. Changes in the intensity of the atmospheric anticyclone have been documented on interannual (Hermes and Reason, 2005) and interdecadal time scales (Allan et al., 1995). The QB variability in the Indian Ocean basin is in part related to ENSO. Reason et al. (2000) described QB signals in mean sea level pressure and SST over the Indian Ocean, but not in the winds. However, the correlation between the modes time series and the SOI is not significant. Variations in the intensity of the large-scale winds could be associated with strong/weak monsoon years. A component of TBO variability was detected in the tropical Indian Ocean SST and winds, but not in subtropical regions (Meehl et al., 2003). Thus, at this point, it is not possible to determine to which physical forcing the leading mode is related.

The second mode of wind stress curl is significantly correlated to both IOD and ENSO events, with variability at periods of 3 years and ~ 2 years. The latter may reflect the biennial tendency in the IOD that leads to the modes opposite phase the year following an event (Rao et al., 2002). This is controlled by the time it takes the subtropical Rossby waves to reach the western boundary, namely 1 year, where they trigger coastal Kelvin waves and subsequently equatorial Kelvin waves (Feng and Meyers, 2003). Curl anomalies persist in the western basin the year following positive IOD-ENSO events, with stronger southeasterlies northeast of Madagascar during the onset and peak of the Southwest monsoon, which is not apparent in only-ENSO years. These wind stress anomalies could have an impact on the activity of the next summer monsoon. Ashok et al. (2004) pointed out that the combined effect of ENSO and IOD on the summer monsoon over India in JJAS previous to the event peaks is different than that of ENSO alone. They showed that the IOD compensates, by anomalous low-level wind divergence in the eastern Tropical Indian Ocean, the deficit in rainfall over India induced by ENSO.

The third mode reveals a signal in the subtropical Indian Ocean between 10° - 35° S, with a particularly strong cyclonic circulation to the east of Madagascar and in the Mozambique Channel. The pattern suggests a southward shift of the line of zero mean wind stress curl that denotes the limit between the tropical and subtropical gyres. The positive phase of this mode is connected with both normal and protracted La Niña events. For normal La Niña events, curl anomalies are largest to the east of Madagascar in the DJF season. These anomalies also develop in the second and third year of protracted events, which have an interdecadal variability in the basin. The curl pattern of the third mode suggests a forcing of circulation anomalies around Madagascar. For example, a southward shift of the trades leads to changes in the latitude position and intensity of the SEC that progress into variability along its branches at the islands coast. Thereafter, alterations in the regional mesoscale eddy activity in the Mozambique Channel and south of Madagascar could be expected. In this sense,

The wind stress curl over the South Indian Ocean: seasonal and interannual variability

wind forcing associated with La Niña events may have an impact on the circulation in the Southwest Indian Ocean. Over the last decade, the 1997 IOD+/El Niño was followed by the protracted La Niña in 1998-2001. Anomalies in the mesoscale eddy activity south of Madagascar were reported during this period by De Ruijter et al. (2004), as the appearance of regular and frequent dipole pair formation that ultimately interact with the Agulhas Current and its retroflexion south of Africa. They suggested that these changes could be related to variability of the East Madagascar Current (EMC) near its separation point. On the other hand, periods of reduced eddy activity in the Mozambique Channel occurred in early 1996 and 1998 (Schouten et al., 2003). The influence of local or remote wind stress curl forcing on the flow through the Channel and around south Madagascar has not been analyzed yet. In the next Chapter, we investigate in detail the effect of the IOD/ENSO events during last decade on the variability of the boundary currents around Madagascar and possible impacts on the regional mesoscale eddy variability.

Chapter 3

Low-frequency eddy-variability around Madagascar: links to the Indian Ocean variability

3.1 Introduction

The mesoscale activity around Madagascar is related to the large-scale Indian Ocean circulation. The South Equatorial Current (SEC) flows westward between 10° - 20° S and, on reaching the Madagascar coast at $\sim 17^{\circ}$ S, splits into two branches (Fig. 3.1). The northward branch forms the North Madagascar Current (NMC) at the northern tip of the island, while the southern branch feeds into the East Madagascar Current (EMC) (Swallow et al., 1988). The flow of the SEC north of Madagascar bifurcates again at the African coast where it forms the East African Coastal Current (EACC) to the north and the Mozambique Current to the south. Recent hydrographic measurements in the narrows of the Mozambique Channel however, did not detect a continuous western boundary current; instead southward migrating anticyclonic eddies appeared to dominate the flow (de Ruijter et al., 2002). Such eddies have also been suggested by satellite tracking of sea level anomalies (Gründlingh, 1995; Schouten et al., 2002a), and were simulated in a numerical model (Bjastoch and Krauss, 1999). Suggested mechanisms for eddy formation are barotropic instability of the SEC north of the Mozambique Channel (Quadfasel and Swallow, 1986) and shedding related to the geometry of the narrow section of the Channel when during strong current events the northern anticyclonic loop is pushed through the constriction (Ridderinkhof and de Ruijter, 2003). At the southern tip of the island the EMC seems to experience a retroflexion, in which eddies are shed from the current (Lutjeharms, 1988). Westward continuation toward the African coast is another possible regime for the EMC after separation from the shelf (Quartly and Srokosz, 2004). Satellite altimetry revealed cyclonic and anticyclonic eddies in the region south of Madagascar propagating (south) westward toward the Agulhas Current (AC) (Gründlingh, 1995; Schouten et al., 2003; Quartly and Srokosz, 2004).

The eddy activity in the Mozambique Channel is dominated by a frequency of 4 to

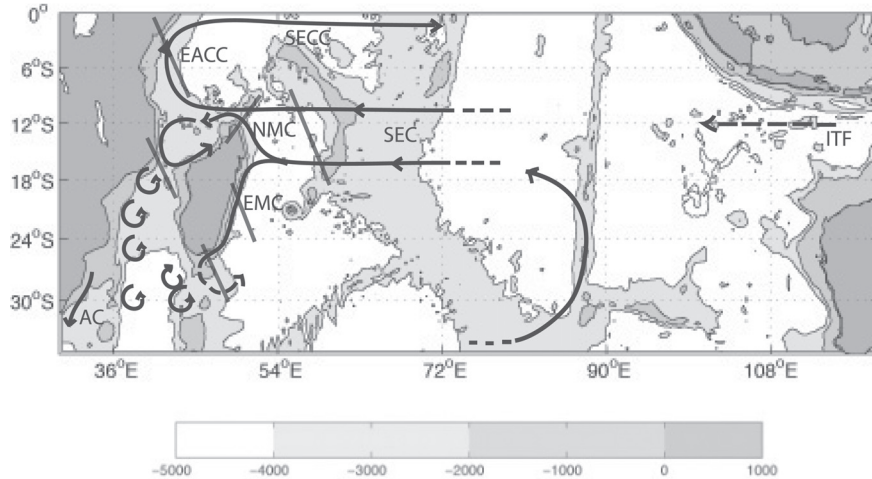


Figure 3.1: Schematic general circulation of the south Indian Ocean (SIO). North of 12°S the South Equatorial Current (SEC), East African Coastal Current (EACC) and SEC Countercurrent (only during the summer monsoon season, DJF) form the tropical gyre in the SIO. South of 12°S the SEC forms the northern boundary of the SIO subtropical gyre, and it splits at the coast of Madagascar into the North Madagascar Current (NMC) and East Madagascar Current (EMC). Eddies dominate the flow in the western Mozambique Channel and at around 27°S the Agulhas Current (AC) is formed along the African coast. The Indonesian Throughflow (ITF) enters the SIO basin between 10° - 15°S . Sections along six satellite tracks used to derive geostrophic velocity anomalies are shown with gray thick lines.

5 times/year (Schouten et al., 2002a). Analysis of in situ and satellite observations revealed interannual variability in this frequency from 1996 to 2000, for instance hardly any eddies were detected in the first halves of 1996 and 1998 (Schouten et al., 2003). According to Schouten et al. (2002b), the rate of eddy formation is modulated by varying equatorial winds via an oceanic teleconnection across the Indian Ocean: equatorial Kelvin waves arrive at the coast of Sumatra at frequencies of 4 times/year, they continue southward as coastal Kelvin waves and subsequently trigger Rossby waves at the same subannual frequency. Anomalous equatorial easterlies associated with the 1994 and 1997 ENSO/IOD modes interrupted this chain of events, leading to less eddies in the Mozambique Channel after a lag related to the time it takes the Rossby waves to cross the basin along 12°S to Madagascar.

The eddy activity south of Madagascar is also connected to the basin Rossby wave variability at frequencies of 4 times/year (Schouten et al., 2002a). In addition, de Ruijter et al. (2004) discovered and measured hydrographically large pairs of counter-rotating eddies or dipoles in this region, and they followed their migration into the Agulhas Retroflexion system. From August-1996 to May-1997 and from May-1999 to June-2000 frequent and regular dipole formation occurred, separated by a period in which hardly any dipoles or eddies were formed. Periods of regular dipole formation could be a response to a strengthening and increase of the cyclonic activity of the EMC due to large-scale interannual sea level anomalies from the negative phase of the ENSO/IOD (de Ruijter et al., 2004). Remarkably, the inter-

Data

action between the train of dipoles in 2000 and the AC caused an anomalous eastward shift of the Agulhas retroflexion that lasted almost half a year. No Agulhas Rings were formed during that period.

Therefore, the processes by which the interannual tropical climate anomalies can influence the low frequency eddy variability of the Mozambique Channel and South Madagascar regions need to be further investigated. In addition to ocean dynamics related to the IOD/ENSO events, a direct response to low frequency atmospheric forcing could be expected (Chapter 2). The dynamics of the IOD in the subtropical Indian Ocean are related to a downwelling Rossby wave forced by positive wind stress curl anomalies in the eastern basin (Rao et al., 2002). This wave intensifies on the way due to a positive convolution with the wind (Feng and Meyers, 2003). Within an OGCM, Masumoto and Meyers (1998) also found that the Ekman pumping in the Indian Ocean between 5° - 15° S has a modifying effect on interannual waves radiating from the eastern boundary. According to Xie et al. (2002), ENSO is the principal forcing of subtropical Rossby waves in the Indian Ocean along 10° S, whereas the IOD exerts a secondary contribution. They showed that these waves are an important factor in controlling sea surface temperature (SST) variability in the western Indian Ocean through thermocline-surface feedbacks. Other ENSO signals enter the Indian Ocean as coastal Kelvin waves propagating along the coast of Indonesia and subsequently as Rossby waves triggered off the western Australian coast, but these are attenuated in the central basin by the local wind stress forcing (Wijffels and Meyers, 2004).

The goal of this Chapter is to investigate whether and how large-scale sea surface height (SSH) anomalies generated in the tropical Indian Ocean (IO) during the IOD impact the dynamics and variability in the region around Madagascar (i.e. between 12° - 25° S) and, eventually, introduce the observed year-to-year variation in the local mesoscale eddy field. After presenting the data in Section 3.2, Section 3.3 deals with the description of interannual variability in the SSH and eddy kinetic energy (EKE) around Madagascar, based on the longest available period of satellite altimetry observations, i.e. over 10 years. In Section 3.4 we analyze the propagation of large-scale SSH anomalies in the subtropical IO through a lag correlation analysis with an IOD index, and examine the modifying role of the subtropical wind stress curl variations along such propagation paths. Large-scale SSH anomalies near Madagascar will alter the local current regimes and their stability characteristics. Therefore, velocity variations in the branches of the SEC as well as in the boundary currents at the African and eastern Madagascar coasts are analyzed, and connections between the current anomalies and eddy variability are discussed (Section 3.5).

3.2 Data

In this study we use SSH measurements from the TOPEX/Poseidon (T/P) and ERS satellite missions processed and merged on a $1/3^{\circ}$ Mercator grid by the CLS Space Oceanography Division, France. The data cover the period October 1992 to January 2004, with a time spacing of one week. The T/P satellite has a 10-day repeat orbit period and ERS has a 35-day repeat orbit period (SSALTO/DUACS handbook, 2004)¹. From December 1993 to March

¹SSALTO/DUACS is the CNES (Centre National d'Etudes Spatiales) near-real time and delayed time multi-mission altimeter data processing system. At the beginning of 2004, DUACS was defined as the Data Unification

1995 ERS data are not available due to problems in the satellite orbit. Thus, we only use the T/P data set, which reduces the spatial resolution of the final product for that time period, as the number of tracks performed by T/P per cycle is less than those of ERS, i.e. for T/P the cross track distance at the Equator is 315 km, while for ERS the maximum distance between tracks is about 80 km. Mapping errors in percentage of the signal variance are also obtained for each weekly SSH field. In addition to the gridded SSH product, we analyze combined along-track SSH data from T/P and ERS. In this product, the along-track distance between SSH observations is about 6 km. We use these data in Section 3.5 to study the variability of western boundary currents that intercept satellite tracks.

The domain of the study covers the IO region from 50°S to 20°N and from 30°E to 120°E. SSH anomalies (SSH from now on) were computed by removing the mean per calendar month from each monthly mean observation. For the analysis in Section 3.4, SSH were further low pass filtered using a Lanczos filter with a cut off frequency of 0.125 months⁻¹ (Duchon, 1979). As the filter response function varies from 1 to 0 at frequencies from 0.094 months⁻¹ to 0.155 months⁻¹ by low pass filtering it is expected that energy at periods higher than 11 months remains unaltered.

We also make use of monthly means of SST and zonal and meridional momentum flux from the NCEP Reanalysis data set (Kalnay et al., 1996). Monthly anomalies were computed for the period 1992-2003 in the same way as for the SSH data. Finally, in Section 3.5.2 we use the ocean absolute dynamic topography from Rio and Hernandez (2004). This combined mean dynamic topography (CMDT-RIO03) is computed with a multi-variate analysis using hydrographic data, surface drifter velocities and altimetry. CMDT-RIO03 corresponds to the mean over the period 1993-1999 and is available over a 1°x1° grid.

3.3 SSH and EKE variability around Madagascar

Two routes of high SSH variability from the region around Madagascar converge into the AC path south of 25°S: one originates around 15°S in the Mozambique Channel and continues south along its western side; the second one comes from the southeastern side of Madagascar and extends westward south of the island (Fig. 3.2a). Most of the variability along these paths is related to the mesoscale eddies detected in the area (Gründlingh, 1995; Schouten et al., 2003; de Ruijter et al., 2004). Indeed, the variability of the high passed SSH (Fig. 3.2b) shows that most of the variance is contained in the mesoscale field, whereas the low frequency SSH variability has spatially the same distribution as the high frequency component but with less amplitude (Fig. 3.2c). The two routes around Madagascar are in turn influenced by SSH variability along two zonal bands extending in the IO around 12°S and 24°S (Fig. 3.2a). These bands show significant Rossby wave activity at frequencies of 4-5 times/year (Schouten et al., 2002a). In particular, the origin of the variability along 24°S is related to eddies from the Leewind Current propagating westward up to 90°E (Fang and Morrow, 2003) and to baroclinic instability of the large-scale currents in the central basin (Palastanga et al., 2007).

To investigate the year-to-year variations in SSH, we analyze time series in five selected regions around Madagascar (Fig. 3.2a). The North Madagascar region (NM) lies in an area where eddies are formed by instabilities of the SEC/NMC-free jet (Quadfasel and Swallow,

Altimeter Combination System.

SSH and EKE variability around Madagascar

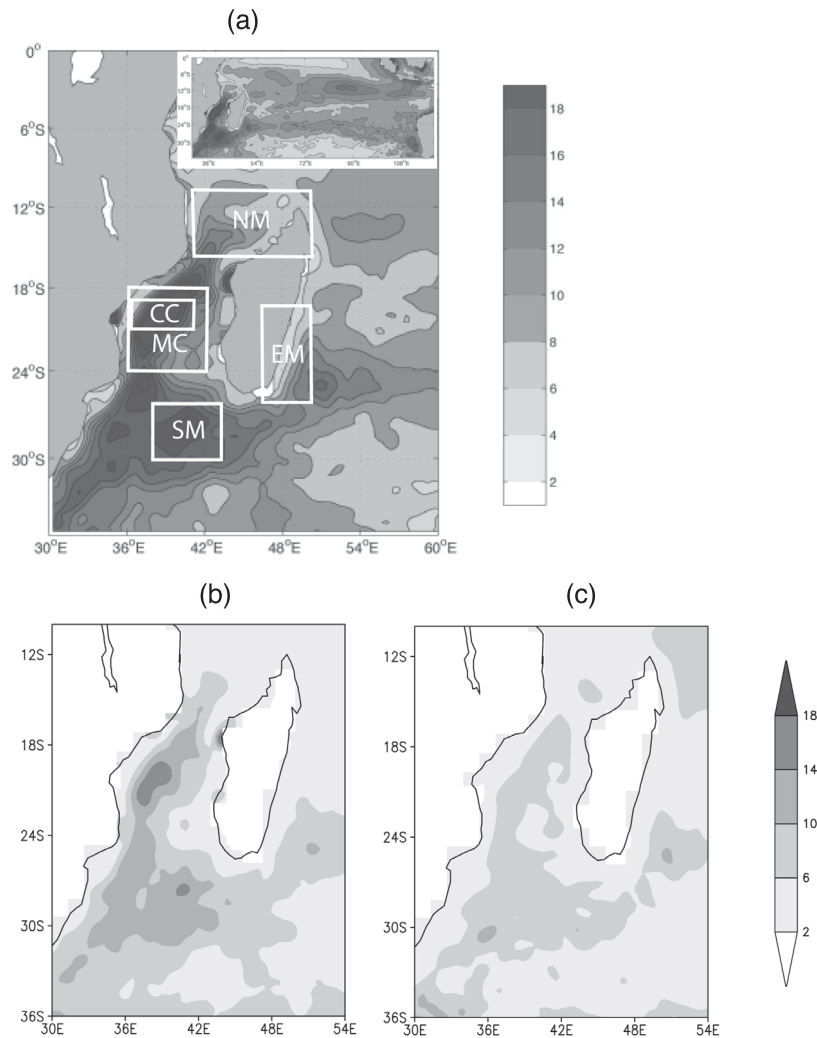


Figure 3.2: Fig. 3.2 a) Standard deviation of SSH anomalies from the combined T/P-ERS data set for the period 1993-2003. Five boxes in the graph display regions selected for a time series analysis, namely North Madagascar (NM), central Mozambique Channel (MC), region inside MC (CC), East Madagascar (EM), and Southwest Madagascar (SM). In the right upper corner the variability over the South Indian Ocean is shown. b) Standard deviation of the high passed SSH anomalies. A Lanczos filter with a cut off frequency of $0.125 \text{ months}^{-1}$ was applied. c) Same as b) but for the low passed SSH anomalies. Units in cm.

1986) and where SSH anomalies arrive from the IO at interannual and shorter time scales (Perigaud and Delecluse, 1993; Schouten et al., 2002a). In the Mozambique Channel between 18° - 24° S (MC) the high frequency SSH variability is related to regular southward traveling

eddies. A small region in the center of MC (i.e. CC) is also selected. This is because the mesoscale field in the Channel exhibits changes from north to south, i.e. the frequency of eddy variability decreases from 7 times/year in the north to 4 times/year in the center, and there is an increase in the eddy SSH toward the south (Schouten et al., 2003). It is thus expected that CC captures better intrinsic signals of eddies passing by than the larger MC. The region southeast of Madagascar (EM) includes both the variability of the EMC and from further offshore. The region southwest of Madagascar (SM) intercepts variability coming from the 24°S band in the IO, as well as eddies detached from the EMC after it separates from the coast to continue its path either westward or to retroflect eastward (Quartly and Srokosz, 2004).

3.3.1 SSH interannual variations

The SSH in NM and MC exhibit an interannual fluctuation that can be compared to the IOD evolution (Fig. 3.3a). An IOD index based on the difference of SST anomalies between the western tropical IO and the southeastern tropical IO (Saji et al., 1999) is also shown. Positive (negative) IOD events took place in 1991 (1992), 1994 (1996) and 1997 (1998), but the 1991/1992 events were of lesser importance and will not be considered in this study. The year after the first positive (negative) IOD event, positive (negative) SSH appear in the two areas. However, after the second IOD cycle (i.e. 1997/1998) a two year period of positive SSH is followed by a two year period of negative SSH. In EM and SM, the SSH is dominated by fluctuations at shorter time scales (Fig. 3.3b,c). Nonetheless, the EM region shows an interannual oscillation similar to that in NM and MC, with positive SSH in 1995 and from late 1997 to mid-1999, the latter followed by negative SSH until 2001 (Fig. 3.3b). The SSH in SM lag those in EM by a few months, and have relatively high frequency oscillations (Fig. 3.3c). This may be related to local dynamical processes of the separating EMC. Moreover, the SM region lies in an area that could be directly affected by variability of the large-scale subtropical IO circulation, including the anticyclonic recirculation gyre in the southwest corner of the basin (Stramma and Lutjeharms, 1997).

It is possible that the interannual variability seen in the SSH field around Madagascar is related to ENSO events that occurred simultaneously to the IOD. An analysis of ENSO signals over the IO (Nicholson, 1997) revealed significant coherence between the SST in the Mozambique Channel and South Madagascar regions and the SOI index at periods of 4-6 years and in the quasi-biennial range. It is likely that Indian Ocean dynamics are involved in transferring ENSO signals into the western tropical basin (Klein et al., 1999). A spectral analysis of the SSH in NM, MC and EM reveals peaks at a period of 4.5 years ($0.019 \text{ months}^{-1}$) (Fig. 3.4). The peaks are close to the 95% confidence level from a red noise background estimation and are significant at the 90% confidence level. They could reflect the oscillation seen in the time series from mid-1997 to mid-2001 after the strong 1997/1998² IOD/ENSO events (Fig. 3.3a). The spectrum of the IOD presents variability at relatively short periods of ~ 3 years (Fig. 2.7), suggesting that the low frequency SSH variability around Madagascar could be more influenced by ENSO than by the IOD. However, it is not possible to draw firm conclusions on this interannual period from a 10 year record. Finally, the SSH in SM show

²Note that the years 1998-2001 correspond to a protracted La Nina event. See Table 2.1 for more details.

SSH and EKE variability around Madagascar

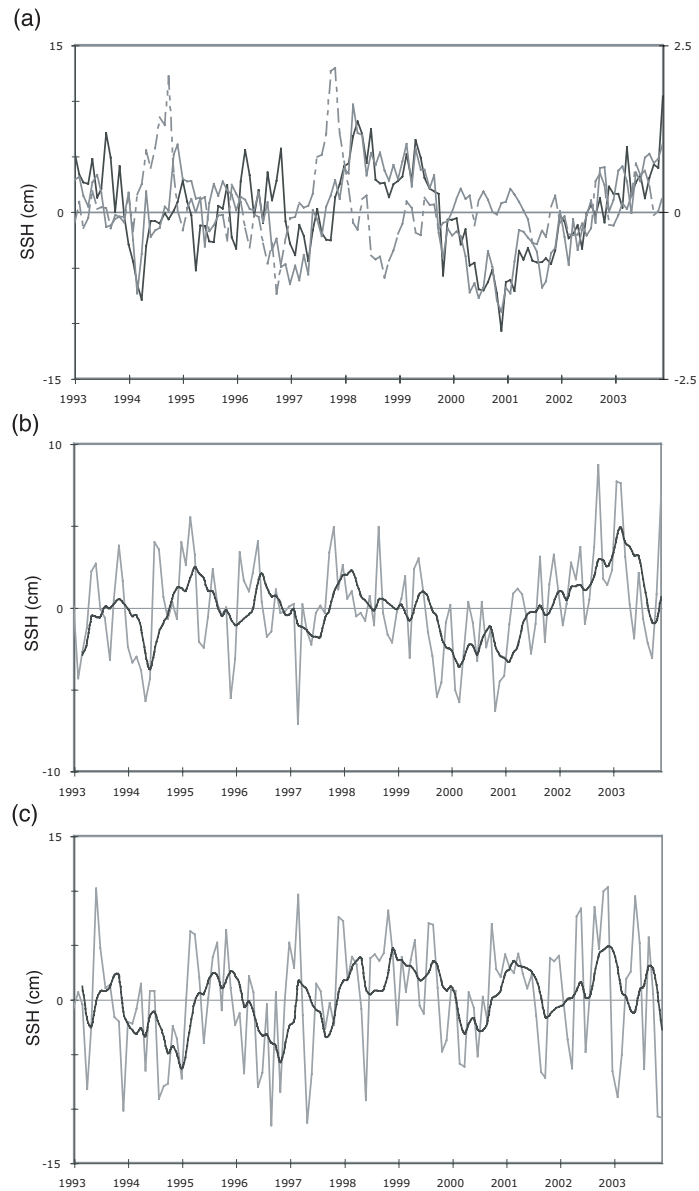


Figure 3.3: Time series of averaged SSH anomalies in the regions a) North Madagascar (gray line) and central Mozambique Channel (black line), b) East Madagascar, c) Southwest Madagascar. In Figures 3.3b and 3.3c a five month running mean of each series is added (black line). In Figure 3.3a the dashed-dotted line denotes the IOD index of Saji et al. (1999), with units in $^{\circ}\text{C}$.

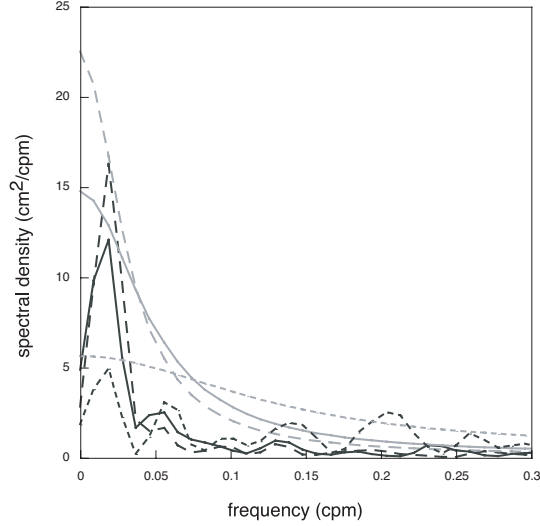


Figure 3.4: Spectral density cm^2/cpm ($\text{cpm}=\text{cycles per month}$) versus frequency (per month) for the SSH time series in the regions North Madagascar (dashed line); central Mozambique Channel (solid line), and East Madagascar (dotted line), with 95% confidence bands in grey for each of the regions (same lines). Spectral peaks were tested with a red noise spectra and its confidence bands at the 90% and 95% significance level as discussed in the text.

variability at subannual time scales (0.1 months^{-1}) and, though not significant, at a period of 2 years ($0.046 \text{ months}^{-1}$) (not shown).

3.3.2 EKE interannual variations

To measure changes in the mesoscale activity around Madagascar, we compute time series of EKE in the MC, CC and SM regions (Fig. 3.5). First, the geostrophic velocity anomalies are estimated from the zonal and meridional SSH gradients

$$\begin{aligned} u' &= -\frac{g}{f} \frac{\partial h}{\partial y} \\ v' &= \frac{g}{f} \frac{\partial h}{\partial x} \end{aligned}$$

Subsequently, the EKE per unit mass is obtained as

$$EKE = \frac{1}{2} (u'^2 + v'^2)$$

This EKE estimation represents only energy contained in anomalous surface currents under the geostrophic assumption. Schouten et al. (2003) combined T/P derived geostrophic

SSH and EKE variability around Madagascar

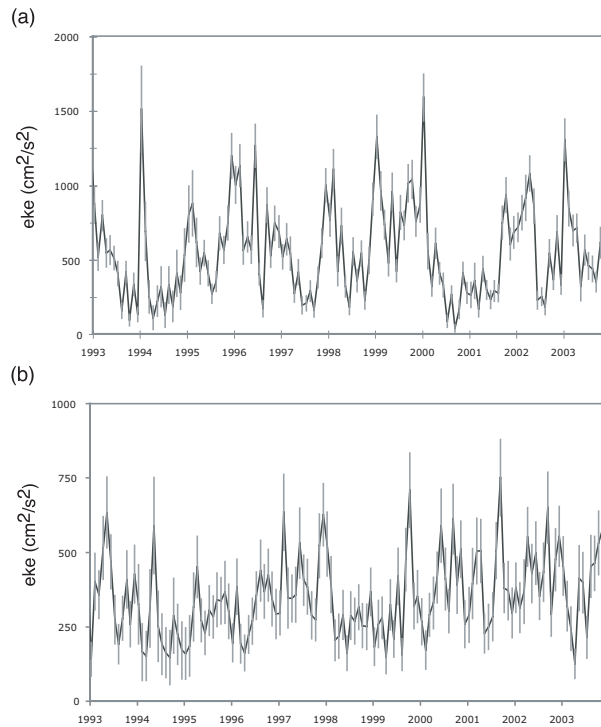


Figure 3.5: EKE time series in (a) the central Mozambique Channel and (b) southwest of Madagascar. Error bars for each monthly EKE estimation are shown with gray segments. Errors are available as a percentage of the signal variance for each weekly SSH field. Units in $\text{cm}^2 \text{s}^{-2}$.

velocity anomalies with in situ LADCP data to estimate total velocities in the Mozambique Channel, and found a good correlation between the direction of the estimated total geostrophic flow and independent mooring observations. If we assume that the mean currents in MC are rather weak, and the same for the SM region, then geostrophic velocity anomalies may constitute a good indication of the variability due to eddies in these regions. Since the high resolution ERS data are not available from December 1993 to March 1995, EKE estimations during that period are not adequate for studying eddy features, which are typically 250-300 km wide around Madagascar (de Ruijter et al., 2002; de Ruijter et al, 2004). Therefore, EKE variations will be only discussed from late 1995-onwards. Estimates of the errors in the EKE computations are given for each region. Overall, the errors are larger in SM than in CC, but even in the former the amplitude of the interannual EKE variation is significant.

The central Mozambique Channel (CC) shows periods of high EKE (i.e. highly energetic eddies) in late-1995/1996, around 1998 and in 1999; and of low EKE in 1997 and in 2000/2001, with an average EKE amplitude of $600 \text{ cm}^2 \text{ s}^{-2}$ (Fig. 3.5a). Interestingly, this EKE interannual variation is not present in the northern region of the Mozambique Channel. This is because, although most of the EKE peaks associated with a positive SSH anomaly in CC

could be traced northwards to about 1-2 months earlier, there is a change in the SSH amplitude towards CC that induces the observed low-frequency variability. The EKE averaged over the larger region MC shows similar characteristics to CC (Fig. 3.5a). The interannual variation in the EKE of the central Channel matches well with periods of positive and negative SSH (Fig. 3.3a). In particular, there is a significant correlation of 0.49 between the SSH and the EKE in the MC region.

South of Madagascar, periods of high EKE are present from August-1996 through 1997 and from October-1999 until 2002, separated by an EKE minimum spanning the second half of 1998 to mid-1999 (Fig. 3.5b). The high EKE peaks can be associated with the periods of regular dipole formation from de Ruijter et al. (2004). Due to the availability of data at that time, de Ruijter et al. (2004) could only track dipoles and analyze their variability from 1996 to 2000. Here we have extended the analysis to 2003 and found that after the train of 2000, two more dipoles were formed, namely in January 2001 and April 2001. Thereafter, no dipoles were observed until 2003. The EKE peaks in 2002 correspond to anticyclonic SSH anomalies. Dipole features were observed again in April 2003, July 2003 and December 2003, though of relatively small size and amplitude, which results in lower EKE peaks (Fig. 3.5b).

A spectral analysis of the EKE in CC shows significant variability (90% confidence level) at periods of 1 year and ~ 3 years, whereas SM has dominant variability around 5 years, though not significant (not shown). Both regions show a significant correlation with the IOD index (i.e. 0.47 in CC at a lag of 20 months and -0.29 in SM at a lag of 15 months, with EKE lagging the IOD), suggesting that a link between the EKE interannual variability in these regions and the IOD cycle could exist. In the following, an explanation for lags and mechanisms for such a response to the IOD is examined.

3.4 Large-scale response of the SSH to the IOD

In this section, we describe the evolution of the basin scale SSH during the IOD cycles of the last decade, i.e. the events 1994/1996 and 1997/1998. The pattern of SSH or heat content anomalies during the peak of a positive event (IOD+) is well known from previous studies (Webster et al., 1999; Rao et al., 2002). This is illustrated in Fig. 3.6a as a composite of SSH for boreal autumn (SON). In response to anomalous cooling, the thermocline is shallower in the eastern IO from 10°S to 10°N , while the deepening of the thermocline at both sides of the Equator represents westward propagating Rossby waves. On the other hand, the negative phase of the IOD (IOD-) has been less well described. A composite of the IOD- in 1996 and 1998 (Fig. 3.6b) shows some differences with respect to the IOD+. For instance, the SSH extend over a smaller area of the central eastern IO; in particular they do not reach the region north of Madagascar. This is probably related to differences in the extension of the wind forcing itself (Chapter 2). In addition, the amplitude of the SSH front off Sumatra is 5 cm less than that during the IOD+. A weaker feedback mechanism to strengthen the original SST anomaly is expected during the IOD-, when only an intensification of the equatorial westerlies occurs, than during the IOD+, when the winds along the Equator reverse, leading to a strong coupling with the atmosphere (Saji et al., 1999).

A lagged correlation analysis between the time series of the IOD index (Fig.3a) and the

Large-scale response of the SSH to the IOD

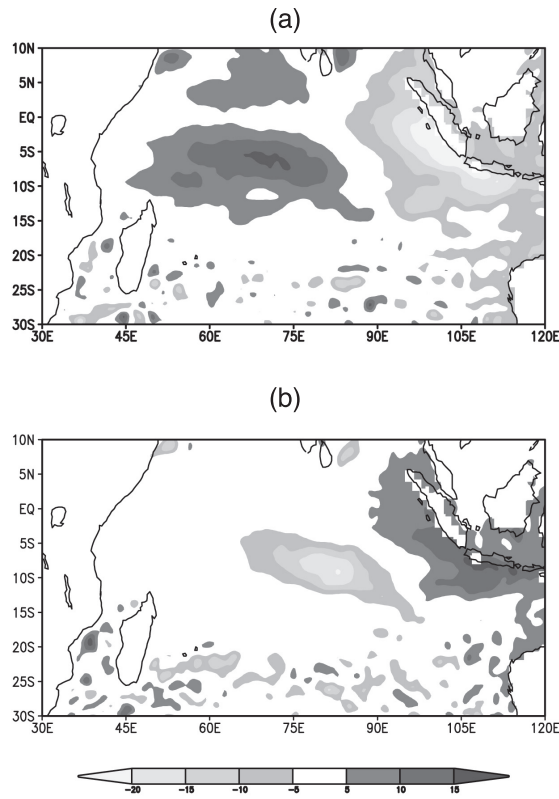


Figure 3.6: *Composite of SSH anomalies during the boreal autumn season (SON) for the two strong positive IOD phases of the last decade (1994 and 1997). b) Same as Figure 3.6a, but for the two negative IOD phases (1996 and 1998). Units in cm.*

basin SSH with a six-monthly increasing lag between both variables is presented in Fig. 3.7. To focus on interannual time scales, SSH anomalies were low pass filtered (Section 3.2). Note that only correlations higher than 0.4 are significant at the 90% confidence level, based on a t-student distribution of the correlation coefficient for a basin average and with the degrees of freedom of the SSH estimated from the autocorrelation function of the low-passed anomalies.

From lags of 1 to 13 months the correlations are consistent with the description of the IOD (subtropical) dynamics by Feng and Meyers (2003). Basically, after the peak of the IOD+ (1 month time lag) negative correlations propagating south along the coast of Indonesia represent coastal Kelvin waves that enter the IO basin between 5°-20°S as downwelling Rossby waves. These correlations split near 95°E into tropical and subtropical bands (7 month time lag), while a large-scale positive correlation pattern is seen east of Madagascar and north of 18°S due to downwelling subtropical Rossby wave forced during the IOD+. After the peak of the IOD- (13 month time lag), negative correlations in the central subtropical

Low-frequency eddy-variability around Madagascar: links to the Indian Ocean variability

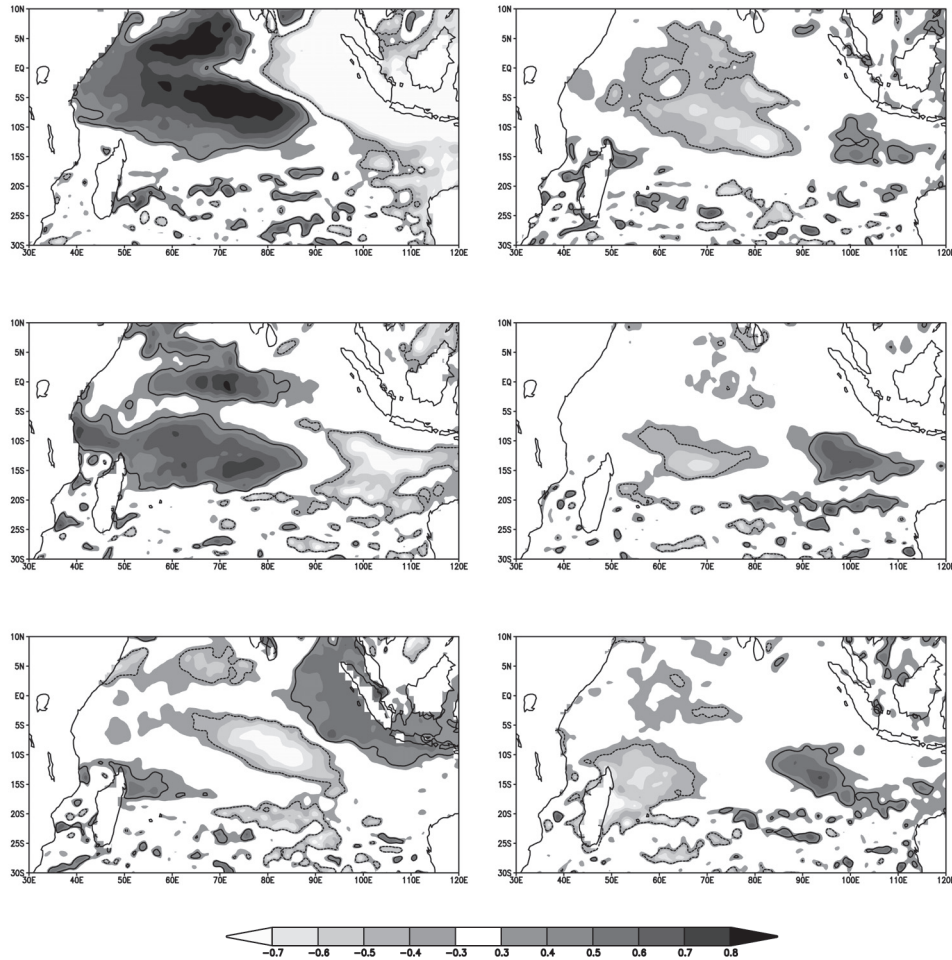


Figure 3.7: Correlation patterns between the IOD index (Saji et al., 1999) and the basin low-pass filtered SSH. For every spatial point of the Indian Ocean the correlation coefficient of the IOD index time series with the SSH time series is calculated at the lags shown, with the SSH lagging the index and lags in months. The 0.4 contours are shown to denote areas of significant correlation at the 90% confidence level based on a *t*-student distribution for the correlation coefficient. Correlations lower than 0.3 are not shown. Contours every 0.1 units.

IO are reinforced by the IOD- wind stress curl anomalies and grow in extension from 90°E to 60°E, with a strong SE-NW tilt. There are still positive correlations around Madagascar and from the southern tip of the island towards the African coast along the dipole corridor (de Ruijter et al., 2004). Negative correlations propagate between 5°-15°S as an upwelling Rossby wave (17 month time lag). They are strengthened and extend to the south near 75°E

Large-scale response of the SSH to the IOD

(21 month time lag), and at the longitude of the Mascarene's Arc they split into northward and southward branches, likely due to interaction with the bottom topography. They continue to extend southwestward along Madagascars eastern coast, until they form a large-scale pattern in the Mascarene Basin (25 month time lag). The shape of this pattern seems to result from the subsequent splitting of signals near 60E and at the islands eastern coast, as well as from interaction with signals arriving from the 20°S-band. Compared to the pattern at 13 months time lag, the negative correlations extend over a broader area to the east of Madagascar, and along the eastern side of the Mozambique Channel to the islands southern tip.

The 2-year correlation cycle described in Fig. 3.7 can be compared with a time longitude diagram of SSH anomalies along 14°S-15°S (Fig. 3.8). To examine the effect of the wind stress curl forcing on the SSH propagation, Fig. 3.9 shows the wind stress curl anomalies averaged in the band 10°-15°S. Negative SSH from the 1994 IOD+ enter the subtropical basin in early 1995 and can later be traced up to 95E (Fig. 3.8). It seems that the center of positive wind stress curl anomalies present around 90°-95°E has acted to weaken or destroy these anomalies (Fig. 3.9). During 1996 negative curl anomalies are present from 60°E to 95°E; in particular, anomalies in the west generate negative SSH, which continue to propagate west and finally in early 1997 form a (weak) negative SSH pattern east of North Madagascar. Positive SSH propagate from the central to the western IO from late 1997 through 1998 (Fig. 3.8), in response to the large-scale positive curl anomaly from the 1997 IOD+ (Fig. 3.9). Negative SSH entering the basin in early 1998 are reinforced around 95°E by negative wind curl anomalies associated with the 1998 IOD-. These SSH are further intensified near 80°-85°E by basin-scale negative curl anomalies (Fig. 3.8, Fig. 3.9), reaching an average SSH amplitude of 30 cm. They arrive at the coast of Madagascar in early 2000. At that time, a large-scale negative curl anomaly extends over the basin, which near 50°-60°E seems to amplify the large-scale negative SSH pattern that develops around the island. Negative curl anomalies near 80°E and 95°E force Rossby wave trains that reach Madagascar in late 2000 and 2001.

In conclusion, the propagation characteristics of the SSH from the 1997/1998 IOD event are consistent with the 2 year time scale found in the correlation analysis (Fig. 3.7). The SSH evolution after the 1994 IOD+ shows a gap in the propagating SSH signals between 85°-95°E, related to the absence of negative wind stress curl forcing (from an IOD-) in 1995. It is suggested though that negative SSH signals from the 1994 IOD- are connected to those finally regenerated in the western basin by the local wind forcing. The wind stress curl variability in the subtropical IO is not independent of ENSO (Reason et al., 2000). In particular, during the last decade wind stress curl anomalies between 10°S-15°S exhibit a significant correlation with the SOI (Chapter 2). Moreover, large negative wind stress curl anomalies near 90°-95°E in 1998, as well as those across the basin in early 1999 and 2000, are probably signals from the protracted 1998-2001 La Niña. These anomalies have a large impact on the Rossby wave activity arriving at Madagascar from late 1999 through 2001.

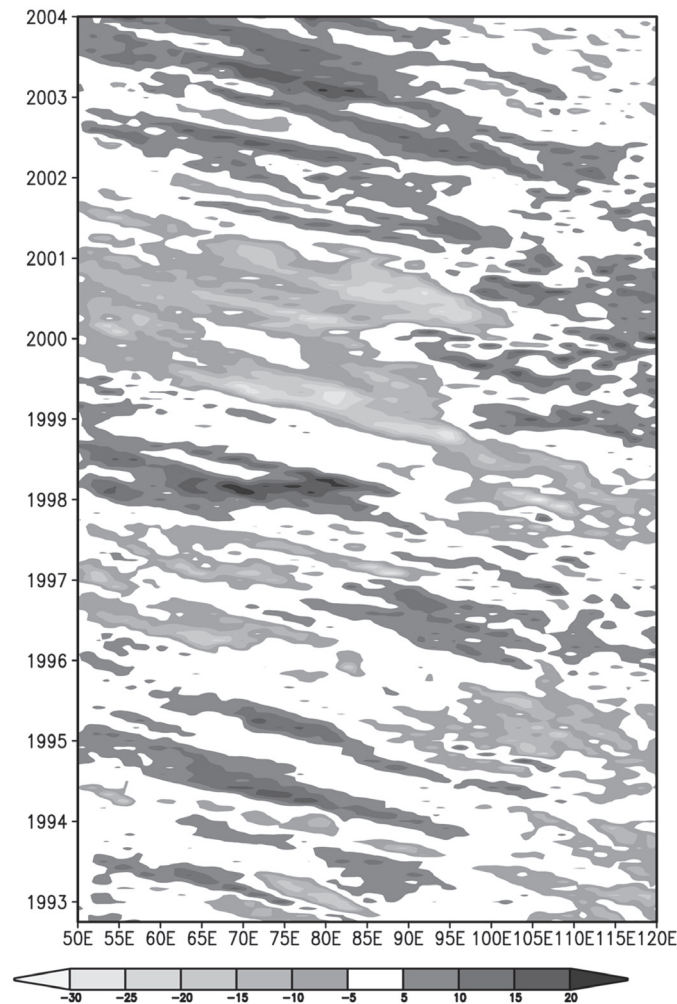


Figure 3.8: *Time-longitude diagram of the SSH anomalies averaged along the band 14°-15°S. Values lower than 5 cm are not shown. Units in cm.*

3.5 Linking the large-scale IO variability and the mesoscale activity around Madagascar

In this section we investigate a link between the mesoscale activity in the southwest IO (Section 3.3) and the basin scale variability (Section 3.4). The correlation patterns found to the east of Madagascar the year after the occurrence of a positive and negative IOD event (Fig. 3.7) suggest that local current regimes may be altered by these large scale SSH anomalies, with subsequent consequences for the formation of eddies in the area. In Section 3.5.1 we

Linking the large-scale IO variability and the mesoscale activity around Madagascar

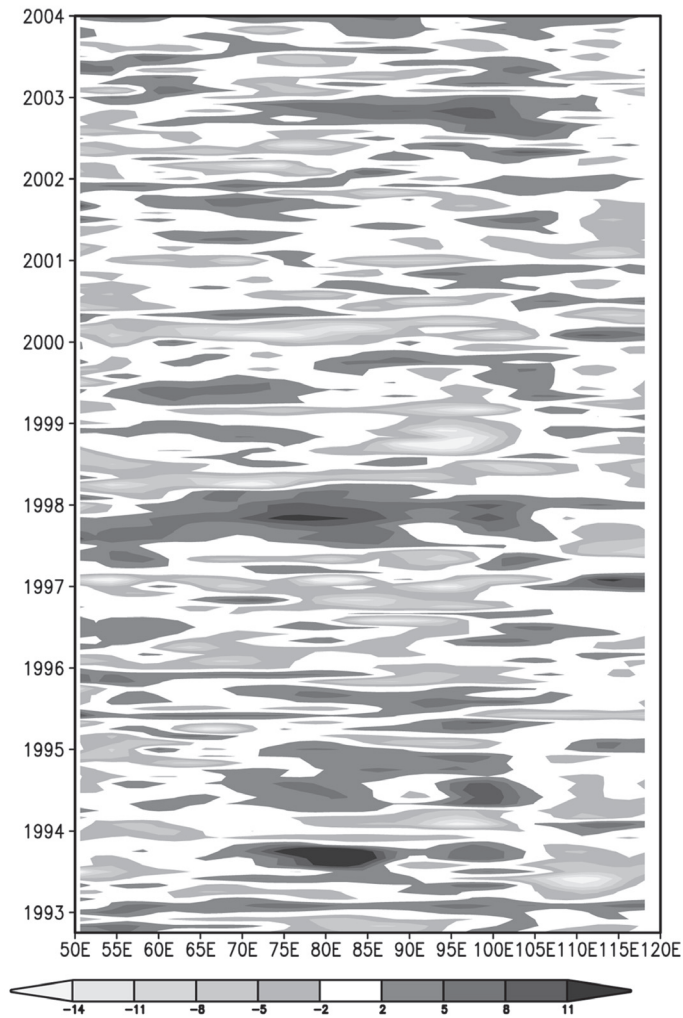


Figure 3.9: *Time-longitude diagram of the wind stress curl anomalies averaged in the band 10°-15° S. Units in $10^{-8} \text{ Pa m}^{-1}$.*

analyze changes in the western boundary currents around the island and relate them to variations in the intensity and lateral position of the tropical and subtropical gyres. The impact of the currents variability on the mesoscale eddy activity around Madagascar is discussed in Sections 3.5.2 and 3.5.3.

3.5.1 Variability of the local flow fields

To analyze variability in the SEC regime and its branches at the African and Madagascar coasts, SSH data along the tracks of the T/P and ERS satellites were used to derive surface geostrophic velocity anomalies. In total, six tracks are selected (see Fig.3.1). A track to the east of Madagascar intercepts the SEC at the core of its northern (11° - 13° S) and southern (17° - 20° S) branches. Tracks selected at the northern tip of Madagascar and at the eastern coast of Madagascar capture the westward flow of the NMC and the southward flowing EMC, respectively. The latter two sections extend 100 km and 60 km from the nearest point to the coast, which is consistent with the observations of Swallow et al. (1988) for the width of the NMC and EMC. Another two tracks intercept the western boundary flows at the narrows of the Mozambique Channel at 17° S and over the EACC path at 5° S. A track at the southern tip of Madagascar captures the EMC westward flow and its possible retroreflection path (EMCR). Note that to filter out mesoscale signals in the velocity anomalies, the time series are smoothed using three to five months running mean filters.

After the 1994 and 1997 IOD+ there is a decrease in the flow of both branches of the SEC (Fig. 3.10a) as well as in the NMC (Fig. 3.10b), the EMC (Fig. 3.10c) and the EACC (not shown). The situation reverses after the 1998 IOD- in early 1999, when an intensification of the SEC northern branch (Fig. 3.10a), the EMC (Fig. 3.10c) and the EACC is seen. These velocity anomalies are consistent with a weakening (strengthening) of the tropical gyre in response to positive (negative) large-scale SSH anomalies in the central western IO after the IOD phases (Fig. 3.7, lags =1 to 13 months). In early 1997 and 2000, there is an increase in the northern (only in 1997) and southern branch of the SEC, the NMC (Fig. 3.10a, b), and (only in 1997) the EMC (Fig. 3.10c). These anomalies suggest that negative SSH arriving at Madagascar 2 years after the peak of an IOD+ (Fig. 3.7, lags =25 months) could cause a strengthening and/or southward extension of the tropical gyre. Velocity anomalies in the narrows of the Mozambique Channel oscillate between -2 cm/s and 4 cm/s from 1997 to 2002, with increased flow in 1998 after the IOD+ and decreased flow during 1997 and in 2000-2001 (Fig. 3.10d). In the NMC, the tendency of increased flow persists during 2002-2003 (Fig.3.10b).

Analysis of the zonal geostrophic velocities from the gridded SSH data set for the SEC flow to the east of Madagascar also shows a net increase in the SEC from late 1996 to late 1997, followed by a decrease that lasted until 2000, and again a flow increase throughout 2000 and most of 2001 (Fig. 3.11). The variations in the flow of the NMC (also shown in Fig. 3.11) are closely related to the integrated flow of the SEC between 12° - 20° S, with a correlation of 0.75 between both series. Comparison with Fig. 3.10a indicates that while in 1997 and 1998 both SEC branches are involved in the strengthening and weakening of the SEC, the flow increase in 2000 is achieved by the southern branch.

To evaluate variations in the intensity and latitudinal position of the tropical and subtropical gyres, SSH anomalies from altimetry are combined with a mean dynamic topography of the IO (Rio and Hernandez, 2004). In Fig. 3.12 the variability of the absolute sea level from 1998 to 2000 is shown as composites of the SSH fields over the two seasons following the peak of the 1997 IOD+, the 1998 IOD-, and over 2000. Normally, the boundary between the IO tropical and subtropical gyres is found around 12° S (marked by the 2.03 contour). In the first half of 1998, Fig. 3.12a shows that the subtropical gyre extends up to 5° S, and the tropi-

Linking the large-scale IO variability and the mesoscale activity around Madagascar

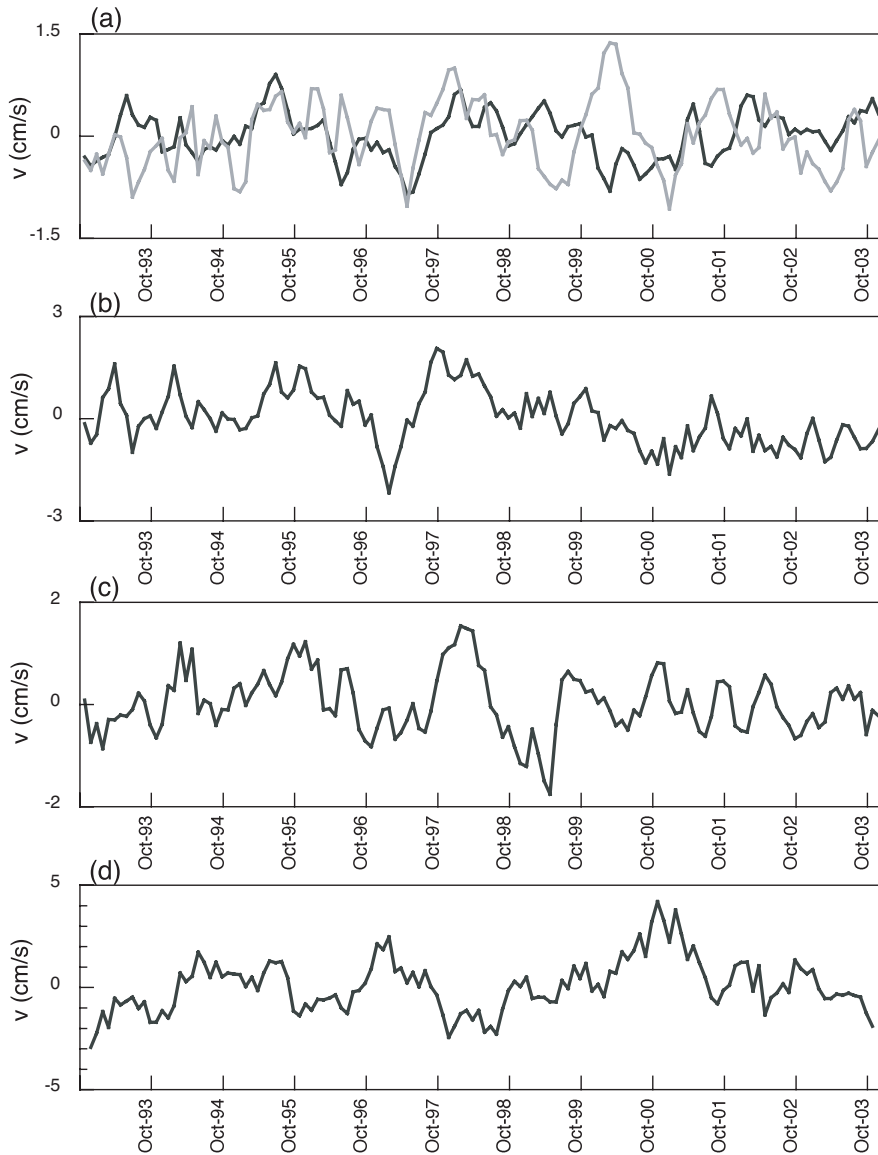


Figure 3.10: Time series of geostrophic velocity anomalies computed across the combined TP-ERS tracks that intercept the flow of the a) SEC northern branch (grey line) and SEC southern branch (black line), b) North Madagascar Current (NMC), c) East Madagascar Current (EMC), and d) the flow southwest of the narrows in the Mozambique Channel near 17°S. All the series were smoothed with a three month running mean filter, except in d), in which a five month running mean was applied. Positive velocity anomalies indicate less intense flow.

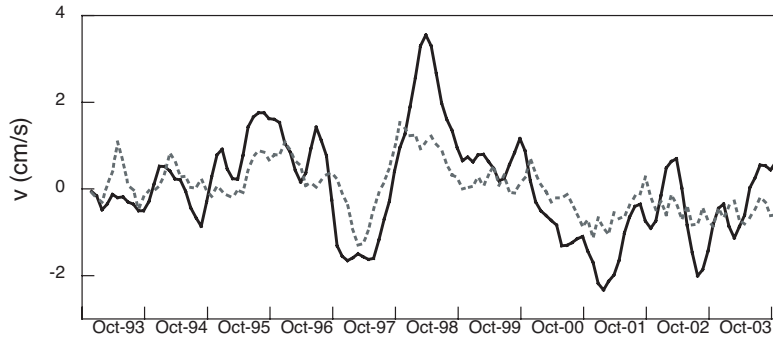


Figure 3.11: Time series of geostrophic zonal velocities computed from the gridded TP-ERS product and averaged over the SEC region 51° - 58° S, 12° - 20° S (solid line). Geostrophic velocity anomalies across the NMC track (Figure 3.10b) are also shown (dotted line). The time series were smoothed with a three month running mean filter. Positive velocity anomalies indicate less intense flow.

cal gyre was missing. On the other hand, the sea level pattern in 1999 displays an intensified tropical circulation extending northward from 15° S in the central IO with a SE-NW tilt (Fig. 3.12b). Eventually, in 2000 the limit of the tropical gyre is along 15° S, about 3 south of its normal position (Fig. 3.12c). After the 1994/1996 IOD cycle similar, but weaker, anomalies in the amplitude and extension of the tropical gyre are observed. Application of the island rule (Godfrey, 1989) indicates that a northward extension of the subtropical gyre to the east of the island or a reduction in the extension of the tropical gyre would induce a larger southward flow through the Channel, and vice versa. Liu et al. (1999) show a similar response of the island circulation to remotely forced long Rossby waves. In this sense, the variability of the flow through the Mozambique Channel seen from 1997 to 2001 (Fig. 3.10d) is in agreement with the large scale SSH anomalies arriving at the eastern Madagascar coast during those years (Fig. 3.8).

3.5.2 Impact on the Mozambique Channel eddy activity

The periods of high and low EKE in the central Mozambique Channel (Fig. 3.5a) coincide with years over which the flow in the narrows was relatively high and low, respectively (Fig. 3.10d). In addition, the EKE in the central Channel is correlated with large-scale SSH propagating from North(-east) Madagascar southward into the Channel. To analyze the relation between currents variability in the narrows and the eddy activity further south, we perform SSH composites during the high and low EKE periods.

Six out of 8 high EKE peaks in Fig. 3.5a are associated with propagating anticyclonic SSH anomalies. We average the SSH fields corresponding to 2 months before each of those EKE peaks. Similarly, for the low EKE period, we select 7 SSH fields associated with the small EKE peaks observed in the central Channel 2 months later. All the EKE peaks have similar characteristics with respect to the origin and propagation of the positive SSH anomalies traced through Channel, and this is well represented in the composites (Fig. 3.13). EKE

Linking the large-scale IO variability and the mesoscale activity around Madagascar

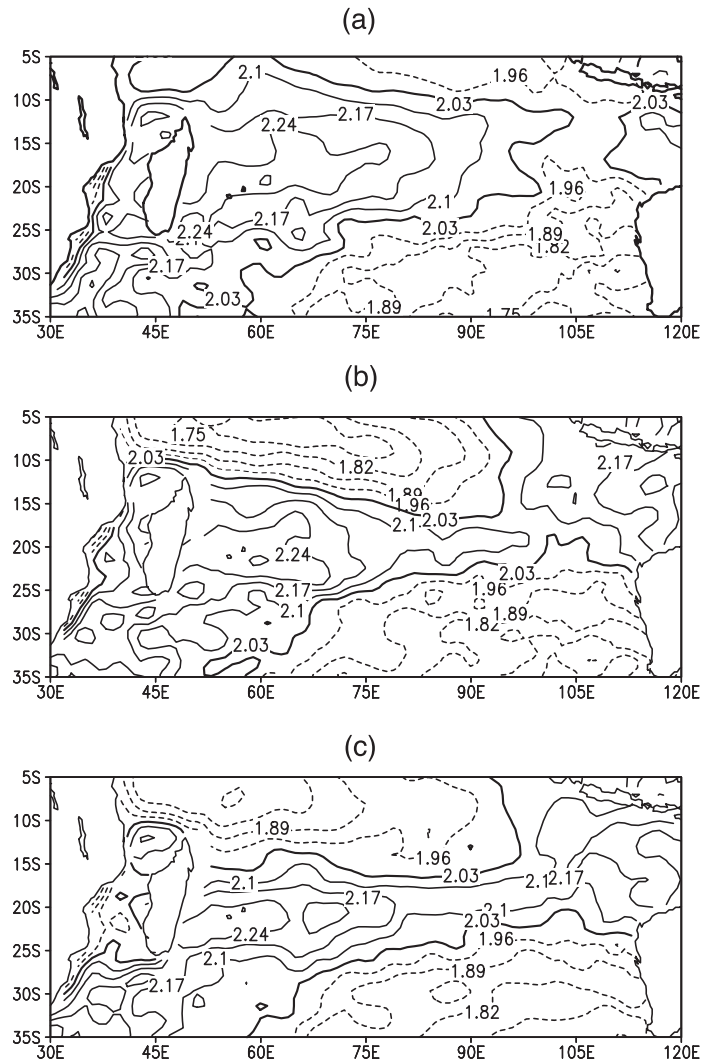


Figure 3.12: Total SSH field in the South Indian Ocean averaged a) from December 1997 to May 1998, b) from December 1998 to May 1999, and c) in 2000. SSH anomalies from altimetry were superimposed on a mean dynamic topography of the Indian Ocean (Rio and Hernandez, 2004) to derive the time-varying sea level. The 2.03 contour is thicker and denotes the limit between the tropical and subtropical gyres. After the 1997 IOD+ the subtropical gyre extends northward up to 5°S (Figure 3.11a). In contrast, after the 1998 IOD-, the tropical gyre intensifies and extends down to 15°S in the central Indian Ocean (Figure 3.11b). Eventually in 2000 the southern boundary of the tropical gyre is around 15°S (Figure 3.11c). Units in cm.

peaks left out from the composites did not show a clear relation with the flow in the western side of the Channel's narrows.

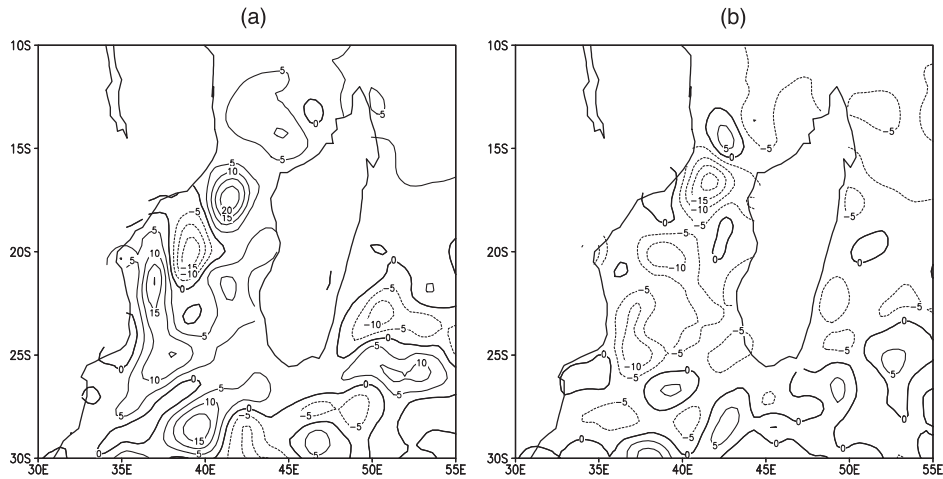


Figure 3.13: Composite of the SSH anomaly fields around Madagascar during (a) high EKE events and (b) low EKE events. For the high EKE composite six SSH fields that correspond to the EKE peaks that appear in the central Mozambique Channel (CC in Figure 3.2) in December 95, January 98, September 98, December 98, March 99 and May 99 are averaged. For the low EKE composite seven SSH fields that correspond to the weak EKE peaks observed in March 97, June 97, February 2000, June 2000, September 2000, December 2000 and March 2001 are considered. Units in cm.

During the high EKE period, an anticyclonic anomaly of 20 cm is present in the Channel's narrows, as well as large scale positive SSH in the northern Channel and east of North Madagascar (Fig. 3.13a). The larger velocities in the narrows could favor the growing of passing anticyclonic anomalies. In the Mozambique Channel between 20°-24°S a large anticyclonic anomaly is also present. Schouten et al. (2003) proposed that eddies in the central Channel grow due to merging with other elongated positive SSH anomalies that approach from the eastern side. Altimetry data indicate that all the anticyclonic anomalies over the period 1996 and 1998-1999 experienced merging at some stage of their propagation. In particular, an elongated anomaly was observed to move off the western Madagascar coast in January 1999 and interact with an eddy south of the narrows in March 1999.

During the period of low EKE no anticyclonic anomalies are seen in the Channel (Fig. 3.13b). Negative SSH arrive from the Indian Ocean at the northern Madagascar coast and only a weak positive SSH is present around 14°S (Fig. 3.13b). Examples of these are anticyclonic SSH observed in the northern Channel in February 2000, September 2000 and January 2001, which probably correspond to eddies measured hydrographically by Ridderinkhof and de Ruijter (2003) in April 2000, September 2000 and February 2001, respectively. After passing the narrows, altimetry shows that these anomalies were considerably reduced in size. It seems that weaker currents in the narrows and the absence of positive SSH inhibit the growth of eddies and/or induce a destructive merging between the SSH. In particular, the anticyclonic anomalies seen in the narrows in April 2000 and September 2000 became weaker and got squeezed towards the African coast after large elongated negative SSH from the eastern side appear in the central Channel in July 2000 and December 2000.

3.5.3 Connection to the eddy activity south of Madagascar

In the South Madagascar region no unique relationship between the EKE and the EMC variability could be established from these data. The EKE minimum observed from 1998 to 1999 (Fig. 3.5b) could be a lagged response to the weakening of the EMC in 1998 (Fig. 3.10c). However, the EKE peaks during 1996-1997 and 2000-onwards lack periods of a more intense EMC. The predominance of positive SSH from 1998 to mid-1999 around the southern tip of Madagascar (Fig. 3.3c) suggests a decrease in the cyclonic activity from the EMC. On the other hand, negative SSH propagating along 20°S after the IOD+ and arriving at the eastern Madagascar coast during the period 1999-2001 (Fig. 3.3b), could be favorable for the formation of dipoles southeast of the island (de Ruijter et al., 2004). It is likely then that the EKE in this region is not only influenced by tropical variability, but also from that of the subtropical band 20° - 30°S as well as midlatitude variability.

In association with the period 1999-2000 when a stronger and southward-extended tropical gyre was seen, anomalies in the surface currents to the south of Madagascar also appeared. Fig. 3.14 shows that the EMC and the flow to its south, i.e. the EMCR, display an anti-phase relation over most of the years. This tendency was interrupted during 1999-2000, and in 2000 a stronger westward jet south of Madagascar is seen. The extra transport towards the African coast could have been carried by the dipoles that later join the Agulhas retroflection regime (de Ruijter et al., 2004). Different than other years, this train of dipoles propagated almost straight towards the AC.

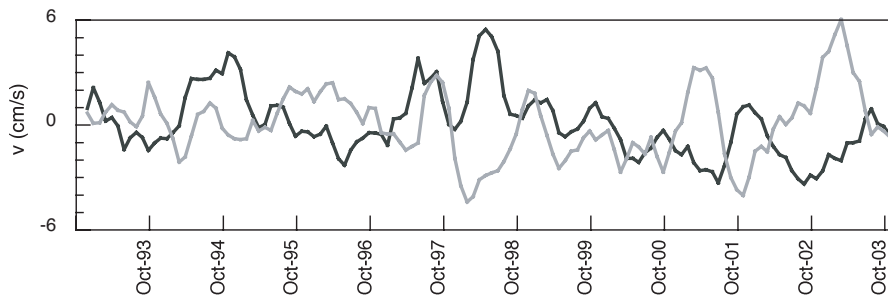


Figure 3.14: Same as Figure 3.10, but for the flow at the southern tip of Madagascar along the EMC westward path (black line) and the flow along the possible EMC retroflection path (EMCR) (grey line). In the former negative anomalies mean more intense westward flow; in the latter negative anomalies mean less intense eastward flow. Both time series were smoothed with a five month running mean filter.

3.6 Summary and discussion

We have used sea level data from T/P and ERS satellites for the period 1993-2003 to study the interannual variability of the SSH and EKE fields in the Mozambique Channel and South Madagascar regions. In particular, the goal of this study was to investigate a possible link

between the mesoscale eddy field in these two regions and the large-scale Indian Ocean (IO) variability via changes in the western IO upper layer currents. Large-scale SSH signals related to the occurrence of the IOD cycle in the Tropical IO propagate in the subtropical IO as forced Rossby waves that arrive at the coast of Madagascar about 1 year after each IOD phase (Fig. 3.7). By computing geostrophic velocity anomalies from altimetry, we found that sea level anomalies due to a positive IOD event induce a weakening in the surface flow of the South Equatorial Current (SEC) west of the Mascarenes Arc and its branches at the Madagascar and African coasts. In contrast, the response to a negative IOD event is an intensification of these currents. As a consequence, an intensification and northward (southward) extension of the subtropical (tropical) gyre is seen after the positive (negative) IOD phase (Fig. 3.12), leading to anomalies in the flow through the Mozambique Channel consistent with the Island Rule predictions (Godfrey, 1989).

The SSH field in the northern and central Mozambique Channel shows significant inter-annual variability; especially after the 1997/1998 IOD when a 2 year period of positive SSH anomalies was followed by a 2 year period of negative SSH anomalies. This variability is also related to the ENSO events that coincided with the IOD phases over last decade. In response to large-scale SSH and circulation anomalies, the mesoscale eddy activity in the central Mozambique Channel shows periods of high (low) EKE after a positive (negative) IOD event. This EKE interannual modulation is not apparent in the EKE of the northern Channel. The difference can be explained in part by interaction between the currents in the narrows and eddies coming from the north. After a positive IOD event, relatively strong surface currents tend to reinforce the amplitude of passing eddies. Additionally, a predominance of positive SSH stimulates merging between anomalies in the central Channel, favoring further growth. Therefore periods of high EKE coincide with high amplitude eddies that are ultimately responsible for a larger southward transport through the Channel. The opposite is expected after the negative IOD phase.

The formation of eddies north of the Mozambique Channel is characterized by a 7 times/year frequency induced by barotropic instability of the SEC (Quadfasel and Swallow, 1986). Schouten et al. (2003) showed that further south, this frequency is reduced to 4-5 times/year. They also observed reduced eddy formation in the first half of 1998. We suggest that the northward shift of the subtropical gyre during that period caused a reduction of the instability of the SEC-jet north of Madagascar, which lead to less eddies being formed that year. This study also shows that 2 years after the IOD positive phase the EKE associated with 4-5 times/year eddies in the central Channel is greatly reduced. These changes could be traced until the southern part of the Channel around 24S; in particular a break in the EKE signal occurred from August 2000 until November 2001. This extreme response in the Mozambique Channel eddy activity is influenced by anomalous wind stress curl forcing due to the protracted 1998-2001 La Niña. Large-scale negative wind stress curl anomalies appear to the east of Madagascar during the second and third year of a protracted event (Chapter 2) that may induce an anomalous cyclonic circulation there, and thus a reduction in the Channels throughflow. During 1999 negative wind stress curl anomalies in the central basin were responsible for the forcing of upwelling Rossby waves, and in 2000, at the arrival of those waves, local curl anomalies helped the development of a large negative SSH pattern around the island. The occurrence of the IOD negative phase in 1996 without ENSO that year seems to explain the lesser impact on the Channels eddy activity seen in early 1997.

Summary and discussion

The EKE in the region south of Madagascar shows a period of low eddy activity after the 1997 IOD, when the EMC was weaker. Otherwise, we could not find a relation between anomalies in the EMC and the EKE to the southwest from altimetry data. Variations in the dipole activity south of Madagascar have an impact on the Agulhas Current (AC) further south. The interaction between the train of dipoles in 2000 and the AC led to an eastward shift of the Agulhas retroflexion that lasted for about 6 months (de Ruijter et al., 2004). They also showed that the dipoles that year propagate to the AC following a southwestward path. Altimetry data show anomalies in the currents south of Madagascar consistent with a stronger flow towards the AC. In addition, due to the reduction in the eddy activity of the Mozambique Channel in 2000 it is possible that interactions between SSH anomalies in the southern part of the Channel was inhibited and the dipoles could propagate straight to the AC.

The Indonesian Throughflow (ITF) entering the basin between 10° - 15° S is another cause of interannual variability in the IO. Anomalous winds around Indonesia during the ENSO/IOD alter the normal Indo-Pacific sea level gradient, which is the driving force of the ITF: during El Nio (La Nia) events, a lower (higher) ITF transport is expected, and vice versa for the IOD phases (Meyers, 1996). Murtugudde et al. (1998) verified this with a simple model, and found a large increase in the ITF during the 1994 IOD event. Ultimately, it is the wind curl in the central IO that modulates the SSH variability arriving to the east of Madagascar (Matsumoto and Meyers, 1998).

Understanding the year-to-year variations in the flows around Madagascar is relevant for both the local and global circulation dynamics and variability. Schouten et al. (2002a) showed that eddies from the Mozambique Channel and South Madagascar are a control on the shedding of Agulhas Rings south of Africa, and therefore have an impact on the Indian-Atlantic interocean exchange. We found that large-scale SSH anomalies related to the IOD induce changes in the surface currents in the western IO that subsequently alter the EKE in the central Channel and eventually the southward throughflow. Although a lag of about 1.5 years is detected between an IOD peak and the EKE interannual variability in the central Channel, the analysis is limited by the length of the available time series and the conclusions depend on only a few IOD events. It is therefore necessary to continue monitoring the SSH interannual variations in the subtropical IO and around Madagascar.

Chapter 4

Flow structure and variability in the Subtropical Indian Ocean

4.1 Introduction

It is well known from satellite altimetry that the variability of the South Indian Ocean comprises a range of frequencies from interannual to subannual time scales (e.g., de Ruijter et al., 2005). The rms of the sea surface height (SSH) in the South Indian Ocean shows a local maximum off Sumatra extending into the basin along 12°S , and a second area of high variability around 25°S extending eastward to the Australian coast and westward to the east of Madagascar (see Fig. 1.6). The SSH variance from off Java to 90°E is related to baroclinic instability of the South Equatorial Current (SEC) at a period of 40-80 days (Feng and Wiffels, 2002), while to the west the variance is attributed to annual Rossby waves (Perigaud and Delecluse, 1992; Morrow and Birol, 1998), as well as interannual SSH anomalies related to the Indian Ocean dipole (IOD) and ENSO teleconnections (Xie et al., 2002). In the latitude band 20° - 30°S evidence for semiannual (Morrow and Birol, 1998) and 4-5 times/year (Schouten et al. 2002) westward propagating Rossby waves was found. Analyzing a simple two-layer model, Birol and Morrow (2001) concluded that the quasi-semiannual Rossby waves (i.e. periods between 150-180 days) are connected to variations in the eastern boundary pycnocline. Moreover, Birol and Morrow (2003) presumed that the semiannual coastal Kelvin waves along Australia might be remotely forced, i.e. by equatorial Pacific wind anomalies. However, the forcing of the observed 4-5 times/year waves in the 25°S band east of Madagascar was not identified. In the present study, we further investigate the causes of the variability in this subtropical band.

The eastern part of the subtropical Indian Ocean is also characterized by significant mesoscale eddy activity associated with eddies pinched off from the Leeuwin Current west off Australia. Combining hydrographic observations and altimetry data, Fang and Morrow (2003) could track Leeuwin Current anticyclonic eddies propagating westward between 20° - 32°S . Interaction with bottom topography seems to induce a slowing down and decay of the eddy amplitudes. Overall, the eddy signals are lost west of 90°E .

South of Madagascar eddies have been tracked with altimetry propagating (south) westward towards the Agulhas Current (Gründligh, 1995; Schouten et al., 2002). Thereafter, they may have an impact on the shedding of Agulhas rings (Schouten et al., 2002). Recently, large deep-reaching dipoles (i.e. vortex pairs) were discovered and measured hydrographically in this region (de Ruijter et al., 2004). They also propagate into the Agulhas Retroflexion region and trigger the shedding of Agulhas rings. Analyzing 6 years of altimetry data, de Ruijter et al. (2004) could only follow three of these dipoles upstream as pairs to the southern tip of the Mascarene ridge (23°S, 55°E); in most cases, cyclonic vortices formed as lee eddies at the southern tip of Madagascar, whereas anticyclones were first observed in the region east or south of Madagascar. Schouten et al. (2002) detected a dominant frequency of 4-5 times/year in the eddy variability of the Mozambique Channel and south of Madagascar and suggested a modulation in the eddy-formation processes by the arrival of Rossby waves at 12°S and 27°S at the same subannual frequency. In addition, the eddy kinetic energy in the Mozambique Channel shows significant interannual variability associated with signals from the IOD propagating between 10°-15°S (Palastanga et al., 2006).

Baroclinic instability processes appear to be important in explaining the observed eddy variability in subtropical ocean basins (Gill et al., 1974; Qiu, 1999; Qiu and Chen, 2004). Stammer (1997) pointed out that this might be a general characteristic of the extratropical oceans: the analysis of global SSH wavenumber spectra showed that at midlatitudes maximum energy is found at a wavelength related to the first mode baroclinic Rossby radius of deformation, suggesting the dominance of baroclinic instability as a source for mesoscale variability. In the center of the subtropical gyres of the Pacific Ocean, eastward quasi-zonal currents of thermal origin have been documented (Qiu and Chen, 2004), and were simulated with numerical models (Takeuchi, 1986). Using a $2\frac{1}{2}$ -layer model, Qiu (1999) and Qiu and Chen (2004) studied the baroclinic instability of these quasi-zonal jets in the North and South Pacific, respectively. Their findings suggest that seasonal variations in the intensity of the instability can explain the seasonal variations observed in the eddy kinetic energy. The question that arises is to what degree the variability in the subtropical band east of Madagascar can be explained in a similar way.

The first objective of this study is to describe and analyze the mean circulation of the subtropical Indian Ocean between 20°-30°S, in particular, its vertical structure and velocity shear characteristics. The second objective is to investigate the stability characteristics of this flow. So far, the scarcity of observations in the central part of the subtropical gyre of the South Indian Ocean has limited a detailed analysis of the currents and their variability. In this study we combine the available hydrographic data with altimetry observations to investigate the structure of the flow and show a connection between the subtropical South Indian Ocean upper layer circulation and the local eddy-field. The Chapter is organized as follows. In Section 4.2 the data sets used in this study are described and Section 4.3 briefly discusses the characteristics of the subtropical eddy variability derived from altimetry. Section 4.4 deals with the description of the mean flow structure along the 20°-30°S band. The instability of this flow is analyzed in Section 4.5 using 2-layer model dynamics. A summary and discussion close the Chapter.

4.2 Data

The climatological data used in this study consists of temperature and salinity observations of the South Indian Ocean available in the World Ocean Atlas 2001 (WOA01) database (Conkright et al., 2002). These observations were objectively analyzed and interpolated onto a 1-degree resolution grid extending from the surface to a depth of 5500 m. The sampling in the subtropical South Indian Ocean, especially far from the coast, is rather poor. The number of surface temperature observations along 25°S within 1-degree boxes lies on average between 20 and 60, in particular observations decrease from 60 near 65°E to about 15 near 90°E. The number of surface salinity observations is larger in the western than in the central South Indian Ocean basin, with most of the observations confined to meridional sections located along 65°E, 80°E and 90°E (i.e. on average 10 to 15 observations are found along 25°S).

Additional temperature and salinity data were obtained from three WOCE hydrographic sections in the Indian Ocean. These comprise the IO7N and IO7C sections along 55°E from 12°S to 29°S (Donahue and Toole, 2003); the I8N section along 80°E, from 24°S to 6°N (Talley and Baringer, 1997); and the I9N section along 95°E from 45°S to 5°S (Gordon, 1995).

We use SSH measurements from the TOPEX/Poseidon (T/P) and ERS satellite missions combined and interpolated onto a $1/3^\circ \times 1/3^\circ$ grid by the CLS Space Oceanography Division, France. These data span the period October 1992-January 2004, with a time spacing of one week.

4.3 SSH variability from altimetry

To highlight mesoscale eddy variability in the altimetry data a high pass Lanczos filter (Duchon, 1979) with a 35 weeks (~ 8 months) cutoff period was applied to the weekly SSH. As the filter response function varies from 1 to 0 at periods from 18 to 35 weeks, by filtering we expect to remove the steric height annual variability (~ 52 weeks) (Stammer, 1997) and to reduce the semiannual signal (~ 25 weeks) observed along the latitude band 20°-30°S (Morrow and Birol, 1998). The rms of the high passed SSH shows a band of high variability around 25°S like the unfiltered data (see Fig. 1.6), but with relative maxima more clearly outstanding near 67°E, 80°E, 87°E, and 105°E (Fig. 4.1). Inspection of the time-longitude diagram of the high passed SSH reveals wavelike westward propagating features along this band (not shown).

To analyze the dominant frequencies of the SSH variability along 25°S, a spectral analysis was performed around 100°E, 80°E, and 65°E. Figure 4.2a shows that near 100°E the dominant variability is found at around frequencies of 0.052 weeks^{-1} (~ 2.5 times/year), while in the central and western basin spectral peaks occurs at around $0.067\text{-}0.072 \text{ weeks}^{-1}$ (~ 4 times/year). In particular, the latter frequency appears to dominate the spectra over the areas of maximum variability west of 90°E (Fig.4.1). The presence of variability around 4 times/year is consistent with the observations of Schouten et al. (2002). Energy present at periods of 22-24 weeks is probably related to the quasi-semiannual variability forced at the eastern boundary (Birol and Morrow, 2001).

Flow structure and variability in the Subtropical Indian Ocean

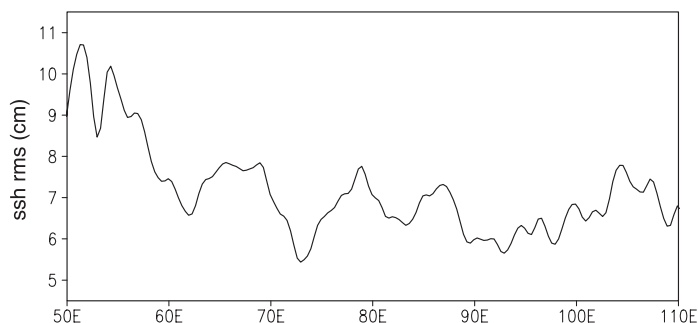


Figure 4.1: *Rms of the high pass filtered SSH along 24°S in the South Indian Ocean. A filter with a cutoff period of 8 months was applied to the weekly SSH field from the combined T/P-ERS data set.*

To estimate the spatial scales associated with the subtropical eddy variability, wavenumber-spectra of the high pass filtered SSH with a cut off wavelength of 700 km were computed along 25°S and between 50°E-110°E. The average spectrum shows a dominant peak at a wavelength of around 440 km, whereas for higher wavenumbers the energy closely follows a k^{-3} relation (Fig. 4.2b). Stammer (1997) noted that this type of cutoff in the spectra is associated with the length scale at which the maximum baroclinic instability occurs. Moreover, the energy decay in the spectra as a power-function of the wavenumber k is consistent with theories of baroclinic instability and geostrophic turbulence (Pedlosky, 1987). In the South Indian Ocean around 25°S the wavelength associated with the first baroclinic Rossby radius of deformation is $2\pi R_0 \sim 330 \text{ km}$ (Chelton et al., 1998). This is in good agreement with the SSH spectral maximum, if one considers that real mesoscale features tend to be larger than those predicted by linear theories of baroclinic instability (Pedlosky, 1987). The peak in the spectra at a wavelength of around 590 km (Fig. 4.2b) might be related to the quasi-semiannual waves, i.e. wavelengths between 300-500 km, observed by Morrow and Birol (1998).

4.4 Mean flow structure

Due to the scarcity of observations in the center of the subtropical gyre, the flow structure between 20°-30°S is not yet well known. Based on hydrographic data, Stramma and Lutjeharms (1997) estimated the transport of the subtropical gyre over the upper 1000 m. They showed that the westward return flow in the gyre is found in the subtropical basin from 40°S up to the latitude of the SEC, and as part of a recirculation cell in the southwest corner of the basin (see their Fig. 7). Dynamic topography maps in the atlas by Wyrski (1971), as well as a more recent analysis by Reid (2003), indicate however, a surface eastward flow to the east of Madagascar. In this section we analyze in detail the structure of the flow in the South Indian Ocean around 25°S from the surface down to about 1000 m. Although it is expected that seasonal changes can be important in the near surface circulation, because of the lack of observations, we limit the description to the mean pattern. Comments related to the seasonal variability are included in the discussion section.

Mean flow structure

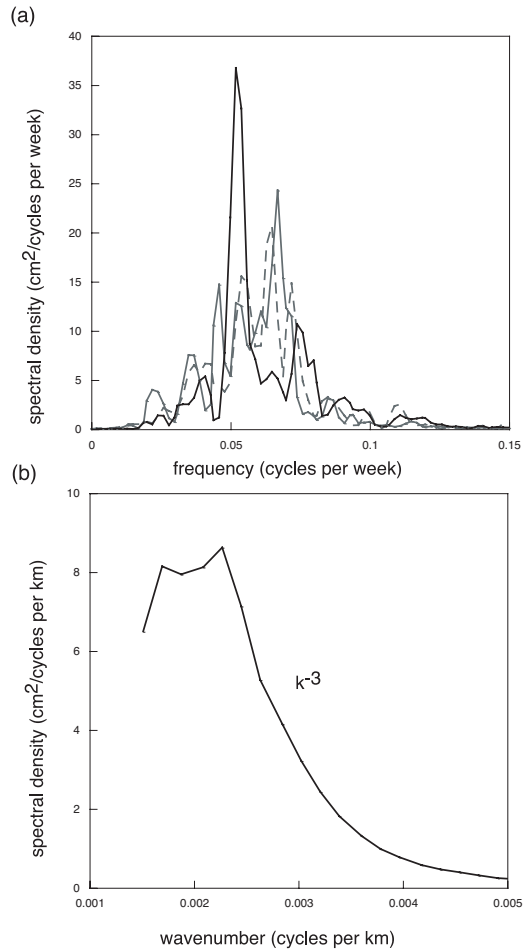


Figure 4.2: (a) Frequency spectra of the high pass filtered SSH from the combined TIP-ERS data set in three regions along 25°S, namely, at 100°E (solid black line), 80°E (dashed line), and 65°E (solid gray line). The dominant frequency changes from 2.5 times/year in the east to 4 times/year in the central and western basin. (b) Wavenumber spectra of the SSH data along 25°S and between 50°-110°E. Weekly SSH were high pass filtered with a cut off wavelength of 700 km. Energy decays at high wavenumbers as the third power law of the wavenumber, k^{-3} . The dominant wavelength is found around 440 km, and a second peak appears around 590 km.

The climatological dynamic topography at the surface relative to 2000 m (Fig. 4.3a) shows the pattern of the subtropical gyre with a recirculation cell in the southwestern basin around 30°S (Stramma and Lutjeharms, 1997) and an anticyclonic recirculation to the east of Madagascar. The latter is bounded to the north by the westward flowing SEC, roughly between 10°-20°S, and to the south by an eastward flow from south Madagascar up to 75°. The eastward flow continues between 20°-30°S from the central basin to Australia, and seems

Flow structure and variability in the Subtropical Indian Ocean

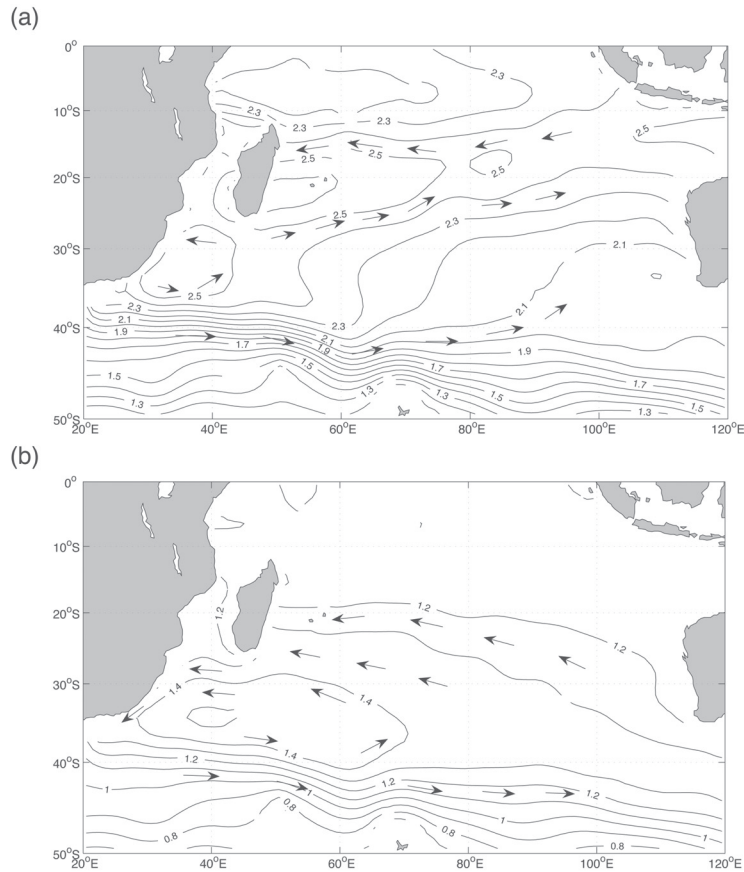


Figure 4.3: *Dynamic topography of the South Indian Ocean relative to 2000 m at (a) the surface and (b) 500 m, based on the climatological hydrographic data. Units in $m^2 s^{-2}$. Contours every 0.1 units. It shows a recirculation cell east of Madagascar and general eastward flow in the upper layer south of 20°S. At 500 m the flow between 20°S and 30°S is westward, as an Sverdrupian flow.*

connected to the South Indian Ocean Current, which constitutes the southern limit of the subtropical gyre at around $\sim 40^\circ S$ (Stramma, 1992). This shallow, quasizonal eastward flow along $25^\circ S$ has not been previously documented in detail. It is noteworthy that the location of this jet is similar to that of the subtropical countercurrents observed in the North and South Pacific (Qiu, 1999; Qiu and Chen, 2004), supporting the idea of a dynamically similar permanent current in the South Indian Ocean subtropical gyre. By analogy with the Pacific Ocean we will hereafter refer to the Indian Ocean eastward jet as the South Indian Ocean Countercurrent (SICC). At 500 m (Fig. 4.3b), the flow between 20° - $30^\circ S$ is westward in agreement with the large scale Sverdrup flow forced by the wind stress curl, while in the southwest the recirculation cell extends up to $70^\circ E$.

A geostrophic velocity section at $65^\circ E$ based on climatology (Fig. 4.4a), shows the verti-

Mean flow structure

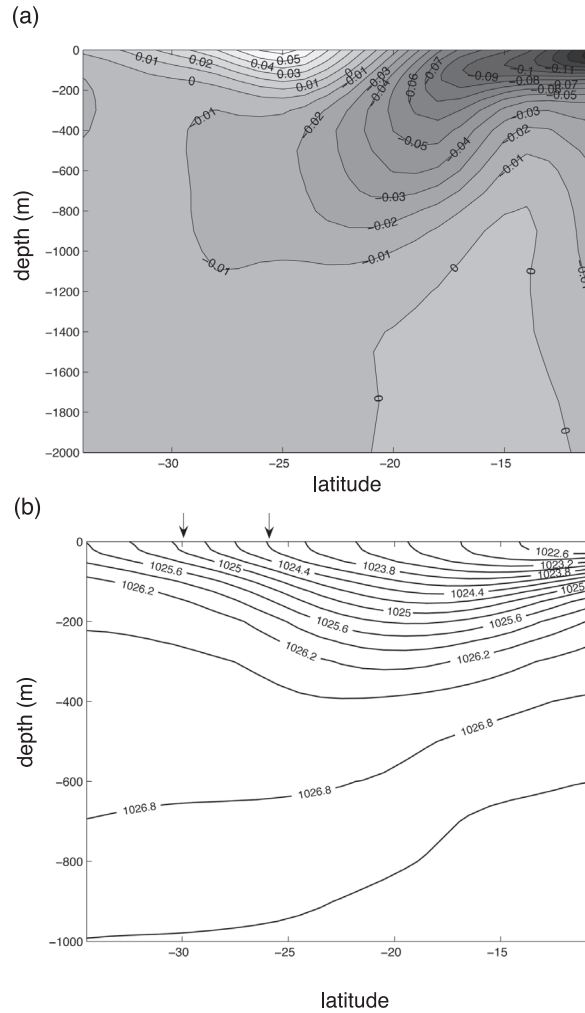


Figure 4.4: Geostrophic zonal flow structure along 65°E computed from climatological temperature and salinity data relative to 2000 m. Contours every 0.01 m/s. Light (dark) shaded correspond to the eastward SICC (westward SEC). The SICC extends in the latitude band 20°-35°S, overlying the southward extension of the SEC at deep levels in the subtropical gyre. (b) Meridional section of potential density along 65°E in the South Indian Ocean from the climatology. Units in kg m^{-3} . Contours every 0.3 units. A shallow density front exists in the latitude band 26°-30°S. This front lies farther north than the northern branch of the Subtropical Front (i.e., NSTF) documented by Belkin and Gordon (1996).

cal structure of the flow east of Madagascar. The eastward jet is confined to the upper 250 m in the latitude band 20°-35°S, with its core around 25°S and surface velocities up to 0.06 m/s. It flows above westward velocities of about -0.02 m/s associated with the southward extension of the SEC between depths of 350-1100 m. This vertical structure characterizes the flow

Flow structure and variability in the Subtropical Indian Ocean

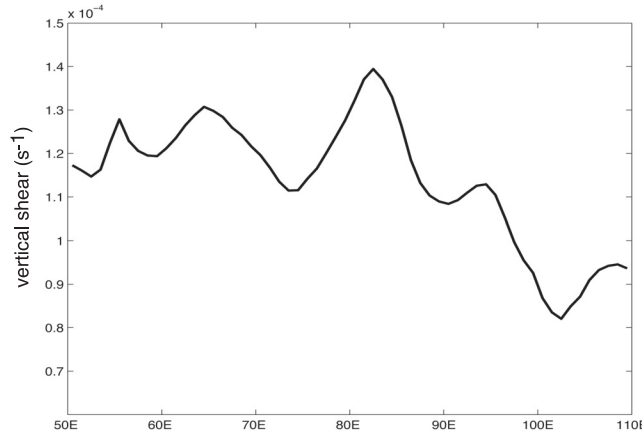


Figure 4.5: Vertical shear of the (climatological) SICC-SEC system along 25°S in the South Indian Ocean. The shear is computed as the difference between velocities at the surface and at 600 m, divided by the layer depth. Relative maxima are found near 55°E, 65°E and 82°E, although the variations are small.

between 50°-95°E, with the core of the eastward jet slightly to the north east of 75°E. A density section at the same location (Fig. 4.4b) shows a relative high meridional gradient of the surface isopycnals between 26°-30°S, suggesting the presence of a frontal structure in the upper 200-300 m. The SICC could be the current associated with the front in terms of thermal wind balance. An estimate of the velocity difference between the climatological flow at the surface and at a depth of 600 m yields relative maxima of ~0.08 m/s near 55°E, 65°E and 83°E, and minima near 75°E and 90°E (Fig.4.5), which are mainly related to the intensity of the climatological surface current.

To estimate the actual strength of this frontal system geostrophic velocities were also derived along three WOCE hydrographic sections. Along 55°E the velocity section shows two alternating eastward and westward velocity cores between 22°-26°S, extending from the surface to about 900 m deep, which seem to be due to two anticyclonic eddies (not shown). Additionally, LADCP data available at the time of the cruise confirm the eastward-westward reversal of surface velocities around 25°S, with speeds of 0.35 m/s. In the section along 95°E there is also an indication of an anticyclonic eddy around 24°S. Because of the presence of eddies, these two sections were not considered for further analysis. The section along 80°E extended to the south as far as 24°S. Between 22°-24°S a core of eastward velocities is seen in the upper 200 m, flowing over a westward flow. Velocities at the surface reach 0.28 m/s and show a minimum of about 0.025 m/s near 500 m (Fig.4.6a). Comparison with the vertical structure obtained from the climatology at that location indicates good qualitative agreement, although there are differences in the depth extension of the eastward and westward flows, and in the magnitude of the surface velocities. In particular, the actual surface velocities are almost one order of magnitude larger than the climatological ones, and the difference between surface and 600 m velocities is greater in the synoptic data by a factor of 4 (Fig. 4.6a,b).

The subtropical countercurrents in the Pacific Ocean are closely related to the location

Mean flow structure

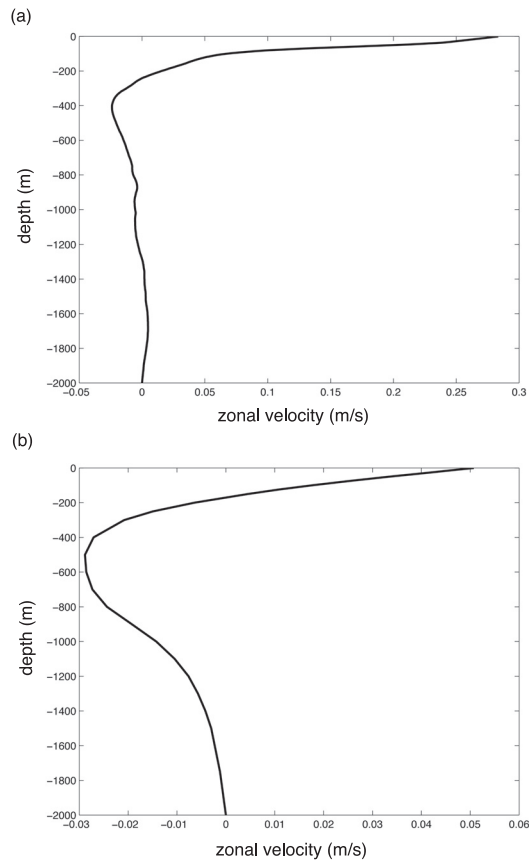


Figure 4.6: (a) Geostrophic zonal velocity profile at 80°E , 24°S , in the upper 2000 m from a WOCE hydrographic section. (b) Same as Figure 4.6a, but from climatological data. Note the difference in velocity scale. It shows that climatology underestimates significantly the magnitude of the surface, eastward velocities. The velocity difference computed between the surface and 600 m is about 0.3 m/s in the WOCE data, and lower by a factor 4 in climatology (~ 0.08 m/s).

of the Subtropical Front. They originate from the superposition of the baroclinic circulation driven by the meridional temperature gradient across the front, and the wind driven barotropic flow (Takeuchi, 1986). Belkin and Gordon (1996) analyzed the fronts of the South Indian Ocean south of 30°S . They defined the northern branch of the Subtropical Front (NSTF) over the sector $30^{\circ}\text{-}38^{\circ}\text{S}$, $60^{\circ}\text{-}90^{\circ}\text{E}$ to be the southern boundary of the warm, salty water of the central subtropical gyre. Inspection of the mean sea surface temperature (SST) fields from climatology shows a band of relatively high meridional SST gradients extending with a south-eastward tilt from 45°E , 27°S towards Australia (Fig. 4.7a). Analysis of SST from satellite data supports the existence of a similar basin temperature front between $27^{\circ}\text{-}35^{\circ}\text{S}$. In the central basin, these temperature gradients seem connected to the NSTF of Belkin and Gordon (1996). The meridional salinity gradients from climatology indicate a frontal zone east of

Flow structure and variability in the Subtropical Indian Ocean

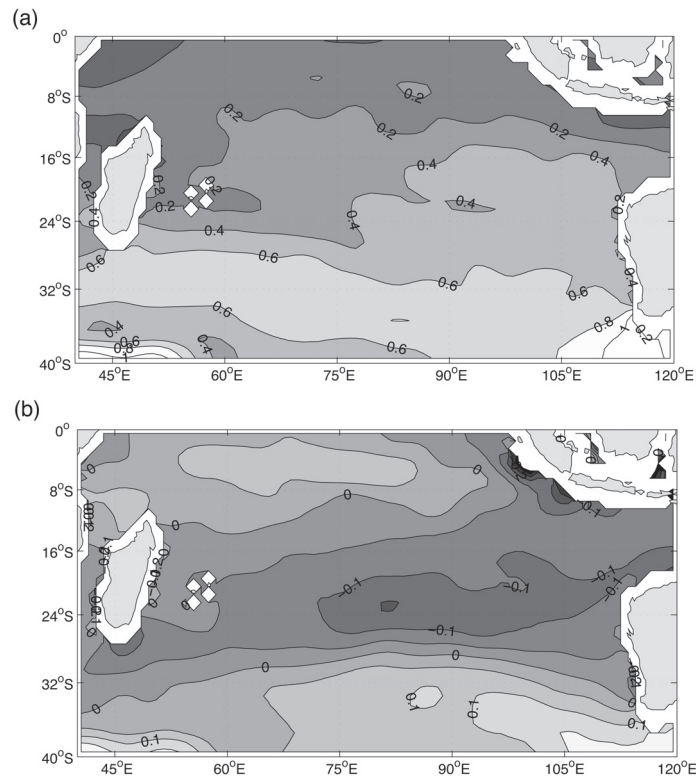


Figure 4.7: (a) Meridional sea surface temperature (SST) gradients in the South Indian Ocean. Units in $^{\circ}\text{C}/\text{m}$. (b) Same as Figure 4.7a, but for salinity. Units in psu/m . Climatological temperature and salinity data are used. A subtropical temperature frontal zone extends southeastward from south Madagascar at 27°S towards southwest Australia. The salinity front seen around 24°S and east of 75°E corresponds to the South Indian Tropical Front (Tchernia, 1980).

75°E between 20° - 26°S (Fig.4.7b), that corresponds to the South Indian Tropical Front (Tchernia, 1980), which separates salty waters of the central subtropical Indian Ocean from the fresher waters of the eastern tropical Indian Ocean. As a consequence, a secondary density front exists in the band 20° - 30°S (i.e. north of the NSTF of Belkin and Gordon (1996)) extending with a northeastward tilt from southeast Madagascar to the eastern subtropical basin. Whether (and how) this subtropical frontal zone is linked to the origin of the SICC deserves further investigation that will be left for future studies.

Another important aspect of the SICC to be investigated is its connection to the western boundary current that closes the surface anticyclonic circulation east of Madagascar, the East Madagascar Current (EMC). The fate of the EMC after separating from Madagascar's coast has been a subject of discussion. Based on the available hydrographic observations mboxLutjeharms (1976) suggested that the surface flow south of Madagascar was eastward, leading later to the suggestion of an EMC retroflexion similar to that of the Agulhas Current

Stability considerations

(Lutjeharms, 1988). However, based on chlorophyll data, Quartly and Srokosz (2004) found indications of different EMC regimes, sometimes corresponding to a retroflection, in other cases to a westward continuation towards the African coast. The eastward flow we observed from the climatology near the southwestern tip of Madagascar (Fig.4.3a) seems consistent with the observations of Lutjeharms (1976). Further east, the SICC could support the existence of an EMC retroflection and/or an eastward EMC return flow into the ocean interior. However, the SICC is shallow compared to the vertical extension of the EMC, so only the near-surface part of the EMC would be involved in such a retroflection.

In summary, both climatology and WOCE data reveal the SICC to be a shallow eastward current extending along the South Indian Ocean subtropical gyre over the westward flow of the SEC. With this sheared flow structure, instabilities of the SICC-SEC that explain the observed subtropical variability may be induced. To check this, in the next section we analyze the baroclinic instability of the SICC-SEC system in the context of a 2-layer model.

4.5 Stability considerations

A simple model to study baroclinic instability was introduced by Phillips (Phillips, 1954). In this approximation the ocean is represented by two layers of constant depth H_n and density ρ_n , with meridionally independent zonal velocities U_n in each layer ($n=1$ and 2). This implies that the interface between the two layers has a constant slope. Here we adopt this approximation to represent the vertical structure of the SICC-SEC system. For instance, Philander (1976) used the Phillips model to show that the North Equatorial Current may be baroclinically unstable. In the absence of friction and bottom topography, the linearized version of the quasigeostrophic potential vorticity equation (see Pedlosky, 1987) reads

$$\left(\frac{\partial}{\partial t} + U_n \frac{\partial}{\partial x}\right)q_n + \frac{\partial \Pi_n}{\partial y} \frac{\partial \phi_n}{\partial x} = 0 \quad (4.1)$$

where q_n is the perturbation potential vorticity, ϕ_n the perturbation stream function, and Π_n is the mean potential vorticity in layer n .

As U_1 and U_2 are independent of y , the normal mode solutions to Eq. (4.1), ϕ_n , have the form

$$\phi_n = \text{Re} [A_n \sin(l y) \exp i(k x - w t)] \quad (4.2)$$

where the magnitude of the wavenumber vector is $K^2 = k^2 + l^2$ and the frequency w is a complex, i.e. $w = w_r + i w_i$. The meridional wavenumber equals $l = m\pi/B$, where B is a typical meridional scale or width of the zonal channel.

The meridional gradient of the mean potential vorticity, Π_{ny} , reads

$$\Pi_{ny} = \beta - (-1)^n F_n (U_1 - U_2) \quad (4.3)$$

where

$$F_n = \frac{f_0^2}{g'H_n}$$

In the above equations β is the variation of the Coriolis parameter with latitude, f_0 is the Coriolis parameter at the reference latitude, g' is the reduced gravity, and F_n is the inverse of the square of the Rossby deformation radius in each layer.

The phase speed of the normal modes is given by $c = w/K$; then the argument of the exponential in (4.2) takes the form

$$\phi_n \sim \exp ik(x - c_r t) \exp kc_i t$$

with kc_i defined as the growth rate of the unstable modes.

Substitution of the solution (4.2) into equation (4.1) leads to a system of two ordinary differential equations for the amplitudes A_1 and A_2 (see Pedlosky, 1987). Requiring nontrivial solutions for this system yields a quadratic equation for c whose solutions are:

$$c = U_2 + \frac{U_s K^2 (K^2 + 2F_2) - \beta(2K^2 + F_1 + F_2)}{2K^2(K^2 + F_1 + F_2)} \pm \frac{[\beta^2(F_1 + F_2)^2 + 2\beta U_s K^4(F_1 - F_2) - K^4 U_s^2(4F_1 F_2 - K^4)]^{\frac{1}{2}}}{2K^2(K^2 + F_1 + F_2)} \quad (4.4)$$

where

$$U_s = U_1 - U_2 \quad (4.5)$$

To evaluate the instability potential of the SICC-SEC system we solved equation (4.4) considering only zonal wave propagation (i.e. $K^2 \sim k^2$) and using parameters derived from climatology. Inspection of the mean velocity profiles (Fig. 4.4, Fig. 4.6) shows that values of H_1 between 200-300 m and H_2 between 400-700 m are good choices for the depths of the upper and lower layers associated with the SICC and SEC, respectively. It is also seen from the velocity profile (Fig. 4.6b) that the flow exhibits little variation between 400-700 m; thus, U_2 is estimated as the average zonal flow over those depths, whereas U_1 equals the zonal velocity at the surface. As the climatology probably underestimates the actual value of the vertical shear it is reasonable to consider an upper bound estimation. The sensitivity to different estimations of the vertical shear will become clearer below. To analyze variations of the growth rate along the latitude band 20°-35°S the maximum growth rate kc_i was computed at each grid point, i.e. the spatial dependence of the vertical shear was taken into account. (Note that in the Phillips model U_s is called the shear).

Fig. 4.8 shows the maximum growth rate, kc_i , when $H_1 = 250$ m and $H_2 = 400$ m. Non-zero values are found between 24°-31°S and near the regions of maximum vertical shear (Fig.4.5). Comparison with Fig. 4.1 shows that the instability spots also lie close to the regions of maximum variability west of 90°E. The growth rates vary between $0.004 - 0.014$ day⁻¹, or equivalently between e -folding time scales from 70 to 250 days.

Stability considerations

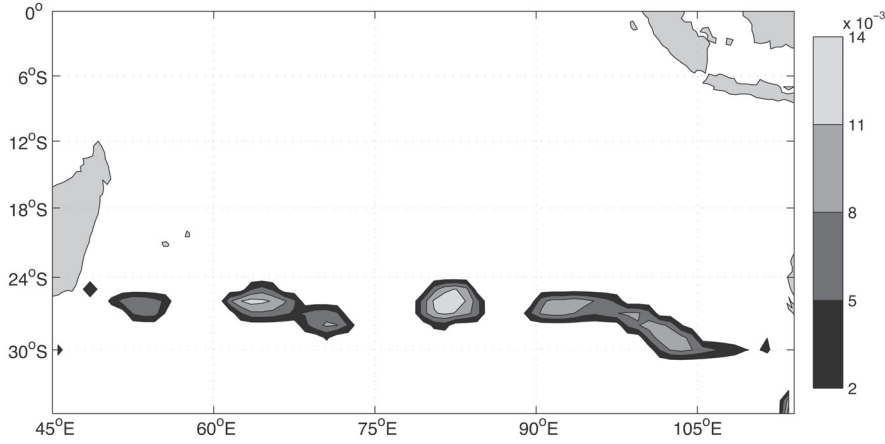


Figure 4.8: Maximum growth rate of the unstable modes estimated from the 2-layer Phillips model equations (equation 5.4), computed at each grid point over the South Indian Ocean. The model depth of the first and second layers is 250 m and 400 m, respectively. The velocity shear is estimated between the flow at the surface and the average flow between 400-600 m, from climatology. Units in days^{-1} . Results indicate that in the subtropical band between 24° - 30° S the flow is baroclinically unstable.

The wavelengths of the most unstable modes lie between 240-320 km, decreasing from north to south in agreement with the variation of R_0 . The southeastward tilt seen in kc_i east of 100° E coincides with a shift in the SICC core towards $\sim 29^\circ$ S. The largest growth rates are found near 64° E, 26° S and 82° E, 26° S (Fig. 4.9). They show a window of unstable wavelengths between 250-333 km, with maxima around 297 km and 283 km, and e -folding time scales between 75-80 days. The e -folding time scales predicted from the Phillips model are of the same order as those found for the countercurrents in the Pacific Ocean during the winter-spring season (Qiu, 1999; Qiu and Chen, 2004).

The above results are quite sensitive to the thickness of the second layer. For instance, a choice of $H_2 > 450$ m makes solutions of equation (4.4) stable over the subtropical domain. On the other hand, reducing the depth of the first layer tends to increase the instability potential of the subtropical current system. The sensitivity to H_2 is related to the necessary condition for instability in the Phillips model. For instability to occur the meridional gradient of the mean potential vorticity needs to change sign between the two layers, from equation (4.3) when $U_1 > U_2$ this reduces to:

$$\Pi_2 y < 0, \text{ or } U_s > \frac{\beta}{F_2} = \frac{\beta g' H_2}{f_0^2}$$

A slightly different criterion for baroclinic instability can be derived from the $2\frac{1}{2}$ -layer quasigeostrophic model equations. Qiu (1999) showed that when $U_1 > U_2$, the necessary condition states that the vertical shear has to overcome the beta effect plus a factor proportional to the stratification ratio, i.e.:

Flow structure and variability in the Subtropical Indian Ocean

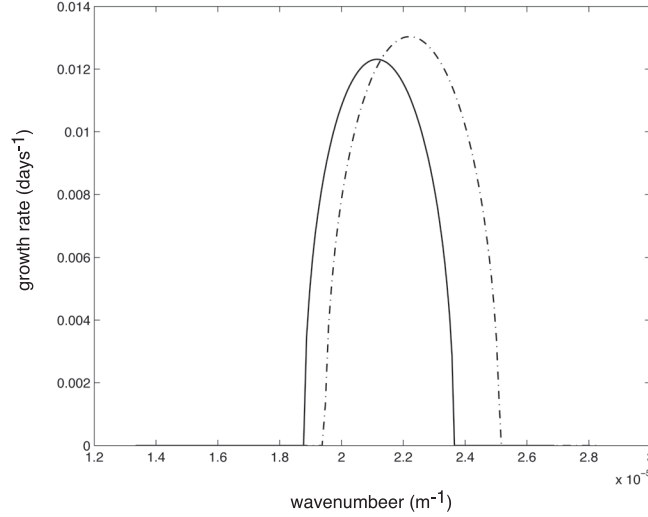


Figure 4.9: Growth rate as a function of the zonal wavenumber k calculated from equation (4.4) at $64^\circ E, 26^\circ S$ (solid line) and at $80E, 26^\circ S$ (dashed line). Both locations show similar e-folding times (between 75-80 days) and wavelengths for the most unstable modes (~ 290 km).

$$U_s > \frac{\beta}{F_2} + \gamma U_2 \quad (4.6)$$

where $\gamma = \frac{\rho_2 - \rho_1}{\rho_3 - \rho_2}$, and ρ_3 represents the density in the lower inert layer.

Results of equation (4.6) are similar to those in Fig. 4.8, although there is a slight increase in the instability potential over the subtropical latitude band 24° - $31^\circ S$. If H_2 becomes larger than 450 m the instability is also reduced.

Since the vertical shear from climatology is about 4 times smaller than that observed from synoptic hydrographic data (Fig. 4.6), we estimated the Phillips growth rate using the zonal velocity profile available at $80^\circ E, 24^\circ S$ (Fig. 4.7a). To compute kc_i , U_1 was estimated as the velocity averaged over the first 100 m and U_2 as the velocity averaged over the second layer thickness. H_1 was set equal to 250 m and H_2 was varied between 250-750 m. (Note that the change in the vertical shear due to varying H_2 is very small). Figure 4.10 shows that the e-folding time scales of the most unstable waves vary slowly when H_2 varies from 250 to 650 m, but it increases sharply from ~ 30 to 63 days when H_2 varies between 650-750 m. A depth of ~ 750 m for H_2 is probably the more realistic approximation of the vertical flow structure in this synoptic data set (see Fig. 4.6a). In this case the window of unstable wavelengths is 390-470 km, with $\lambda \sim 430$ km for the most unstable wave. This is in agreement with the dominant spatial scale of eddy variability estimated from observations (i.e. ~ 440 km, Fig. 4.2b). In addition, the frequency of the most unstable mode turns out to be around 5 times/year, though it varies in the range 3.5-6 times/year with small variations of the vertical shear (i.e. the frequency increases when the vertical shear decreases).

Summary and discussion

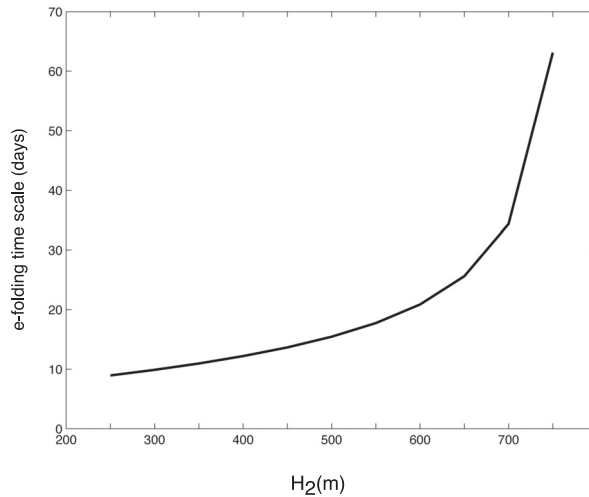


Figure 4.10: The e-folding time scale of the most unstable mode as a function of the second layer depth H_2 using parameters from WOCE synoptic hydrographic data at 80°E , 24°S (as in Figure 4.6a). The sensitivity of the growth rate to changes in H_2 is higher if the latter varies from 650 m to 750 m.

In conclusion, the frequency range generated by the baroclinic instability as detected near 80°E , 24°S is close to the observed subtropical Rossby wave variability of 4-5 times/year (Schouten et al., 2002). Although the results with synoptic hydrographic data are based on a single observation of the velocity profile, they support the hypothesis that regions of maximum vertical shear around 25°S are baroclinically unstable. It is likely that the analysis using climatology underestimates the vertical shear and thereby the expected instability along the subtropical band.

4.6 Summary and discussion

In this study, we have analyzed the flow structure in the South Indian Ocean subtropical gyre between 20° - 30°S . The climatology shows the existence of a shallow eastward jet with its core around 25°S , which flows over the deep reaching westward SEC. The presence of the eastward South Indian Ocean Countercurrent (SICC) is analogous to the subtropical countercurrents in the Pacific Ocean (Qiu, 1999; Qiu and Chen, 2004). This suggests that the forcing of the SICC could be similar to that in the Pacific. The position of the northernmost branch of the Subtropical Front in the South Indian Ocean lies further south than that in the Pacific (Belkin and Gordon, 1996). From the climatological data we have shown the existence of a secondary, subtropical frontal zone extending across the basin between 26° - 32°S in the west and between $\sim 20^\circ$ - 27°S in the east. The SICC might be its associated frontal jet. The connection of the SICC to the western boundary current at that latitude, the East Madagascar Current (EMC), is still unclear. Evidence for the existence of events of an EMC retroflection has been derived in the past from analyses of surface data (Lutjeharms, 1988; Quartly and

Srokosz, 2004). The shallow SICC could provide the mean large scale eastward flow to which a retroflexion of the upper layers of the EMC could connect. In the future, a combination of observations and modeling studies is needed to better determine the characteristics of the SICC, its forcing and variability.

The stability of the SICC-SEC vertical flow structure was analyzed using the Phillips 2-layer model (Phillips, 1954). We have shown that the SICC-SEC system satisfies the condition for baroclinic instability in this model: the meridional gradient of the mean potential vorticity changes sign around 200 m. In particular, areas of maximum vertical shear in the subtropical basin between 24° - 31° S are baroclinically unstable. The findings are confirmed in a stability analysis of the $2\frac{1}{2}$ -layer quasi-geostrophic model (see e.g. Qiu, 1999). The e -folding time scales found near 64° E and 82° E (~ 80 days) compare well with baroclinic instability time scales detected in the Pacific subtropical countercurrents (Qiu, 1999; Qiu and Chen, 2004). Given the simplicity of the 2-layer model and the quality of the database in this region of the South Indian Ocean, the range of unstable wavelengths (290-470 km) agrees surprisingly well with estimations of the wavenumber spectra from altimetry (~ 440 km). Analysis of the stability using synoptic hydrographic data along the 80° E section shows a range of unstable frequencies between 3.5-6 times/year. A similar subannual frequency is present in the SSH data along 25° S, consistent with the 4-5 times/year Rossby wave propagation detected by Schouten et al (2002). Therefore, baroclinic instability of the SICC-SEC system can explain the eddy variability observed along the 25° S band and the fact that a large part of the variance is in the subannual frequency range. It is also worth noticing that the possibility of barotropic instability across the SICC horizontal shear was evaluated following Lipps (1963). Assuming a simplified meridional profile for the upper layer currents, i.e. the SICC and SEC, and an infinite inert lower layer, no change in the sign of the meridional gradient of potential vorticity was detected in the fluid. In other words, the sufficient condition for barotropic stability is satisfied.

The altimetry data show high eddy kinetic energy (EKE) levels in the center of the South Indian Ocean subtropical gyre analogous to those observed along the subtropical Pacific Ocean (i.e. EKE ranges between 150 - 300 cm^2s^2). The region east of South Madagascar between 50° - 60° E is a particularly highly energetic area (see Fig. 1.6), with average EKE variations from 200 up to 1000 cm^2s^2 , and significant interannual variability over the period 1993-2003. EKE variations in the 25° S band may represent changes in the intensity and/or position of the SICC. Estimations of the EKE associated with the low frequency component of the SSH field (i.e. periods greater than 1 year) range between 20 - 70 cm^2s^2 . This suggests that a high percentage of the total EKE variability there is related to mesoscale processes. Eddies propagating from the western Australian coast into the Indian Ocean could be tracked only up to 90° E (Fang and Morrow, 2003). It is plausible that variability generated locally by baroclinic instability in the subtropical Indian Ocean and propagating along 25° S connects with the eddy activity observed southeast and south of Madagascar (Schouten et al., 2002; de Ruijter et al., 2004; Quartly and Srokosz, 2004). The processes relating the Rossby wave activity and observed eddies are, however, not obvious. A theoretical analysis by Halliwell et al. (1994) showed that in a baroclinically unstable system initially wavelike perturbations might develop into large eddy structures due to a non-linear energy cascade. In the region east of South Madagascar, the convergence of eddy variability from the central Indian Ocean, plus non-linear interaction with local instabilities of the SICC, may induce the large EKE.

Summary and discussion

High levels of EKE also exist in the South Indian Ocean over the SEC path (i.e. EKE ranges between 100-400 cm^2s^2). The stability analysis based on the Phillips 2-layer model shows that the SEC vertical shear is stable. However, an analysis of the continuously stratified system showed that the SEC in the eastern Indian Ocean is baroclinically unstable, with the largest growth rates (e -folding time scales of less than 50 days) during the July-September season (Feng and Wijffels, 2002). North of Madagascar the SEC is barotropically unstable at a period of 50 days, inducing this frequency of variability in the eddy activity drifting south into the Mozambique Channel (Schott et al., 1988; Schouten et al., 2003).

Finally, the EKE along 25°S shows a regular seasonal variation, with minima around May and maxima in November. Qiu (1999) and Qiu and Chen (2004) showed that the seasonal modulation of the EKE in the subtropical Pacific countercurrents is related to seasonal variations in the growth rate of the baroclinic waves. Analysis of seasonal velocity profiles from climatology reveals that the SICC is stronger (weaker) in austral summer (winter), while the SEC weakens (strengthens) due to the large-scale wind variability (Tchernia, 1980). As a consequence, the shear of the SICC-SEC system is high in summer and winter, leading to baroclinic instability with e -folding time scales between 40-50 days in both seasons. Therefore, the growing time of a perturbation can explain the appearance of maximum variability towards November, but not the spring minimum. Future studies using better quality observations of the seasonal velocity profiles as well as density sections, will be needed to analyze seasonal variations of the SICC-SEC system and their possible relation to the annual variability of the EKE. The use of 2-layer models has strengths and shortcomings as pointed out by Gill et al. (1974). Two problems of the two-layer model are the neglect of horizontal density variations, which could affect the stability properties, and the constrained choice of values of layer depths and g' . More accurate analyses of the continuously stratified system will also require an ensemble of hydrographic observations that is not currently available for the South Indian Ocean.

Chapter 5

Non-linear effects on the circulation around an island, with application to Madagascar

5.1 Introduction

The presence of Madagascar in the South Indian Ocean sets unique characteristics to the subtropical gyre circulation. This large-scale island, located roughly between 12° - 25° S, blocks the wind-driven circulation between those latitudes, i.e. the westward flowing South Equatorial Current (SEC) bifurcates at the eastern Madagascar coast around 17° S generating two western boundary currents: the North Madagascar Current (NMC) to the north and the East Madagascar Current (EMC) to the south (Swallow et al., 1988). The fate of the EMC at its termination point it is still not fully established: either an eastward retroflection with subsequent eddy shedding (Lutjeharms, 1988) or westward continuation as a free jet toward the African coast (Quarty and Srokosz, 2004) are possible regimes. It could also involve partial retroflection in the upper layer, with a connection to the South Indian Ocean Countercurrent (Palastanga et al., 2007). The main subtropical gyre western boundary current, the Agulhas Current, originates around 27° S along the African coast.

A description of the South Indian Ocean subtropical gyre based on historical hydrographic observations is given in Stramma and Lutjeharms (1997). The flow integrated over the upper 1000 m shows a southwestern recirculation to the south of Madagascar and a broad westward return flow between 10° - 30° S. The recirculation, the EMC and the flow from the Mozambique Channel are sources of the Agulhas Current (AC), each of them contribute with 35 Sv, 20 Sv and 5 Sv to the AC transport (Stramma and Lutjeharms, 1997). A recent analysis of climatological data revealed a surface anticyclonic circulation to the east of Madagascar that comprises of an eastward current around 25° S, named the South Indian Ocean Countercurrent (SICC), and, between 10° - 20° S, of the westward flow of the SEC (Palastanga et al., 2007). The SICC extends in the upper 300 m to 95° E, with a maximum transport of 10 Sv (Siedler et al., 2006). A mean dynamic topography of the South Indian Ocean (Rio

Non-linear effects on the circulation around an island, with application to Madagascar

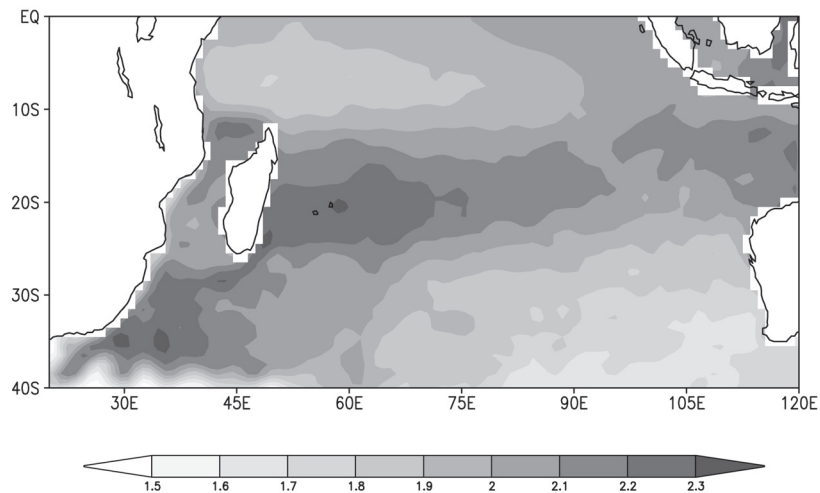


Figure 5.1: *Dynamic topography of the South Indian Ocean computed from hydrographic data, surface drifters and altimetry (Rio and Hernandez, 2004). Units in m^2s^{-2} . It shows the anticyclonic subtropical gyre circulation at the surface between 12° – 40° S, with two separate recirculations, one to the east of Madagascar and another east of South Africa.*

and Hernandez, 2004) illustrates the existence of two subgyres (i.e. to the east and south of Madagascar) possibly connected in the region around South Madagascar (Fig. 5.1). While Stramma and Lutjeharms (1997) suggested that the southwestern recirculation cell might be related to bottom topography, issues like the dynamical connection between the subgyres, or their relation to the wind stress curl over the basin, have not been addressed.

The nature of the flow in the Mozambique Channel seems determined by the southward propagation of anticyclonic eddies rather than by a continuous western boundary current as previously thought (Di Marco et al., 2002; De Ruijter et al., 2002). The circulation in the northern part of the Channel is characterized by an anticyclonic loop with southward flow to the west and northward (and weaker) flow to the east (Donguy and Piton, 1991). Ridderinkhof and De Ruijter (2003) measured a net southward transport of 14 Sv in the narrows of the Mozambique Channel, with a frequency of 4 times/year related to the pinching off of anticyclonic eddies from the northern anticyclonic loop. Eddies have been traced with satellite altimetry migrating southward along the Channel and into the AC system (Biaostoch and Krauss, 1999; Schouten et al., 2002). The region to the south of Madagascar also presents high eddy activity, with eddies propagating toward the AC (Gründligh, 1995; Schouten et al., 2000; Quartly and Srokosz, 2004; De Ruijter et al., 2004). Ultimately, Madagascar eddies may influence the variability of the AC retroflexion and/or the formation of Agulhas rings (Schouten et al., 2002a; De Ruijter et al., 2004), forming an important link in the global ocean circulation.

Only few modeling studies were devoted to investigate the large-scale South Indian Ocean circulation. Matano et al. (1999) used a primitive equation model to study the adjustment of

Introduction

the South Indian Ocean between 20° - 50° S to seasonal wind variations. They found that the mean baroclinic circulation reproduces well the inertial recirculation and the AC, whereas the mean barotropic circulation is constrained in the central basin due to the blocking effect of bottom topography. Using a $1\frac{1}{2}$ -layer model forced by Hellerman and Rosenstein (1983) climatological winds, Woodberry et al. (1989) simulated the monsoonal Tropical Indian Ocean circulations. As their model domain extended to 25° S, where open boundary conditions were applied, the flows in the Mozambique Channel and the EMC were not fully analyzed. Other studies for instance have focused on the influence of Madagascar eddies onto the AC system through analyses of eddy resolving numerical models (Biastoch and Krauss, 1999; Penven et al., 2006).

Godfrey (1989) derived a linear analytical model to account for the effect of large-scale islands on the Sverdrup circulation. He derived the so called Island Rule, which states that the transport between the island and the ocean's eastern boundary can be quantified by the circulation of the wind stress along a closed path that enfolds the island's western boundary. Godfrey reasoned that it is licit to neglect inertial, frictional and/or topographic effects around the island, as long as the island's eastern boundary (i.e. where western boundary currents occur) is avoided. The linear island rule has succeeded in predicting the stationary circulations around Hawaii in the North Pacific (Qiu et al., 1997) and New Zealand in the South Pacific (deSzoek, 1987). Godfrey (1989) estimated the transport around Madagascar to be 4 ± 3 Sv based on Hellerman and Rosenstein (1983) winds, but since then no other indirect estimates of the Mozambique Channel throughflow have been reported. Pedlosky et al. (1997) revisited the validity of the Island Rule when frictional and non-linear effects become important, for instance if eddies are shed at the island extremities. In a series of idealized experiments with barotropic models they found that even in highly non-linear regimes the Island Rule predicts between 80-90% of the modeled transports. In addition, they showed the existence of a linear recirculation to the east of an island when the Sverdrup interior stream function presents (at least) one extreme between the island northern and southern latitudes. Quick inspection of the wind stress curl in the South Indian Ocean (see e.g. Fig. 2.1) suggests that such linear recirculation cannot be expected to the east of Madagascar, as the minimum and maximum in the curl are present around 10° S and 40° S, respectively.

Non-linear effects on the circulation around Madagascar are expected to be important due to the complex boundary current system and the significant local mesoscale eddy activity, in particular near the separation regions at the northern and southern extremities of the island. In this Chapter we investigate the effect of non-linearity on the western boundary currents around Madagascar and the impact of non-linear flow interactions on the transport through the Mozambique Channel. A specific question is to test the validity of the linear island rule around Madagascar when inertial and/or frictional effects become more significant. We use continuation techniques within a shallow-water, barotropic model to examine dependencies of the steady circulation on wind stress amplitude and pattern. Therefore, branches of steady solutions are followed in parameter space as for example the wind stress amplitude is varied. One simplification in the model is excluding bottom topography. Numerical studies have shown that the Indian Ocean meridional ridges act as a barrier for annual barotropic signals forced by the winds in the central Indian Ocean (Kindle, 1991; Matano et al., 1999). This probably explains why in situ observations across the EMC and NMC did not detect any significant seasonal variability (Swallow et al., 1988). In this study we do not aim to analyze the

variability (i.e. seasonal) of the circulation around Madagascar, but rather to study different steady solutions caused by different wind patterns and strength. Another simplification in the model is the existence of an open zonal channel of constant depth in the south that prevents non-linearities associated with the recirculation of the subtropical western boundary current to dominate the solution for large amplitudes of the wind stress.

This Chapter is organized as follows. A complete description of the model, data and experiments set up is given in Section 5.2. Section 5.3 starts with the formulation of the generalized island rule, followed by its linear application to the transport through the Mozambique Channel. Section 5.4 discusses first the characteristics of the model circulation forced by annual mean winds and its sensitivity to friction and inertia. Then, the steady circulations forced by wind fields whose profiles and amplitudes differ from the annual mean case are presented. Finally, Section 5.5 offers a summary and discussion of the results.

5.2 The model

We use the same barotropic, shallow water model as Dijkstra and de Ruijter (2001), but we will ignore bottom topography. The model has a single layer with constant density, ρ , and equilibrium thickness, H . The model involves the shallow water equations in spherical coordinates ϕ , θ , and z . The flow is driven by a surface wind stress field, $\vec{\tau}(\phi, \theta) = \tau_0(\tau^\phi, \tau^\theta)$, where τ_0 is the amplitude (in Nm^{-2}) and (τ^ϕ, τ^θ) provides the spatial pattern. Lateral Laplacian friction, with lateral friction coefficient, A_H , is the only dissipative mechanism in the model. The model's horizontal domain covers the South Indian Ocean from 20°E to 90°E and from 41°S to 5°S , and includes realistic geometry. All boundaries are bounded by a closed contour, Γ , except in the south where a zonal channel extends from the southern wall to 36°S .

The model equations are non-dimensionalized using typical scales r_0 , H , U , r_0/U , and τ_0 for length, layer depth, velocity, time, and wind stress amplitude, respectively, where r_0 is the radius of the earth. The non-dimensional equations are then

$$\begin{aligned} \epsilon \left(\frac{\partial u}{\partial t} + \frac{u}{\cos \theta} \frac{\partial u}{\partial \phi} + v \frac{\partial u}{\partial \theta} - uv \tan \theta \right) - v \sin \theta = \\ - \frac{\epsilon F}{\cos \theta} \frac{\partial \eta}{\partial \phi} + E \left(\nabla^2 u - \frac{u}{\cos^2 \theta} - \frac{2 \sin \theta}{\cos^2 \theta} \frac{\partial v}{\partial \phi} \right) + \alpha \frac{\tau^\phi}{h} \end{aligned} \quad (5.1a)$$

$$\begin{aligned} \epsilon \left(\frac{\partial v}{\partial t} + \frac{u}{\cos \theta} \frac{\partial v}{\partial \phi} + v \frac{\partial v}{\partial \theta} + u^2 \tan \theta \right) + u \sin \theta = \\ - \epsilon F \frac{\partial \eta}{\partial \theta} + E \left(\nabla^2 v - \frac{v}{\cos^2 \theta} + \frac{2 \sin \theta}{\cos^2 \theta} \frac{\partial u}{\partial \phi} \right) + \alpha \frac{\tau^\theta}{h} \end{aligned} \quad (5.1b)$$

$$\frac{\partial h}{\partial t} + \frac{1}{\cos \theta} \left(\frac{\partial(hu)}{\partial \phi} + \frac{\partial(hv) \cos \theta}{\partial \theta} \right) = 0 \quad (5.1c)$$

where (u, v) are the velocities in the eastward and northward direction, $\eta(\phi, \theta, t)$ is the free surface elevation, (τ^ϕ, τ^θ) are the components of the wind stress, and h is the thickness of the water column (with equilibrium value H). Note that due to the flat bottom changes in h are due only to changes in the sea surface height, i.e. $h = H + \eta(\phi, \theta, t)$.

The model

The non-dimensional parameters in the momentum equations are the Rossby number, ϵ , the inverse Froude number, F , the Ekman number, E , and the wind stress coefficient, α . Expressions for these parameters are

$$\epsilon = \frac{U}{2\Omega r_0}; F = \frac{gH}{U^2}; E = \frac{A_H}{2\Omega r_0^2}; \alpha = \frac{\alpha_0 \tau_0}{2\Omega \rho H U} \quad (5.2)$$

where Ω is the angular velocity of the earth. The amplitude of the wind stress within the model, called hereafter τ_m , is varied by the the control parameter α_0 used in the continuation technique, i.e. $\tau_m = \alpha_0 \tau_0$.

On the boundary of the domain no-slip conditions are implemented; so that

$$(\phi, \theta) \in \Gamma : u = v = 0 \quad (5.3)$$

whereas on the lateral sides of the southern open channel periodic boundary conditions are applied.

The model equations are discretized on a staggered Arakawa C-grid using second-order central differences on a standard resolution of $1/5^\circ$ in both zonal and meridional directions. A continuation technique based on the pseudoarclength method by Keller (1977) is used to determine steady state solutions as the control parameter is continuously varied. The wind stress amplitude in the model is varied by varying α_0 from 1 to 5. For the reference experiment $\alpha_0 = 1$ and τ_0 represents the maximum amplitude of the annual mean wind stress; the reference layer thickness is $H = 500$ m, and the Laplacian friction coefficient equals to $A_H = 1000 \text{ m}^2 \text{ s}^{-1}$, which gives an Ekman number $E = 1.6 \cdot 10^{-7}$. Steady solutions using E as control parameter (i.e. varying E one order of magnitude) are also computed. Standard values of all other parameters used in the model are listed in Table 5.1.

Parameter	Value	Parameter	Value
Dimensional parameters			
r_o	$6.4 \times 10^6 \text{ m}$	τ_o	$1.6 \times 10^{-1} \text{ Pa}$
H	$5 \times 10^2 \text{ m}$	A_H	$1.0 \times 10^3 \text{ m}^2 \text{ s}^{-1}$
ρ_o	$1.0 \times 10^3 \text{ kg m}^{-3}$	U	0.1 m s^{-1}
g	9.8 m s^{-2}	Ω	$7.29 \times 10^{-5} \text{ s}^{-1}$
Dimensionless parameters			
ϵ	1.0×10^{-4}	E	1.6×10^{-7}
α	2.2×10^{-2}	F	4.9×10^5

Table 5.1: Standard values for the parameters in the barotropic shallow water model. The scale of the wind stress τ_0 corresponds to the maximum amplitude of the annual mean wind stress; in other experiments it will equal the maximum amplitude of July and January wind stresses. The value of α is computed with α_0 equal to 1; throughout the experiments α_0 will vary from 1 to 5.

The model has been forced by the momentum flux fields obtained from the NCEP reanalysis data for the period 1948-2003 (Kalnay et al., 1996). The data, which are originally given

on a Gaussian grid with approximately 2° horizontal resolution, have been interpolated onto the model's grid. In addition, the data have been modified over the southern domain in order to constrain the flow's amplitude in the open channel. We use annual mean winds as well as the monthly means of January and July, which have maximum amplitudes of 0.16 Pa, 0.22 Pa and 0.33 Pa, respectively. Figure 5.2 shows a zonal average of the wind stress curl for the annual mean, and the patterns of January and July times a factor of 5. There is, as expected, a seasonal shift of the zero curl contour from around 22°S in January to 16°S in July, with the annual mean resembling the latter. Since the wind stress in the southern part of the domain was set to a constant amplitude equal to 0.001 Pa, the region of positive curl extends as far as 36°S (32°S) in January (July), while in reality this limit is found between 45° - 50°S .

5.3 Island rule formulation

5.3.1 Theory

In this section we derive the island rule in the context of the shallow water equations (5.1). Godfrey (1989) considered the steady momentum equations integrated from the surface to an assumed depth of no motion. Along a path that avoids western boundary layers, i.e. that connects the western side of the island with the basin eastern boundary, lateral and bottom friction can be neglected. Furthermore, due to the no-normal flow condition across boundaries, the pressure between the island tips must be constant. This leads to a constraint for the value of the barotropic stream function on the island, which is constant in a steady state.

Let us consider the steady form of the momentum equations (5.1a, 5.1b) multiplied by the total layer depth, h

$$\begin{aligned} & \epsilon \left(\frac{hu}{\cos\theta} \frac{\partial u}{\partial\phi} + hv \frac{\partial u}{\partial\theta} - huv \tan\theta \right) - hv \sin\theta = \\ & - \frac{\epsilon F}{\cos\theta} h \frac{\partial h}{\partial\phi} + E \left(h\nabla^2 u - \frac{hu}{\cos^2\theta} - \frac{2\sin\theta}{\cos^2\theta} h \frac{\partial v}{\partial\phi} \right) + \alpha\tau^\phi \end{aligned} \quad (5.4a)$$

$$\begin{aligned} & \epsilon \left(\frac{hu}{\cos\theta} \frac{\partial v}{\partial\phi} + hv \frac{\partial v}{\partial\theta} + hu^2 \tan\theta \right) + hu \sin\theta = \\ & - \epsilon F h \frac{\partial h}{\partial\theta} + E \left(h\nabla^2 v - \frac{hv}{\cos^2\theta} + \frac{2\sin\theta}{\cos^2\theta} h \frac{\partial u}{\partial\phi} \right) + \alpha\tau^\theta \end{aligned} \quad (5.4b)$$

Noticing that $\frac{1}{\cos\theta} \frac{\partial v}{\partial\phi} - \frac{\partial u}{\partial\theta}$ is the vertical component of the relative vorticity, ζ , in spherical coordinates, the vectorial form of the steady shallow water equations reads

$$\begin{aligned} & \epsilon(\vec{k} \wedge \vec{u} h\zeta) + \epsilon(\vec{k} \wedge \vec{u} hu \tan\theta) + \vec{k} \wedge \vec{u} h \sin\theta = \\ & -\epsilon\nabla \left(\frac{Fh^2}{2} \right) - \epsilon h\nabla \left(\frac{|\vec{u}|^2}{2} \right) + D + T \end{aligned} \quad (5.5)$$

where \vec{k} is a vertical unit vector, the horizontal nabla operator in spherical coordinates equals $\nabla = \left(\frac{1}{r\cos\theta} \frac{\partial}{\partial\phi}, \frac{1}{r} \frac{\partial}{\partial\theta} \right)$, and the wind stress and dissipation terms have been written for sim-

Island rule formulation

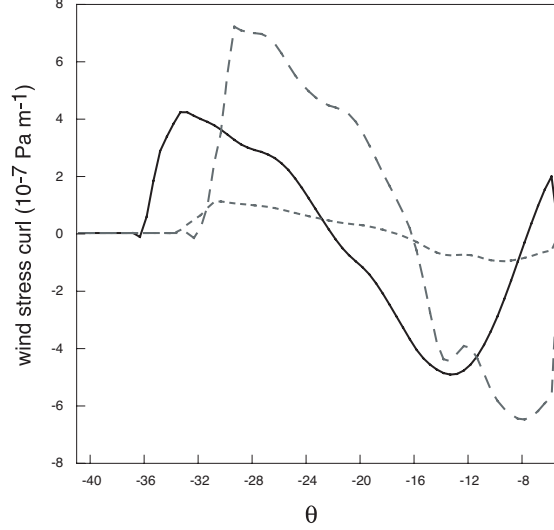


Figure 5.2: Zonal average of the wind stress curl in the Indian Ocean between 50° - 90° E for the annual mean (short dashed line), the pattern of July times a factor 5 (long dashed line), and the pattern of January times a factor 5 (solid black line). The zero wind stress curl at mid latitudes is not realistic; it is due to a modification in the data in the southern model domain.

plicity as T and D , respectively. Applying the circulation integral to (5.5) along the closed circuit C (Fig. 5.3) in a counterclockwise sense leads to

$$\begin{aligned} \epsilon \oint_C h \zeta \vec{u} \cdot \vec{n} ds + \epsilon \oint_C h u \tan \theta \vec{u} \cdot \vec{n} ds + \oint_C h \sin \theta \vec{u} \cdot \vec{n} ds = \\ \oint_C T \cdot \vec{t} ds + \oint_C D \cdot \vec{t} ds - \epsilon \oint_C h \nabla \left(\frac{|\vec{u}|^2}{2} \right) \cdot \vec{t} ds \end{aligned} \quad (5.6)$$

where \vec{t} and \vec{n} are the unit tangent and normal vectors to the contour C , and the circulation of the pressure term in the right hand side of (5.5) has dropped because it is the closed integral of a perfect differential. Note also that due to the factor h associated with the shallow water model the last term in (5.6) does not cancel over the closed circuit. The equation states that the sum of the (vertically integrated) planetary vorticity flux and the relative vorticity flux out/in to the region enclosed by C equals the total contribution of the wind stress and friction along C , plus the contribution from metric and non-linear terms.

Taking into account the no-slip boundary condition, it is useful to write the planetary vorticity flux as the sum of the zonal integrals along the northern and southern latitudes of the island, namely θ_n and θ_s ,

Non-linear effects on the circulation around an island, with application to Madagascar

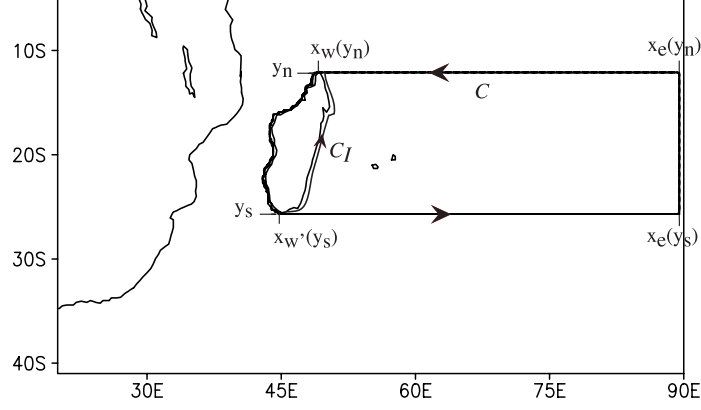


Figure 5.3: The South Indian Ocean domain, with the contour C connecting Madagascar's western boundary and the eastern boundary of the basin, X_e . The contour runs between Madagascar's northern, Y_n , and southern, Y_s , latitudes in an anticlockwise sense. The contour C_I runs anticlockwise around Madagascar

$$\begin{aligned}
 \sin \theta_n \int_{X_w}^{X_e} h v \cos \theta_n d\phi - \sin \theta_s \int_{X'_w}^{X_e} h v \cos \theta_s d\phi = \\
 -\epsilon \oint_C \zeta h \vec{u} \cdot \vec{n} ds - \epsilon \oint_C h u \tan \theta \vec{u} \cdot \vec{n} ds \\
 + \oint_C T \cdot \vec{t} ds + \oint_C D \cdot \vec{t} ds - \epsilon \oint_C h \nabla \left(\frac{|\vec{u}|^2}{2} \right) \cdot \vec{t} ds
 \end{aligned} \tag{5.7}$$

The two integrals on the left hand side of (5.7) are the transport between the island and the basin eastern boundary, which are equal by mass conservation in a barotropic, incompressible fluid. Thus, in dimensional form

$$\begin{aligned}
 (f_n - f_s) \Psi_I = \oint_C T \cdot \vec{t} ds + \oint_C D \cdot \vec{t} ds - \oint_C h \zeta \vec{u} \cdot \vec{n} ds \\
 - \frac{1}{r_0} \oint_C h u \tan \theta \vec{u} \cdot \vec{n} ds - \oint_C h \nabla \left(\frac{|\vec{u}|^2}{2} \right) \cdot \vec{t} ds
 \end{aligned} \tag{5.8}$$

This is the expression of the island rule in spherical coordinates, where Ψ_I is the barotropic stream function on the island, and f_n, f_s are the expressions of the Coriolis parameter on the latitudes of the island's northern and southern tips. In a closed basin, Ψ_I is also the transport around the island, i.e. between the island and all basin boundaries. Note that the metric term on the right hand side of (5.8) is usually ignored. Furthermore, if non-linear and

Island rule formulation

dissipation terms are neglected, then the linear Island Rule by Godfrey (1989) is obtained

$$\Psi_I = \frac{1}{(f_n - f_s)} \oint_C \frac{\vec{\tau}}{\rho} \cdot \vec{t} ds \quad (5.9)$$

in which the transport around the island as a function of only the circulation of the wind stress along C . The Island Rule can also be expressed in terms of the Sverdrup stream function. Separating the total contribution of the wind in (5.9) into that in a circuit around the island C_I (Fig. 5.3) and that in a circuit that runs counterclockwise between the island's eastern boundary and the basin's eastern boundary, so that the path along the island's eastern boundary cancels, and using Stokes theorem, equation (5.9) becomes

$$(f_n - f_s) \Psi_I = \oint_{C_I} \frac{\vec{\tau}}{\rho} \cdot \vec{t} ds + \int_{X_w}^{X_e} \int_{Y_s}^{Y_n} \text{curl}(\vec{\tau}/\rho) dx dy \quad (5.10)$$

using a definition of the Sverdrup streamfunction, i.e.

$$\Psi^s = -\frac{1}{\beta} \int_X^{X_e} \vec{k} \cdot \nabla \wedge T dx',$$

equation (5.9) becomes

$$(f_n - f_s) \Psi_I = \oint_{C_I} \frac{\vec{\tau}}{\rho} \cdot \vec{t} ds - \beta \int_{Y_s}^{Y_n} \Psi^s(X_I, y) dy \quad (5.11)$$

where X_I denotes the island's eastern boundary and β is the variation of the Coriolis parameter with latitude.

Therefore, the Island Rule states that the transport between the island and the basin eastern boundary results from a local contribution due to the wind stress around the island and from the remotely forced Sverdrup transport averaged between the island's northern and southern tips at the island's eastern coast. In general, the Sverdrup component is quite well known in a basin, and the primary unknown of the island rule is the western boundary current around the island. The latter, however, could be much less important than the former.

5.3.2 Application to the Mozambique Channel throughflow

The island's barotropic stream function in (5.9) is computed using wind stress fields from the NCEP reanalysis data (Section 5.2). To compare estimates from different wind data sets, we perform the same calculation using scatterometers winds from the European Remote Sensing satellite (ERS) and QuikSCAT (QuikSCAT) satellites. Wind stress fields derived from those data are available over $1^\circ \times 1^\circ$ and $0.5^\circ \times 0.5^\circ$ horizontal grids, respectively (see Section 2.2a). Due to their higher resolution it is expected that the latter give more accurate estimations of the Island Rule than NCEP data. Error estimates for calculations with ERS and QuikSCAT wind stresses are also presented.

The annual mean transport estimates (Table.5.2) vary from 3.2 Sv (NCEP) to 1.6 Sv (ERS), which falls in the range predicted by Godfrey (1989) using Hellerman and Rosenstein

Data set	QuikScat	ERS	NCEP
Annual mean	-2.18±0.02	-1.62±0.05	-3.20
January	8.43±0.08	4.27±0.16	5.29
July	-9.91±0.08	-6.44±0.19	-11.29

Table 5.2: Estimates of the Island Rule (equation (5.9)) based on three independent wind data sets, namely NCEP, ERS and QuikSCAT. Errors for the latter two are also shown. Units in Sv.

(1983) winds (i.e. 4 ± 3 Sv). Because ERS and QuikSCAT data sets cover different (and relatively short) periods, their differences might reflect interannual variations in the Mozambique Channel transport. For instance, during the years that ERS operated (1991-2000), analysis of altimetry data in the Mozambique Channel showed two periods of low eddy kinetic energy associated with the Indian Ocean Dipole/ENSO events (Palastanga et al., 2006). Such variations could cause decreases in the Channel’s flow. The Island Rule is also tested using July and January winds: the southwest monsoon induces large transports through the Channel in boreal summer, while in boreal winter the direction of the wind driven transport reverses (Table 5.2). These seasonal variations should be interpreted carefully, as the Island Rule was derived for a steady circulation excluding bottom topography. In addition, local seasonal wind effects in the southwestern Indian Ocean, and in particular the region around Madagascar, can be important (e.g. Fig. 2.4). Moreover, studies do not agree on the seasonality of the Mozambique Channel flow, e.g. in situ observations did not detect any seasonal dependence (Ridderinkof and de Ruijter, 2003), but ocean general circulation models simulations suggest a strong change in transport with seasons (Biastoch et al., 1999).

5.4 Model results

5.4.1 Initial experiment

We begin the model experiments using annual mean wind stresses, a layer depth $H = 500$ m and lateral friction coefficient $A_H = 1000 \text{ m}^2\text{s}^{-1}$. The Munk or frictional boundary layer thickness can be estimated as $\delta_M = (A_H/\beta)^{\frac{1}{3}}$. Based on the parameters in Table 5.1 this gives ~ 36 km along the eastern Madagascar coast, thus the Munk boundary layer is well resolved by the model’s resolution of ~ 20 km. A measure of non-linearity can be estimated by the ratio δ_I/δ_M , where $\delta_I = \sqrt{(U_I/\beta)}$ is the inertial boundary layer thickness and U_I is a typical interior velocity. For $\delta_M \gg \delta_I$, the flow is dominated by linear dynamics. In the reference experiment, the ratio δ_I/δ_M is close to 1, indicating that the flow is in a regime in which both inertia and dissipation are important in the fluid boundary layers.

The model stream function displays a typical anticyclonic/cyclonic gyre circulation south/north of 20°S (Figure 5.4a). The westward interior flow is diverted north and south at the coast of Madagascar forming island boundary currents that mimic the NMC and EMC. South of the island, the EMC flows straight to the African coast to join the gyre western boundary current, called hereafter (also) for simplicity, the AC. A recirculation region ap-

Model results

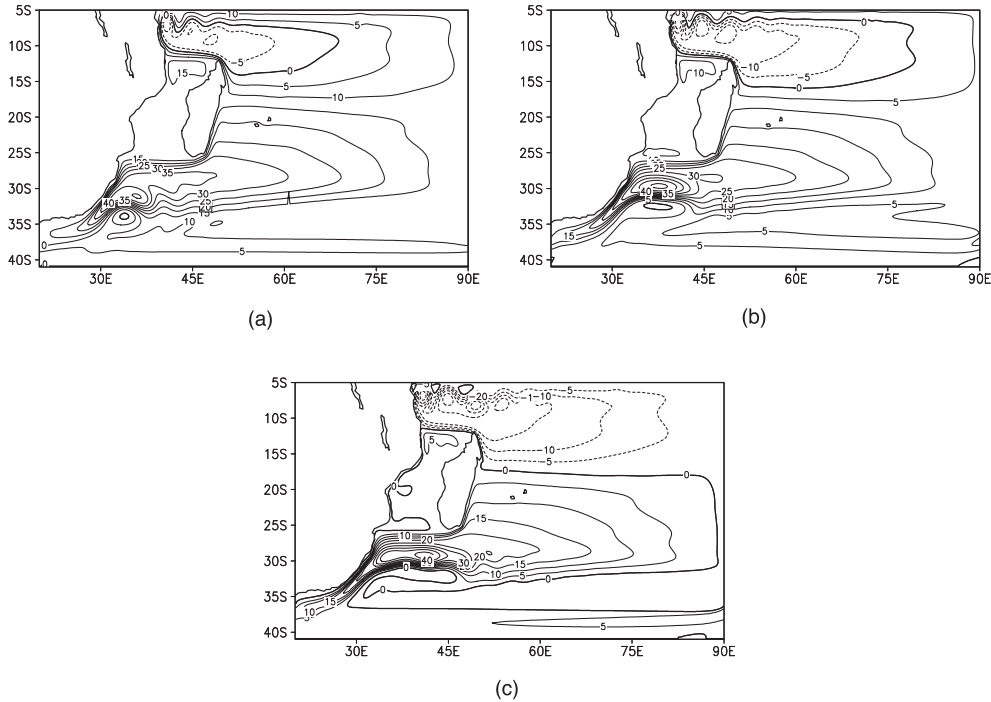


Figure 5.4: Barotropic stream function for the reference experiment. The model was forced by annual mean winds, with $H = 500$ m and (a) $E = 1.6 \cdot 10^{-7}$, (b) $E = 9.2 \cdot 10^{-8}$ and (c) $E = 5.6 \cdot 10^{-8}$. The value of α is as shown in Table 5.1. Contours every 5 units. Units in Sv.

pears to the east of the AC, with a maximum transport of 40 Sv. This simulates quite well the subtropical recirculation described by Stramma and Lutjeharms (1997). The flow in the southern open channel transports around 10.6 Sv towards the east. Along the northern wall stationary Rossby waves are formed as the outflowing western boundary current re-enters the interior flow (Pedlosky, 1987).

The largest model velocities are found along the AC path, with magnitudes up to 0.6 m/s near 29° S. Velocities near the separation regions of the western boundary currents at the islands northern and southern tips show values of around 0.3 m/s and ~ 0.4 m/s. Observations of the AC flow between 27° - 34° S have indicated mean speeds of 1.4-1.6 m/s, with peaks up to 2.6 m/s (Pearce and Grndligh, 1982). On the other hand, geostrophic velocities for the upper 500 m in the NMC vary from 0.3 m/s to 1 m/s, while in the EMC maximum surface velocities reach ~ 0.67 m/s (Swallow et al., 1988). Therefore, the model velocities are quite close to observations of the western boundary flows around Madagascar and lower than the real AC.

The model shows a rather weak flow in the Mozambique Channel, except in the northern part where a local anticyclonic circulation of 15 Sv is formed. The velocities in the northern loop are ~ 0.045 m/s and they decrease to ~ 0.02 m/s further south along the Channel's western side. Transport estimates were performed at sections across the Mozambique Channel

Non-linear effects on the circulation around an island, with application to Madagascar

	NMC	Moz. Channel	EMC	SMC	AC
1000m	13.31	-2.82	-11.64	-22.27	-31.61
*	-1.14	0.24	1.00	1.91	2.72
500 m	11.55	-2.51	-10.20	-20.74	-29.18
*	-1.13	0.25	1.00	2.03	2.86
250 m	10.07	-2.39	-8.73	-19.48	-27.29
*	-1.15	0.27	1.00	2.23	3.12

Table 5.3: *Transports of the North Madagascar Current (NMC) at 14°S, the Mozambique Channel (MC) throughflow at 20°S, the East Madagascar Current (EMC) at 23°S, the flow off southern Madagascar (SMC) at 45°E, and the Agulhas Current (AC) at 30°S for the experiments with different layer depths. For the western boundary currents along the eastern coast of Madagascar sections of 100 km width were considered, while the transports across the SMC and AC were computed along sections of 200 km width. (*) Ratio of the NMC, MC flow, SMC and AC to the EMC. The usual convention of positive transport in the northward and eastward directions is used. Units in Sv.*

(MC), AC, NMC, EMC, and off the southern Madagascar coast (SMC). (More details of the calculations can be found in Table 5.3). The EMC and NMC carry a transport of ~ 10 Sv along the eastern Madagascar coast, whereas the contribution to the AC from the south of the island is ~ 20 Sv. The transport in the modeled AC is about half its real value (Stramma and Lutjeharms, 1997). This is probably due to the reduced input of anticyclonic vorticity in the southern part of the model domain (see Fig. 5.2). The net southward transport through the Channel is 2.5 Sv (Table 5.3), whereas the linear island rule prediction (equation (5.9) within the model) is 3.6 Sv.

We also compute steady solutions using the Ekman number as control parameter (i.e. decreasing δ_M). The pattern of the circulation for $E = 9.2 \cdot 10^{-8}$ and $E = 5.6 \cdot 10^{-8}$ (Fig. 5.4b,c) is overall the same as in the previous case but, as friction decreases, non-linear effects like the intensity of the southwestern recirculation and the overshoot of the western boundary current around South Africa, are more evident. Note also that there is a slight shift to the north and east of the recirculation with lower E . The relative change in the maximum velocities of the boundary currents is small, although the velocities of the AC increase to ~ 1 m/s, thus closer to the observed values. The transports of the boundary currents do not show significant changes with E ; only in the AC a transport increase of 4.5 Sv occurs.

5.4.2 Sensitivity experiments

With $H = 250$ m and $E = 6.7 \cdot 10^{-8}$ ($\delta_I/\delta_M \sim 1.5$) the subtropical gyre recirculation is further intensified in the region around 30°S; in particular, small-scale inner recirculations develop in the zonal direction (Fig. 5.5). There is now a stronger westward transport along South Madagascar and the flow in the southern channel turns westward. The latter is probably caused by the AC overshoot around South Africa, which entering the western end of the southern Channel finally dominates over the weak eastward flow there. Inertia induces greater maximum velocities along the AC (1.3 m/s), the SMC (0.75 m/s), and the NMC (0.63 m/s). On the other hand, variations in the Mozambique Channel transport with layer depth are

Model results

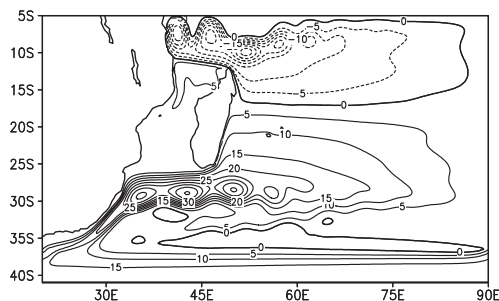


Figure 5.5: *Barotropic stream function for the experiment forced by annual mean winds, with $H = 250$ m and $E = 6.7 \cdot 10^{-8}$. The value of α is as shown in Table 5.1. Contours every 5 units. Units in Sv.*

rather small (Table 5.3). In the most inertial case the transport is about 65% of the linear island rule, while for a layer depth of $H = 1000$ m, the transport is about 75% of the linear estimation, but note that the difference between these actual transports is of the order of 0.5 Sv.

We now consider the case of a wind pattern that resembles that of July (see Fig. 5.2). Using again the continuation technique, steady solutions were followed varying the control parameter α_0 from 1 to 5, so the ratio δ_I/δ_M varies from 1 to 3. Eventually, the extra input of anticyclonic vorticity to the east of Madagascar generates a highly non-linear flow around the island.

The barotropic stream function for different wind stress amplitudes is shown in Fig. 5.6. For realistic winds (Fig. 5.6a), the field is very similar to that obtained with the annual mean pattern (Fig. 5.4a). Due to the northward shift of the trades in July, there is slight northward shift of the subtropical gyre, with the subtropical recirculation located around 30°S in front of the African coast. The AC transport reaches about 30 Sv at this stage (Fig. 5.7a). Interestingly, the ratio between the Mozambique Channel and EMC transports has changed to ~ 1 , so they both exert an equal contribution to the AC flow. The transport of the island's western boundary currents increases linearly with τ_m up to a wind stress amplitude of ~ 0.8 Pa. In particular, for very low amplitudes of the wind stress the Channel's transport is 87% of the linear island rule and for realistic winds it is about 83% of the latter. Fig. 5.7b illustrates in more detail the linear increase of the Mozambique Channel transport lying within 80-90% of the island rule estimate, while for winds larger than $\tau_m \sim 0.8$ Pa the Channel's transport diverges from the linear behavior. At that point, a southwestward tilt in the free jet from south Madagascar to Africa starts to be seen (Fig. 5.6b). The southwestward tilt of the flow from South Madagascar increases with increasing winds, as well as the intensity of recirculation southeast of the island, which is expected to increase the EMC transport. For $\tau_m \sim 1$ Pa, the AC and SMC transports start to decrease (Fig. 5.7a), and the inertial recirculation moves further east into the basin (Fig. 5.6c).

Finally, for winds 5 times larger than the real value the flow pattern (Fig. 5.6.d) shows a recirculation region that is completely situated to the east of Madagascar, with an overshooting western boundary current that connects through the southwestward flowing free-jet with the AC flow along South Africa. The relocation of the inertial recirculation modifies the rela-

Non-linear effects on the circulation around an island, with application to Madagascar

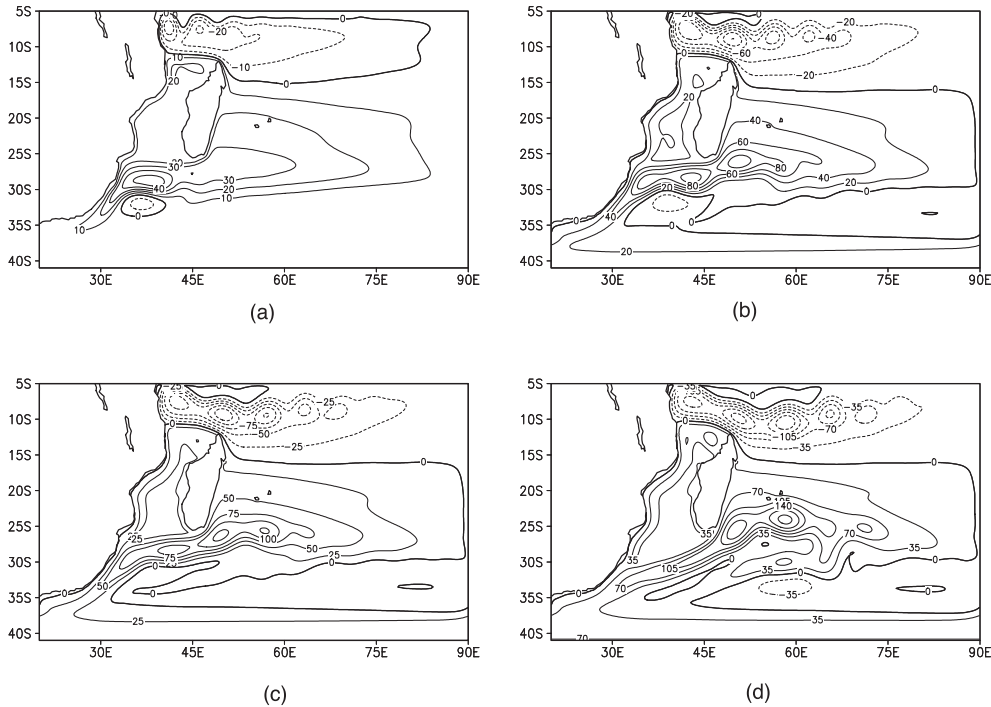


Figure 5.6: Barotropic stream function for the experiment forced by a wind stress with the spatial structure of July and amplitudes equal to (a) 0.33 Pa, which is the maximum amplitude of the observed wind stress, (b) 0.8 Pa, (c) 1 Pa and (d) 1.5 Pa. Contours every 10, 20, 25 and 35 units, respectively. Units in Sv.

tion between the western boundary currents: the EMC has now a transport of 54 Sv, while in the AC (around 30°S) the transport is 34 Sv, although it increases to 56 Sv across a section of 200 km at 33°S. The Mozambique Channel transport reaches 38 Sv, which is $\sim 70\%$ of that predicted by the linear island rule. In general, the basin transports have reached unrealistically high values, specially in the recirculation region. The transport of the boundary currents is quasi-constant after a wind stress of ~ 1.3 Pa; the extra input of vorticity by the wind goes probably to further development of cells in the central basin.

In the Mozambique Channel, the momentum put by the wind induces strong currents along the western boundary, with maximum velocities of 0.7 m/s near the narrows and of 0.2 m/s around 20°S. Maximum velocities of 0.2 m/s were measured in the narrows (Ridderinkhof and De Ruijter, 2003). Strong northward velocities appear in the western side of the central Channel (up to ~ 0.3 m/s) and on the eastern side of the northern anticyclonic loop (up to ~ 0.5 m/s). The NMC and EMC show velocities of ~ 2 m/s near their separation from the coast, while along the free jet towards Africa velocities of ~ 1.5 m/s magnitude are detected. The latter are comparable to measurements of the speed of the AC along the African coast (Pearce and Grndligh, 1982).

Steady solutions with a wind pattern that has the spatial structure of January and varying

Model results

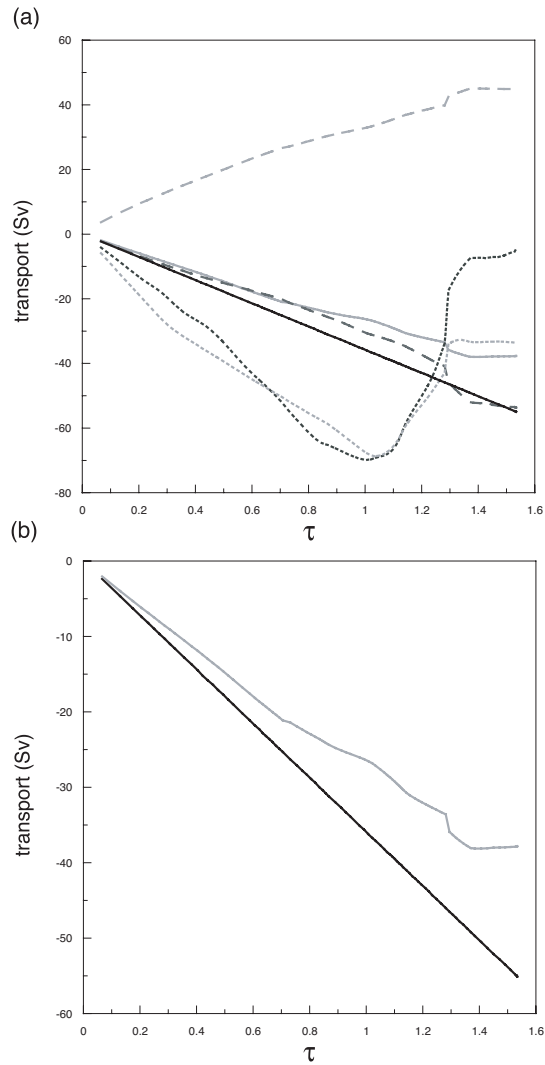


Figure 5.7: (a) Transport of the NMC (grey dashed line), the EMC (dark dashed line), the flow through the Mozambique Channel (solid grey line), the flow from southern Madagascar (dark dotted line), and of the AC (grey dotted line) as a function of July wind stress of varying amplitude (note that here $\tau \equiv \tau_m$). Also shown is the transport predicted by the Island Rule (solid black line). The NMC, EMC, and MC transports increase with increasing winds, while the AC and SMC decrease after a wind stress amplitude of ~ 1 Pa is reached. (b) Enlarged version of (a) for the MC transport (grey line) and Island Rule estimate (black line).

amplitude were also computed. In this case, the winds force a northward transport through the Mozambique Channel (Fig. 5.8a). For $\tau_m \sim 0.22$ Pa the circulation shows a double gyre structure, with a southwestern recirculation and a recirculation region near the northern tip

Non-linear effects on the circulation around an island, with application to Madagascar

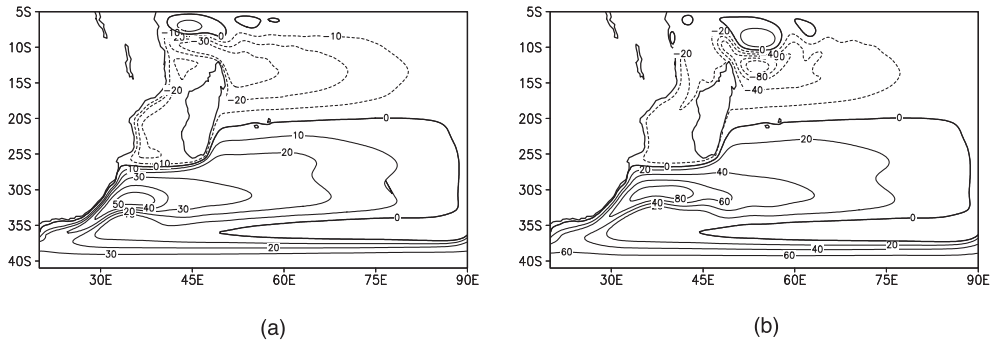


Figure 5.8: Barotropic stream function for the experiment with the spatial pattern of January winds and amplitudes equal to (a) 0.22 Pa, the maximum amplitude of the observed wind stress, and (b) 0.7 Pa. Contours every 10 and 20 units, respectively. Units in Sv.

of Madagascar. Increasing the wind stress amplitude leads to linear increases of the western boundary currents, in particular the transport of the Channel follows within 98% the linear island rule and is about two thirds of the EMC transport (Fig. 5.9). A bifurcation, mostly notable in the NMC transport, occurs at a value of the wind stress $\tau_m \sim 0.5$ Pa, after which the NMC significantly deviates from the earlier linear behavior. The latter is associated with the development of a compact recirculation northeast of the island, while south of Madagascar the flow has basically the same characteristics as before (Fig. 5.8b). For $\tau_m \sim 0.7$ Pa ($\delta_I/\delta_M \sim 2$), the transport of the AC reaches about 70 Sv, that in the NMC is 37 Sv, and the Channel's transport differs in only 0.3 Sv from the Island Rule (Fig.5.9). The solutions could not be followed for values of the parameter τ_m larger than 0.7 Pa because of numerical problems.

5.4.3 Analysis of the island rule

In the above experiments the transport through the Mozambique Channel does not depart significantly from the linear island rule. In particular, the agreement is excellent with January winds, while with the mean and July wind patterns the linear island rule overestimates by -at the most- 30% the actual transport. According to equation (5.8) deviations from the Island Rule appear when the net contributions of friction and non-linear terms are significant compared to the wind contribution. However, the model experiments show that increasing inertia does not alter significantly the Channel's transport or its ratio to the linear estimation. Pedlosky et al. (1997) also found for non-steady flows that the effect of non-linearity on the transport around an island is negligible.

The relative importance of the terms in the momentum equation (5.1a,b) was evaluated from the model fields as transport contributions and is shown in Table 5.4, each row representing the momentum balance integrated along the contour C . Although the balance is satisfied within the model, the approximation of the Coriolis term along the boundaries of the basin and the island western side is not satisfactory for the purpose of this analysis. Specifically, as the Coriolis term is not equal to zero on the boundary, a residual is introduced (shown in

Model results

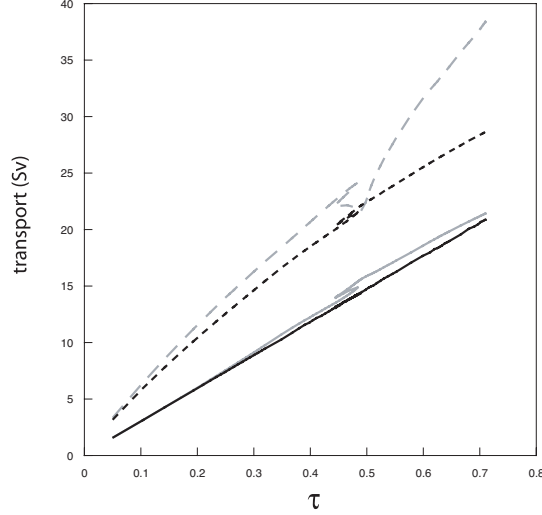


Figure 5.9: Transport of the NMC (long dashed line), the flow through the Mozambique Channel (solid grey line), the Island Rule prediction (black line) and the EMC times a factor -1 (short dashed line) as a function of January winds of varying amplitude (here $\tau \equiv \tau_m$). Note that the realistic wind stress amplitude is $\tau = 0.22$ Pa. Two bifurcations occur around $\tau = 0.5$ Pa, after which the behavior of the NMC departs from the linearity.

the last column of Table 5.4) that when integrated along the meridional and irregular island paths becomes large (i.e. of the order of the other terms). There is also a small residual due to the pressure term that does not exactly equal zero along the closed contour C . This is also taken into account in the term in the last column of Table 5.4. Thus, the first column of Table 5.4 shows the Coriolis term integrated along the zonal section at the island's northern (or southern) latitude; next, the wind, friction and inertia terms are shown. These are expected to be well estimated from the model (i.e. no spurious contributions were detected).

A comparison of the model results between the quasi-linear regime with mean winds ($\delta_I/\delta_M \sim 1$) and the highly-non linear regime with July winds ($\delta_I/\delta_M \sim 3$) shows that in the former the relative importance of inertia with respect to the wind term is larger than in the later. This can be explained by a cancellation between the inertial terms along the northern and southern paths of C in the most non-linear case, giving then a small net contribution.

Case	Coriolis	Wind	Friction	Inertia	Residual
Annual mean	2.5	-3.7	-0.1	0.6	0.7
July	38	-55.1	9.3	2.4	5.4
January	-21.2	21.5	-3	2.4	0.3

Table 5.4: Contribution in Sv of each of the terms in the momentum balance to the circulation integral as shown in equation (5.8). Here the Coriolis term is representing the island stream function, Ψ_I . A residual appears due the approximation of the Coriolis term along the western boundary of the island.

Non-linear effects on the circulation around an island, with application to Madagascar

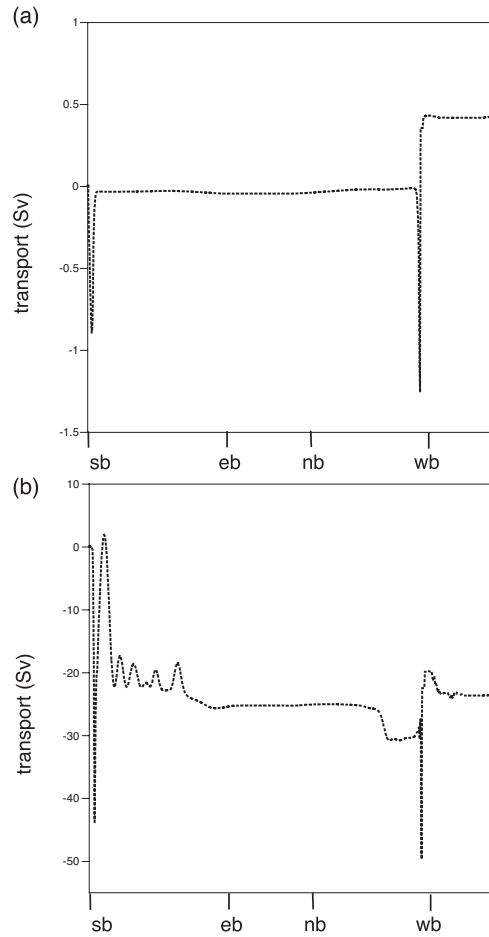


Figure 5.10: Cumulative integral of the relative vorticity flux normal to the contour C for the experiment with (a) annual mean winds and (b) July winds. The x-axis shows schematically the limits of the southern (sb), northern (nb), eastern (eb), and western (wb) paths along C . Units in Sv.

In the other cases, the largest inertial contribution comes from the northern boundary. The inertial term as shown in equation 5.1 a,b includes the advection of relative vorticity across C (the third term in the right hand side of equation (5.8)). An estimate of the cumulative integral of this term along C is shown in Fig. 5.10., with ζ estimated from the model's velocity fields and interpolated into h -grid points. For the reference experiment (Fig. 5.10.a), the integral along the southern boundary is negative on the EMC western flank due southward advection of negative vorticity that tends to be canceled to the east by southward advection of positive vorticity along the eastern flank of the EMC. Along the northern boundary, northward advection of negative vorticity at the NMC eastern flank adds a negative contribution to the integral, but this is offset by advection of positive vorticity on the current's western side. For

Summary and discussion

the most non-linear case with July winds, a large negative contribution to the flux appears along the southern path due to northward advection of positive vorticity in the recirculation region around 50°E (see Fig. 5.6d). This term acting from 50° - 53°E is essential to set the meridional vorticity flux to a large negative value. Further east, the flux oscillates due to the recirculation up to 75°E . On the other hand, the behavior of the NMC near the northern tip is similar to the annual mean, or less non-linear case. This suggests that the meridional vorticity flux along the recirculation region southeast of Madagascar introduces an asymmetry between the mean and July cases that eventually turns the non-linear effects very weak.

Viscous effects are mostly important in the experiment with July winds, inducing a reduction in the Channel's transport of about 10 Sv. The friction term is larger in the northern than in the southern tip of the island, probably caused by the NMC rounding the tip of the island while in the south the EMC separates before interacting with the boundary at that latitude (Fig. 5.6d). With January winds ($\delta_I/\delta_M \sim 2$), there is a good correspondance with the Island Rule, which is in part related to a cancellation between frictional and inertial effects. The transport through the Channel is controlled by the the balance between the advection of planetary vorticity and the vorticity input by the wind, or the Sverdrup balance; the non-linear recirculation in the northeastern tip of the island seems to affect the regime of the NMC itself.

5.5 Summary and discussion

In this study we have investigated steady circulation patterns in the region around Madagascar in the context of a barotropic, shallow water model. The goal was to analyze non-linear effects on the island's boundary current solutions, and in particular, in the transport through the Mozambique Channel. The Island Rule by Godfrey (1989) provides a linear estimate of the transport based on the knowledge of the large-scale wind stress field. In the South Indian Ocean around Madagascar this gives a transport, depending on the wind stress product, between 1.6-3.2 Sv. Recent measurements in the narrows of the Channel indicate a net southward transport of 14 Sv, which seems to be accomplished by eddies (Ridderinkhof and De Ruijter, 2003). The general picture of the circulation around Madagascar is that of a flow largely influenced by non-linear processes. Thus, it is intriguing to analyze to what extent the Island Rule is a valid approximation in this region.

The model experiments forced by annual mean winds and different degrees of lateral friction show relatively good agreement between the Channel's transport and the linear island rule (within 70-80%). Moreover, the flow in the Mozambique Channel is weak (i.e. there is no intense western boundary current), and inertial effects are concentrated in the southwestern recirculation of the subtropical gyre. Using the winds of July, steady solutions show two regimes of behavior according to the amplitude of the wind stress. With realistic winds, the subtropical gyre presents a recirculation cell in the southwestern basin, with two boundary currents flowing westward from the tips of Madagascar towards Africa and a boundary current along the western side of the Mozambique Channel. The East Madagascar Current (EMC) and Channel transports increase linearly with the wind stress amplitude and they contribute equally to the Agulhas Current (AC) flow. In the highly non-linear regime (forced by winds of unrealistic amplitude), the inertial recirculation of the subtropical gyre is found completely to the east of Madagascar. Due to inertia, the EMC overshoots the is-

land's southern boundary and connects through a southwestward jet with the current off South Africa at $\sim 33^\circ\text{S}$. In this regime, the transport through the Channel also deviates in about 30% of the Island Rule. Therefore, the effect of inertia on the Channel's transport is negligible, while friction induces a rather significant decrease in the transport in the high non-linear case. This result is consistent with the experiments of time dependent flows ($\delta_I/\delta_M \sim 1 - 3$) by Pedlosky et al. (1997), who found that increasing non-linearity led to an increase of the frictional boundary layers rather than to a net contribution of inertia through fluxes of relative vorticity. They explained that the vorticity fluxes associated with a western boundary layer of the form $\sim v\partial v/\partial x$ cancel when integrated along the zonal sections between the island and the basin due to the no-slip boundary conditions. In the present experiments, the vorticity fluxes associated with the recirculation region to the east of Madagascar are significant when integrated along the southern contour; probably the mentioned boundary layer approximation is not valid in this case. Still, the net effect of the inertial term in the shallow water model on the basin circulation integral is very weak.

The non-linear behavior of the EMC around South Madagascar is similar to the AC inertial retroreflection regime found in a small basin with high resolution and low Ekman number by Dijkstra and de Ruijter (2001). In that configuration, the inertial overshoot bridges the gap between the western boundary current and the line of zero wind stress curl from where the flow can reconnect with the eastward interior. The results here suggest that an inertial regime south of Madagascar is possible if the winds were 3 to 5 times larger than their real amplitude, although this could be less for lower Ekman number, i.e. one order of magnitude lower. Nevertheless, the lack of an evident overshoot south of Madagascar in the real ocean is not surprising if one compares the intensity of the EMC (~ 0.6 m/s) to that of the AC (1.5 m/s).

Although the inertial regime around Madagascar, in particular the overshoot of the EMC, intensifies significantly for unrealistic amplitudes of the wind stress, a rough comparison with the characteristics of the South Indian Ocean subtropical gyre is suggestive. The upper layer recirculation to the east of Madagascar (Fig. 5.1) is bounded in the south by the eastward flow of the SICC, which is potentially baroclinically unstable (Palastanga et al., 2007). Drifter data at the surface suggest the presence of eddies and meanders along the eastward flow of the SICC near Madagascar, while from altimetry, eddies are suggested to propagate westward along 25°S (Schouten et al., 2002a). These eddy-like features probably converge in the region off the southeastern Madagascars coast, creating a high energy area there (see Fig. 1.6). On the other hand, in the Mozambique Channel there is ample evidence of eddies and eddy-interactions (Schouten et al., 2003). If the real case is close to the flow with high degree of non-linearity from the model experiments, it could be speculated that sensitivities of the EMC jet near its termination point could occur. For example, if instabilities of the SICC grow as to increase the EKE level along 25°S , they may have an impact on the mean recirculation by eddy to mean flow interactions, and then in the behavior of the EMC, e.g. in the tilt of the western boundary current continuation towards the African coast.

Among the advantages of continuation techniques are that they provide a range of steady solutions as a parameter is varied and the linear stability of the latter can be tested (Dijkstra, 2000). Dijkstra and de Ruijter (2001b) found that the instabilities of the Agulhas Current are caused by Rossby basin modes that in turn affect the characteristics of the retroreflection. It could be expected that barotropic instabilities in the western boundary currents around Madagascar introduce variability in the steady states described in Section 5.4. In particular, insta-

Summary and discussion

bilities due to the horizontal shear of the westward jet in the northern Mozambique Channel could cause eddies that may drive, via rectification processes, a non-linear transport in the Channel. Observations show variability at around 7 times/year in the horizontal shear of the North Madagascar Current (Quadfasel and Swallow, 1988), and a reduction of that frequency to 4 to 5 times/year in the central Channel (Schouten et al., 2003). Future studies on the circulation around Madagascar could test this hypothesis regarding the origin of the eddy variability in the Mozambique Channel and the nature of the Channel's flow.

Finally, some of the many simplifications of the model used here have to be remarked. One is the lack of bottom topography that generates an unrealistic adjustment to the wind patterns and unrealistic transports in the recirculations. Both Matano (1999) and Kindle (1991) remarked the important role of meridional barriers in redistributing energy into subbasins. Another limitation in the present model is the lack of baroclinic adjustment. This could be important to the east of Madagascar, where wind anomalies related to the ENSO/IOD modes propagate in the subtropical Indian Ocean on time scales of 1 year. Changes in the island circulation to such interannual wind anomalies have not been studied from a modeling point of view. A particularly important period occurred during the 1998-2001 protracted La Niña. Changes in the circulation around Madagascar were related to the regular formation of dipoles that drifted towards the AC following a straight southwestward path (de Ruijter et al. 2004). Eventually, these anomalies had an impact on the characteristics of the AC retroflection and ring formation. Quantifying interactions between the western boundary currents around Madagascar is important for the variability of the global inter-ocean exchange. The results of this study suggest in a qualitative way that inertial effects are able to introduce significant changes in the EMC regime, and thus in its connection with the AC. More efforts in this direction, for example using eddy resolving multilayer models, are needed.

Bibliography

Allan, R. J., J. A. Lindesay, C. J. C Reason (1995), Multidecadal variability in the climate system over the Indian Ocean region during the austral summer, *J. Climate.*, 8, 1853-1873.

Allan, R. J., D. Chambers, W. Drosowsky, H. Hendon, M. Latif, N. Nicholls, I. Smith, R. Stone, and Y. Tourre (2001), Is there an Indian Ocean dipole and is it independent of the El Niño Southern Oscillation?, *Clivar Exchanges*, 6, 18-22.

Allan, R. J., C. J. C. Reason, J. A. Lindesay, and T.J Ansell (2003), Protracted ENSO episodes and their impacts in the Indian Ocean region, *Deep Sea. Res.*, 50, 2331-2347.

Anderson, D. L. T. and A. E. Gill (1975), Spin-up of a stratified ocean, with application to upwelling, *Deep Sea Res.*, 22, 583-596.

Baquero Bernal, A., M Latif, and S. Legutke (2002), On dipolelike variability of Sea Surface temperature in the tropical Indian Ocean, *J. Climate*, 15, 1358-1368.

Beal, L. M., and H. L. Bryden (1999), The velocity and vorticity structure of the Agulhas Current at 32S, *J. Geophys. Res.*, 104, 5151-5176.

Belkin, I. M., and A. L. Gordon (1996), Southern Ocean fronts from the Greenwich Meridian to Tasmania, *J. Geophys. Res.*, 101, 3675-3696.

Biastoch, A., and W. Krauss (1999), The role of the mesoscale eddies in the source regions of the Agulhas Current, *J. Phys. Oceanogr.*, 29, 2303-2317.

Biastoch, A., C. J. C. Reason, J. R. E. Lutjeharms, and O. Boebel (1999), The importance of flow in the Mozambique Channel to the seasonality in the greater Agulhas system, *Geophys. Res. Lett.*, 26, 3321-3324.

Bjerknes, J. (1966), Atmospheric teleconnections from the equatorial Pacific, *Mon. Wea. Rev.*, 97, 163-172.

Birol, F., and R. Morrow (2001), Source of the baroclinic waves in the southeast Indian Ocean, *J. Geophys. Res.*, 106, 9145-9160.

Birol, F., and R. Morrow (2003), Separation of the quasi-seamannual Rossby waves from the eastern boundary of the Indian Ocean, *J. Mar. Res.*, 61, 707-723.

Broecker, W. S. (1991), *The great ocean conveyor*, *Oceanography*, 4, 79-89.

Chavanne et al., C., P. Flament, R. Lumpkin, B. Dousset, and A. Bentamy (2002), Scatterometer observations of wind variations induced by oceanic islands: Implications for wind driven ocean circulation, *Can. J. Remote. Sens.*, 28 (3), 466-474.

Bibliography

- Chelton, D. B., and M. G. Schlax (1996), Global observations of oceanic Rossby waves, *Science*, 272, 234-238.
- Chelton, D. B., R. A. deSzoeke, M. G. Schlax, K. E. Naggar and N. Siwertz (1998), Geographical variability of the first baroclinic Rossby radius of deformation, *J. Phys. Oceanogr.*, 28, 433-460.
- Chelton, D. B., M. G. Schlax, M. H. Freilich, and R. F. Milliff (2004), Satellite radar measurements reveal short scale features in the wind stress field over the world ocean, *Science*, 303, 978-983.
- Conkright, M.E., R. A. Locarnini, H.E. Garcia, T.D. O'Brien, T.P. Boyer, C. Stephens, J.I. Antonov (2002), *World Ocean Atlas 2001: Objective Analyses, Data Statistics, and Figures, CD-ROM Documentation. National Oceanographic Data Center*, Silver Spring, MD, 17 pp.
- De Ruijter, W.P.M, A. Biastoch, S. S. Drijfhout, J.R.E. Lutjeharms, R. P. Matano, T. Pichevin, P. J. van Leeuwen, and W. Weijer (1999), Indian-Atlantic interocean exchange: dynamics, estimation and impact, *J. Geophys. Res.*, 104, 20,885-20,910.
- De Ruijter, W.P.M, H. Ridderinkhof, J.R.E. Lutjeharms, M.W. Schouten, and C. Veth (2002), Observations of the flow in the Mozambique Channel, *Geophys. Res. Lett.*, 29, 1401-1403.
- De Ruijter, W. P. M., H. M. van Aken, E. J. Beier, J. R. E Lutjeharms, R.P. Matano, and M. W. Schouten (2004), Eddies and dipoles around South Madagascar: formation, pathways and large-scale impact, *Deep Sea Res., part I*, 51, 383-400.
- De Ruijter, W. P. M, H. Ridderinkhof, and M. W. Schouten (2005), Variability of the southwest Indian Ocean, *Philos. Transact. A. Math. Phys. Eng. Sci.*, 363, 63-76.
- De Szoeke, R. A (1987), On the wind driven circulation of the South Pacific Ocean, *J. Phys. Oceanogr.*, 17, 613-630.
- Dijkstra, H. A., and W. P. M. de Ruijter (2001), On the physics of the Agulhas Current: steady retroflection regimes, *J. Phys. Oceanogr.*, 31, 2971-2985.
- Dijkstra, H. A., and W. P. M. de Ruijter (2001b), Barotropic instabilities of the Agulhas Current system and their relation to ring formation, *J. Mar. Res.*, 59, 517-533.
- Dijkstra, H. A (2000), *Non-linear physical oceanography*, Kluwer Academic Publishers, Dordrecht, The Netherlands, 480 pp.
- Di Marco, S., P. Chapman, and W. D. Nowlin Jr. (2000), Satellite observations of upwelling on the continental shelf south of Madagascar, *Geophys. Res Lett.*, 27, 3965-3968.
- Di Marco, S. F., P. Chapman, W. D. Nowlin Jr., P. Hacker, K. Donohue, M. Luther, G. C. Johnson, and J. Toole (2002), Volume transport and property distributions of the Mozambique Channel, *Deep Sea Res., part I*, 49, 1481-1511.
- Donguy, J.R. and B. Piton (1991), The Mozambique Channel revisited, *Oceanology Acta*, 14, 549-558.
- Donohue, K. A., and J. M. Toole (2003), A near-synoptic survey of the Southwest Indian Ocean, *Deep Sea Research*, 50, 1893-1931.

Bibliography

- Duchon, C. E. (1979), Lanczos filtering in one and two dimensions, *J. Applied Meteor.*, *18*, 1016-1022.
- Fang, F., and R. Morrow (2003), Evolution, movement and decay of warm-core Leeuwin Current eddies, *Deep Sea Res., part II*, *50*, 2245-2261.
- Feng M., and G. Meyers (2003), Interannual variability in the tropical Indian Ocean: a two year time-scale of the Indian Ocean dipole, *Deep Sea Res., part II*, *50*, 2263-2284.
- Fu, L-L, and R. A. Davidson (1995), A note on the barotropic response of sea level to time dependent wind forcing, *J. Geophys. Res.*, *100*, 24,995-24,963.
- Fu, L-L (2001), Ocean circulation and variability from satellite altimetry, in *Ocean Circulation and Climate*, Eds. G. Siedler, J. Church and J. Gould, 141-170, Academic Press, London, 715 pp.
- Galanti, E., and E. Tziperman (2003), A midlatitude-ENSO teleconnection mechanism via baroclinically unstable long Rossby waves, *J. Phys. Oceanogr.*, *33*, 1877-1888.
- Gill, A. E., J. S. A. Green, and A. J. Simmons (1974), Energy partition in the large scale ocean circulation and the production of mid-ocean eddies, *Deep Sea Res.*, *21*, 499-528.
- Gill, A. E. (1982), *Atmosphere-Ocean dynamics*, Academic Press, 664 pp.
- Godfrey, J. S. (1989), A Sverdrup model of the depth-integrated flow for the world ocean allowing for island circulations, *Geophys. Astrophys. Fluid Dynamics*, *45*, 89-112.
- Gordon, A. L. (1986), Interocean exchange of thermocline water, *J. Geophys. Res.*, *91*, 5037-5046.
- Gordon, A. L. (1995), WHP Indian Ocean I9N, *International WOCE Newsletter*, No. 20, 26-27 (Unpublished manuscript).
- Gründlingh, M. L. (1995), Tracking eddies in the southeast Atlantic and southwest Indian oceans with TOPEX/POSEIDON, *J. Geophys. Res.*, *100*, 24,977-24,986.
- Harris, T. F. W. (1972), Sources of the Agulhas Current in spring of 1964, *Deep Sea Res.*, *19*, 633-650.
- Hastenrath, S., and S. Greischar (1991), The monsoonal current regimes of the Tropical Indian Ocean: observed surface flow fields and their geostrophic and wind-driven counterparts, *J. Geophys. Res.*, *96*, 12,619-12,633.
- Halliwell, G. R., Jr.G. Peng, and D. B. Olson (1994), Stability of the Sargasso Sea Sub-tropical Frontal Zone, *J. Phys. Oceanogr.*, *24*, 1166-1183.
- Hellerman, S., and M. Rosenstein (1983), Normal monthly wind stress over the World Ocean with error estimates, *J. Phys. Oceanogr.*, *13*, 1093-1104.
- Hermes, J. C. and C. J. C Reason (2005), Ocean model diagnosis of interannual co-evolving SST variability in the South Indian and South Atlantic Oceans, *J. Climate*, *18*, 2864-2882.
- Huang, B., and J. L. Kinter III (2002), Interannual variability in the tropical Indian Ocean, *J. Geophys. Res.*, *107*, 110.1029/2001JC001278.

Bibliography

- Isoguchi, O. and H. Kawamura (1997), A study on the wind driven circulation in the sub-arctic North Pacific using TOPEX/POSEIDON altimeter data, *J. Geophys. Res.*, *102*, 12,457-12,468.
- Johns, W. E. (1988), One dimensional baroclinic unstable waves on the Gulf Stream potential vorticity gradient near Cape Hatteras, *Dyn. Atm. Oc.*, *11*, 323-350.
- Jury, M. R., and B. Huang (2004), The Rossby wave as a key mechanism of Indian Ocean climate variability, *Deep Sea Res., part I*, *51*, 2123-2136.
- Kalnay E, M. Kanamitsu, R. Kistler, W. Collins, D. Deaven, L. Gandin, M. Iredell, S. Saha, C. White, J. Woollen, Y. Zhu, A. Leetmaa, B. Reynolds, C. Chelliah, M. Ebisuzaki, W. Higgins, J. Janowiak, K. C. Mo, C. Ropelewski, J. Wang, R. Jenne, D. Joseph (1996), The NCEP/NCAR 40 Year Reanalysis Project, *Bull. Amer. Meteor. Soc.*, *77*, 437-471.
- Keller, H. B. (1977), *Numerical solution of bifurcation and non-linear eigenvalue problems, Applications of bifurcation theory*, P. H. Rabinowitz, Ed., Academic Press, 359-384.
- Killworth, P. D, D. B. Chelton, and R. A. De Szoeke (1997), The speed of observed and theoretical long extratropical planetary waves, *J. Phys. Oceanogr.*, *27*, 1946-1966.
- Kindle, J. C. (1995), Topographic effects on the seasonal circulation of the Indian Ocean, *J. Geophys. Res.*, *96*, 16,827-16,837.
- Klein, S. A., B. J. Soden, and N-C Lau (1999), Remote sea surface temperature variations during ENSO: evidence for a tropical atmospheric bridge, *J. Climate*, *12*, 917-932.
- Le Blanc, J-L, and J-P Boulanger (2001), Propagation and reflection of long equatorial waves in the Indian Ocean from TOPEX/POSEIDON data during the 1993-1998 period, *Ocean Dyn.*, *17* 547-557.
- Lighthill, M. J. (1969), Dynamic response of the Indian Ocean to the onset of the Southwest monsoon, *Phil. Trans. R. Soc. A*, *265*, 45-92.
- Lipps, F. B. (1963), Stability Jets in a Divergent Barotropic Fluid, *J. Atm. Sc.*, *20*, 120-129.
- Liu, Z., L. Wu, and H. Hurlburt (1999), Rossby wave-Coastal Kelvin wave interaction in the extratropics. Part II: Formation of island circulation, *J. Phys. Oceanogr.*, *29*, 2505-2418.
- Lutjeharms, J. R. E. (1976), The Agulhas Current system during the northeast monsoon season, *J. Phys. Oceanogr.*, *6*, 665-670.
- Lutjeharms, J. R. E., N. D. Bang, C. P. Duncan (1981), Characteristics of the currents east and south of Madagascar, *Deep Sea Res.*, *9*, 879-899.
- Lutjeharms, J. R. E. (1988), Remote sensing corroboration of the retroreflection of the East Madagascar current, *Deep Sea Res.*, *35*, 2045-2050.
- Lutjeharms, J. R. E, and E. Machu (2000), An upwelling cell inshore of the East Madagascar Current, *Deep Sea Research, part I*, *47*, 2405-2411.
- Lutjeharms, J. R. E. (2006), *The Agulhas Current*, Springer-Verlag, Berlin, 330 pp.
- Matano, R. P., C. G. Simionato, and P. T. Strub (1999), Modeling the wind driven variability of the South Indian Ocean, *J. Phys. Oceanogr.*, *29*, 217-230.

Bibliography

- Masumoto, Y., and G. Meyers (1998), Forced Rossby waves in the southern tropical Indian Ocean, *J. Geophys. Res.*, *103*, 27589-27602.
- Meyers, G. (1996), Variation of Indonesian throughflow and the El Niño Southern Oscillation, *J. Geophys. Res.*, *101*, 12,255-12,263.
- Morrow, R., and F. Birol (1998), Variability in the southeast Indian Ocean from altimetry: forcing mechanisms for the Leeuwin Current, *J. Geophys. Res.*, *103*, 18,529-18,544.
- Murtugude, R., A. J. Busalacchi, and J. Beauchamp (1998), Seasonal to interannual effects of the Indonesian Throughflow on the tropical Indo-Pacific basin, *J. Geophys. Res.*, *103*, 21,425-21,441.
- Murtugudde, R., J. P. McCreary Jr., and A. J. Busalacchi (2000), Oceanic processes associated with anomalous events in the Indian Ocean with relevance to 1997-1998, *J. Geophys. Res.*, *105*, 3295-3306.
- Nicholson, S. E. (1997), An analysis of the ENSO signal in the tropical Atlantic and western Indian oceans, *Int. J. Climatology*, *17*, 345-375.
- North, G. R., T. L. Bell, and R. F. Cahalan (1982), Sampling errors in the estimation of empirical orthogonal functions, *Am. Met. Soc.*, *110*, 699-706.
- Palastanga, V., P. J. van Leeuwen, and W. P. M. de Ruijter (2006), A link between low-frequency mesoscale eddy variability around Madagascar and the large-scale Indian Ocean variability, *J. Geophys. Res.*, *111*, 10.1029/2005JC003081.
- Palastanga, V., P. J. van Leeuwen, M. W. Schouten, and W. P. M. de Ruijter (2007), Flow structure and variability in the subtropical Indian Ocean: Instability of the South Indian Ocean Countercurrent, *J. Geophys. Res.*, *112*, 10.1029/2005JC003395.
- Pedlosky, J. (1987), *Geophysical Fluid Dynamics*, Springer-Verlag, New York, 710 pp.
- Pedlosky, J., L. J. Pratt, M. A. Spall, and K. R. Helfrich (1997), Circulation around islands and ridges, *J. Mar. Res.*, *55*, 1199-1251.
- Penven, P., J. R. E. Lutjeharms, and P. Florenchie (2006), Madagascar: a pacemaker for the Agulhas Current system?, *Geophys. Res. Lett.*, *33*, 10.1029/2006GL026854.
- Perigaud, C., and P. Delecluse (1992), Annual sea level variations in the Southern Tropical Indian Ocean from Geosat and shallow water simulations, *J. Geophys. Res.*, *97*, 20,169-20,178.
- Perigaud, C., and P. Delecluse (1993), Interannual sea level variations in the Tropical South Indian Ocean from Geosat and shallow water simulations, *J. Phys. Oceanogr.*, *23*, 1916-1934.
- Philander, S. G. H. (1976), Instabilities of zonal equatorial currents, *J. Geophys. Res.*, *81*, 3725-3735.
- Philander, S. G. H. (1990), *El Niño, La Niña, and the Southern Oscillation*, Academic Press, San Diego, 293 pp.
- Phillips, N. A. (1954), Energy transformations and meridional circulations associated with simple baroclinic waves in a two-level, quasi-geostrophic model, *Tellus*, *6*, 273-286.

Bibliography

- Qiu, B. (1995), Variability of the energetics of the Kuroshio extension and its recirculation gyre from the first two-year of TOPEX data, *J. Phys. Oceanogr.*, *25*, 1827-1842.
- Qiu, B., A. Koh, C. Lumpkin, and P. Flannet (1997), Existence and formation mechanisms of the North Hawaiian Ridge Current, *J. Phys. Oceanogr.*, *27*, 431-444.
- Qiu, B. (1999), Seasonal eddy field modulation of the North Pacific Subtropical Countercurrent: TOPEX/Poseidon observations and theory, *J. Phys. Oceanogr.*, *29*, 2471-2486.
- Qiu, B. (2002), Large-scale variability in the midlatitude subtropical and subpolar North Pacific Ocean: observations and causes, *J. Geophys. Res.*, *32*, 353-375.
- Qiu, B., and S. Chen (2004), Seasonal modulations in the eddy field of the South Pacific Ocean, *J. Phys. Oceanogr.*, *34*, 1515-1527.
- Quadfasel, D. R., and J. C. Swallow (1986), Evidence for 50-day period planetary waves in the South Equatorial Current of the Indian Ocean, *Deep Sea Res.*, *33*, 1307-1312.
- Quarty, G. D. and Srokosz M. A. (2004), Eddies in the Southern Mozambique Channel, *Deep. Sea Res., part II*, *51*, 69-83.
- Rao, S. A., S. K Behera, Y. Masumoto, and T. Yamagata (2002), Interannual subsurface variability in the tropical Indian Ocean with a special emphasis on the Indian Ocean dipole, *Deep Sea Res., part II*, *49*, 1549-1572.
- Reason, C.J.C., R.J. Allan, J.A. Lindesay, and T.J. Ansell (2000), ENSO and climatic signals across the Indian Ocean basin in the global context: Part I, Interannual composite patterns, *Int. J. Climatology.*, *20*, 1285-1327.
- Reason, C. J. C. and J. R. E Lutjeharms (2000), Modelling multidecadal variability in the South Indian Ocean region: local forcing or a near global mode?, *South Afr. J. Sc.*, *96*, 127-135.
- Reason, C. J. C. (2001), Subtropical Indian Ocean SST dipole events and the southern African rainfall, *Geophys. Res. Lett.*, *28*, 2225-2227.
- Reid, J.L., (2003), On the total geostrophic circulation of the Indian Ocean: flow patterns, tracers, and transports, *Progress in Oceanography*, *56*, 137-186.
- Richman, M. B. (1986), Rotation of Principal Components. *J. Climatology.*, *6*, 293-335.
- Ridderinkhof, H., and W. P. M. de Ruijter (2003), Moored current observations in the Mozambique Channel, *Deep Sea Res., part II*, *50*, 1933-1955.
- Rio, M.-H and F. Hernandez (2004), A Mean Dynamic Topography computed over the world ocean from altimetry, in-situ measurements and a geoid model. *J. Geophys. Res.*, *109*, 10.1029/2003JC002226.
- Ropelewski, C. F. and M. S. Halpert (1987), Global and regional scale precipitation patterns associated with the El Niño/Southern Oscillation, *Mon. Wea. Rev.*, *115*, 1606-1626.
- Saji, N.H., B. M. Goswami, P.N. Vinayachandran (1999), A dipole mode in the tropical Indian Ocean, *Nature*, *401*, 360-363.
- Saji, N. H and T. Yamagata (2003), Structure of SST and surface wind variability during Indian Ocean dipole mode events: COADS observations, *J. Climate.*, *6*, 2735-2751.

Bibliography

- Sakova, I. V., G. Meyers, and R. Coleman (2006), Interannual variability in the Indian Ocean using altimeter data and IX1-expendable bathy-thermograph (XBT) data: does the 18-month signal exist?, *Geophys. Res. Lett.*, *33*, 10.1029/2006GL027117.
- Schott, F., M. Fieux, J. Kindle, J. Swallow, and R. Zantopp (1988), The boundary currents East and North of Madagascar II. Geostrophic Direct measurements and model comparisons, *J. Geophys. Res.*, *93*, 4963-4974.
- Schott, F.A., and J. P. McCreary Jr. (2001), The monsoon circulation of the Indian Ocean, *Progress in Oceanography*, *51*, 1-123.
- Schouten, M. W., W. P.M de Ruijter, P.J. van Leeuwen, and J. R. E. Lutjeharms (2000), Translation, decay and splitting of the Agulhas rings in the south-east Atlantic ocean, *J. Geophys. Res.*, *105*, 21,913-21,925.
- Schouten, M. W., W. P.M de Ruijter, and P.J. van Leeuwen (2002a), Upstream control of Agulhas ring shedding, *J. Geophys. Res.*, 10.1029/2001JC000804.
- Schouten, M. W., W. P.M de Ruijter, and P.J. van Leeuwen, and H. Dijkstra (2002b), A teleconnection between the equatorial and southern Indian Ocean, *Geophys. Res. Lett.*, *107*, 10.1029/2001GL014542.
- Schouten, M. W., W. P.M de Ruijter, P.J. van Leeuwen, and H. Ridderinkhof (2003), Eddies and variability in the Mozambique Channel, *Deep Sea Res., part II*, *50*, 1987-2003.
- Siedler, G., M. Rouault, and J. R. E. Lutjeharms (2006), Structure and origin of the subtropical South Indian Ocean countercurrent, *Geophys. Res. Lett.*, *33*, 10.1029/2006GL027399.
- Slingo, J., H. Spencer, B. Hoskins, P. Barrisford, and E. Black (2005), The meteorology of the western Indian Ocean, and the influence of the East African Highlands, *Phil. Trans. R. Soc. A*, *363*, 25-42.
- Song, Q, A. L. Gordon, and M. Visbeck (2004), Spreading of the Indonesian Throughflow in the Indian Ocean, *J. Phys. Oceanogr.*, *34*, 772-792.
- Stammer, D. (1997), Global characteristics of ocean variability estimated from regional TOPEX/POSEIDON altimeter measurements, *J. Phys. Oceanogr.*, *27*, 1743-1769.
- Stramma, L. (1992), The South Indian Ocean Current, *J. Phys. Oceanogr.*, *22*, 421-430.
- Stramma, L., and J. R. E. Lutjeharms (1997), The flow field of the subtropical gyre of the South Indian Ocean, *J. Geophys. Res.*, *102*, 5513-5330.
- Sverdrup, H. U. (1947), Wind driven currents in a baroclinic ocean, with application to the equatorial currents of the eastern Pacific, *Proceedings of the National Academy of Science*, *33 (11)*, 318-326.
- Swallow, J., M. Fieux, and F. Schott (1988), The boundary currents East and North of Madagascar I. Geostrophic currents and transports, *J. Geophys. Res.*, *93*, 4951-4962.
- Takeuchi, K. (1986), Numerical study of the seasonal variations of the Subtropical Front and the Subtropical Countercurrent, *J. Phys. Oceanogr.*, *16*, 919-926.
- Talley, L. D., and M. O. Baringer (1997), Preliminary results from WOCE hydrographic sections at 80E and 32S in the Central Indian Ocean, *Geophys. Res. Lett.*, *24*, 2789-2792.

Bibliography

- Tchernia, P., (1980), *Descriptive Regional Oceanography*, Pergamon Mar. Ser., (3), Pergamon Press, 253 pp.
- Tourre, Y. M., and W. B. White (1995), ENSO signals in global upper ocean temperature, *J. Phys. Oceanogr.*, *25*, 1317-1332.
- Van Leeuwen, P. J., W. P. M. de Ruijter and J. R. E. Lutjeharms (2000), Natal pulses and the formation of Agulhas ring, *J. Geophys. Res.*, *105*, 6425-6436.
- Verschell, M. A., J. C. Kindle, and J. J O'Brien (1995), Effects of the Indo-Pacific through-flow on the upper tropical Pacific and Indian Oceans, *J. Geophys. Res.*, *100*, 18,409-18,420.
- Webster, P. W., A. M. Moore, J. P. Loschnigg and R. R. Leben (1999), Coupled ocean-atmosphere dynamics in the Indian Ocean during 1997-98, *Nature*, *401*, 356-360.
- White, W. B. (2000), Coupled Rossby waves in the Indian Ocean on interannual time scales, *J. Phys. Oceanogr.*, *30*, 2972-2988.
- Woodberry, K. E., M. E. Luther and J. J O'Brien (1989), The wind driven seasonal circulation in the Southern Tropical Indian Ocean, *J. Geophys. Res.*, *15*, 17,985-18,002.
- Wunsch, C., and D. Stammer (1995), The global frequency-wavenumber spectrum of oceanic variability estimated from TOPEX/POSEIDON altimetric measurements, *J. Geophys. Res.*, *100*, 24,895-24,910.
- Wyrtki, K. (1971), *Oceanographic Atlas of the Interanational Indian Ocean Expedition*, Nat. Sci. Found. Washington D. C., 531 pp.
- Wyrtki, K. (1973), An equatorial Jet in the Indian Ocean, *Science*, *81*, 262-264.
- Wyrtki, K. (1987), Indonesian Throughflow and the associated pressure gradient, *J. Geophys. Res.*, *92*, 12,941-12,946.
- Xie, S. P., H. Annamalai, F. A. Schott, and J. P. Mc Creary Jr. (2002), Structure and mechanisms of South Indian Ocean climate variability, *J. Climate*, *15*, 864-878.

Summary

The eddy variability around Madagascar is probably a control factor for the variability of the Agulhas Current Retroflexion South of Africa and for the shedding of Agulhas rings. Agulhas rings carry relatively warm and salty water from the Indian Ocean into the South Atlantic as part of the warm water route of the global ocean thermohaline circulation (THC) that returns North Atlantic Deep Water (NADW) to the North Atlantic. The frequency of ring shedding South of Africa is related to the propagation of sea surface height (SSH) anomalies from the upstream sources of the Agulhas Current, namely the Mozambique Channel and East Madagascar Current (EMC), at a frequency of 4 to 5 times per year. In turn, the variability in the latter two regions is connected to the large-scale Indian Ocean variability along the latitude bands of the northern and southern tips of Madagascar. In the high frequency or subannual range, variability at 4 to 5 times per year was detected along both bands in the form of westward propagating Rossby waves. By interaction with local currents and eddies these waves might induce the high-frequency variability observed in the eddy activity around Madagascar. The variability along the 12°S band is also connected to interannual subtropical Rossby waves forced in the central eastern Indian Ocean by wind stress curl anomalies due to both El Niño/Southern Oscillation (ENSO) and the Indian Ocean Dipole (IOD) modes. The subtropical Rossby waves seem to control the variability in the thermocline ridge over the western Indian Ocean between 5°-12°S, and are essential for the reverse of the IOD phase. However, the impact of the subtropical SSH anomalies on the circulation around Madagascar has not been studied. Analysis of hydrographic and altimetry data revealed interannual variability in the eddy activity of the Mozambique Channel and South Madagascar regions that could be connected to large-scale SSH anomalies from the tropical climate modes. In particular, a period of frequent vortex pair or dipole formation south of Madagascar appeared after the large 1997-1998 ENSO/IOD event. The train of dipoles in 2000 exhibited a straight south-westward propagation towards the Agulhas Current leading to an anomalous eastward shift of the Agulhas Retroflexion and an interruption in the formation of Agulhas rings that lasted almost half a year. Understanding the connections between the large-scale Indian Ocean variability and the eddy-field around Madagascar is ultimately important for monitoring the variability of the Indian-Atlantic interocean exchange.

This thesis investigates the impact of interannual SSH anomalies from the IOD or ENSO on the currents around Madagascar, and subsequently on the low frequency eddy variability in the Mozambique Channel and South Madagascar regions. For this purpose, altimetry data from the combined Topex-Poseidon (T/P)-ERS data set available for the period 1993-2003 are used. The analysis is complemented by an investigation of the spatial and temporal

Summary

structures of low frequency wind stress curl variability in the South Indian Ocean based on three different wind stress data sets, i.e. NCEP Reanalysis, ERS and QuickSCAT winds measured from satellite scatterometers. In this thesis the causes of high frequency variability (i.e. 4-5 times/year) along the 25°S band in the subtropical Indian Ocean are also investigated. Due to the limited amount of hydrographic data in the center of the Indian Ocean subtropical gyre, relatively little is known about the vertical structure of the large-scale subtropical currents. Therefore, an analysis of the vertical shear of the mean flow along 25°S, and its stability, is performed using the available hydrographic data from climatology and from a synoptic section along 80°E. Thereafter, these can be compared to the characteristics of the eddy variability along 25°S as derived from satellite altimetry.

Due in part to the large eddy variability, knowledge of the mean flow patterns around Madagascar has not been straightforward. For instance, only quite recently hydrographic observations in the narrows of the Mozambique Channel indicated a flow composed by southward propagating anticyclonic eddies, with no intense boundary current along the Channel's western side. On the other hand, observations of the EMC are still limited, and several regimes are accepted at the separation of the EMC from the coast, including an eastward retroflexion with possible eddy shedding. Because of the high non-linearity in this area it is unclear to what extent linear estimates of the transport through the Mozambique Channel (i.e. the linear island rule) are adequate. This question as well as the sensitivity of steady circulation patterns to non-linear effects are addressed within a shallow water model in the last part of this thesis.

The wind stress curl over the Indian Ocean shows unique seasonal changes due to the influence of the Indian monsoon. As previous analysis of the wind stress curl in the Indian basin did not extend further south than 30°S, we start with a description of the seasonal distribution of the wind stress curl over the South Indian Ocean from both NCEP and ERS winds. The curl patterns are consistent with the seasonal changes of the large-scale currents in the Tropical Indian Ocean, and suggest a slight northward shift of the South Equatorial Current (SEC) in boreal summer. To study the curl variability around Madagascar, we use high-resolution QuickSCAT winds. The latter reveals a curl dipole northwest of the island, which develops at the onset of the southwest monsoon and lasts the following two seasons. Around South Madagascar, the curl is cyclonic throughout the year, which might be favorable for upwelling. To analyze the low-frequency curl variability an empirical orthogonal function (EOF) analysis was applied to the low pass filtered curl anomalies from 50 years of NCEP data. The variance explained by the first three EOFs is rather low, probably due to noise in the curl field and/or to the relatively coarse resolution of NCEP data. A rotation analysis of the EOFs shows that the centers of action of the three leading modes are robust features in the basin. The first mode is associated with quasi-biennial variability and suggests large-scale changes in the strength of the subtropical anticyclone. However, we could not determine the forcing of this mode in the basin. The second mode is related to the IOD and ENSO forcing, with spectral peaks at periods of 3 and 2 years. It displays centers of action off the coast of Sumatra (cyclonic) and in the central-eastern South Indian Ocean (anticyclonic) associated with a positive IOD/ENSO event. The third mode is connected to both normal and protracted La Niña events, thus in addition to interannual, interdecadal variability in this signal is expected. Its spatial pattern describes a large-scale cyclonic anomaly (e.g. negative curl during La Niña events) to the east of Madagascar and in the Mozambique Channel. The structure

Summary

of this mode suggests changes in the latitude position of the SEC, or in other words, in the latitude extension of the tropical and subtropical gyres.

To investigate the connection between the interannual variability in the mesoscale eddy activity around Madagascar and the large-scale Indian Ocean variability, a lagged correlation analysis between low pass filtered basin SSH and an IOD index was performed. The analysis shows large-scale SSH anomalies propagating westward along 10° - 15° S in response to the IOD interannual forcing in the east. Positive (negative) SSH anomalies are further intensified by local wind curl anomalies, and arriving at the coast of Madagascar they induce a weakening (strengthening) in the intensity of the SEC. A significant interannual oscillation in the SSH of the Mozambique Channel and East Madagascar regions also appears. The response of the flow around Madagascar to the large-scale SSH was studied in more detail by computing geostrophic velocity anomalies from satellite tracks across the SEC and its branches at the Madagascar and African coasts. Analysis of the current variability suggests a strengthening and shift to the north of the subtropical gyre during a positive IOD event, and an intensification and southward extension of the tropical gyre during a negative IOD event. In turn, velocity anomalies in the narrows of the Mozambique Channel show significant interannual variability consistent with the large-scale circulation anomalies to the east of the island in agreement with the Island Rule. In response to the current and SSH low frequency variability, the eddy kinetic energy (EKE) in the central Mozambique Channel shows a significant interannual variation. Two processes are proposed that can explain this signal. First, interaction between anticyclonic eddies propagating southward from the northern part of the Channel and the currents in the narrows tends to strengthen (weaken) the eddy-amplitudes. Second, existing anticyclonic eddies merge with other large-scale SSH anomalies in the Channel inducing growth (destruction) of the eddy features. Thus, periods of large (low) EKE coincide with energetic (weak) eddies connected to positive (negative) SSH anomalies of the IOD phases. The response of the eddy activity south of Madagascar to the large-scale tropical SSH anomalies is less clear. Only during the 1997 IOD/ENSO event the weakening in the EMC appears related with a decrease in the eddy activity downstream. Nevertheless, the variability around South Madagascar seems to be affected by variability along the 25° S Indian Ocean band and by midlatitude's variability maybe connected to the subtropical gyre's recirculation. In addition, during protracted La Niña events as that in 1998-2001 large-scale negative wind stress curl anomalies to the east of Madagascar may force circulation anomalies in this region, e.g. a southward shift in the SEC southern branch. In particular, these negative curl anomalies enhanced the amplitude of the large-scale SSH arriving at the coast of Madagascar in late 1999-2000, and contributed to the forcing of Rossby waves in the central basin in 2000-2001. Therefore, the extreme response in the eddy activity in the Mozambique Channel in 2000-2001 (i.e. a period of very weak eddies) is related to La Niña. On the other hand, although the causes of dipole formation south of Madagascar have not been clarified, it seems that their propagation towards the Agulhas Current in 2000, and thereafter their impact on the Agulhas retroreflection, were influenced by the absence of large anticyclonic eddies from the Mozambique Channel during that period.

To clarify the origin of the eddy variability in the 25° S band of the Indian Ocean we investigated the vertical structure of the mean flow between 20° - 30° S. Analysis of climatological data shows an anticyclonic surface circulation to the east of Madagascar bounded to the south by an eastward flow extending from southwest Madagascar to 95° E, and to the north by the

Summary

westward flowing SEC. The shallow, eastward flowing current, named here the South Indian Ocean Countercurrent (SICC), extends in the upper 300 m above the deep reaching SEC, with its core along the latitude of the high variability band. The structure of the SICC-SEC in the upper 1000 m is also observed from synoptic hydrographic data along 80°E . To study the stability of the SICC-SEC system, a 2-layer model and parameters derived from hydrographic data were used. It is found that regions of large vertical shear along 25°S are baroclinically unstable, with growth rates of about 80 days, frequencies of 3.5 to 6 times/year and wavelenghts between 290-470 km. These parameters correspond well with observations of the mesoscale variability derived from altimetry data along 25°S . Wavefrequency spectra of the high passed SSH shows a dominant frequency of 4 to 5 times/year in the center of the basin near 80°E . Moreover, the dominant spatial scale of eddy variability estimated from SSH wavenumberspectra (~ 400 km) is close to the first baroclinic Rossby radius of deformation, which suggests that baroclinic instability is a main cause of eddy formation. In conclusion, it is likely that Rossby wave variability locally generated in the subtropical South Indian Ocean by baroclinic instability of the SICC-SEC system is the origin of the eddy variability around 25°S .

The effect of non-linearity on the western boundary currents around Madagascar and on the transport through the Mozambique Channel was examined with a barotropic shallow water model. Using continuation techniques, the non-linearity in the flow is increased by increasing the amplitude of the wind stress. Solutions with different wind stress patterns, layer depths, and friction coefficient were analyzed. The analytical island rule states that for a steady state deviations from the linear Island Rule arise from the net contributions of the inertial and viscous terms integrated along a contour that connects the island's western boundary and the basin eastern boundary. With the wind pattern of July for both a solution with moderate degree of non-linearity and a very non-linear solution, the transport through the Channel is about 70% of the linear estimation, indicating that the net effect of inertia on the Channel's flow is negligible. The experiments also show that friction induces a moderate deviation from the linear island rule, and overall the latter gives a good approximation of the Channel's transport. In addition, in the highly non-linear regime the EMC shows an overshoot at the tip of South Madagascar that connects with an inertial recirculation region to the east of Madagascar and resembles previous barotropic model simulations of the Agulhas retroflection . With January winds the agreement between the Island Rule and the transport through the Channel lies within 98%. Although in a high non-linear case an inertial recirculation is present to the northeast of the island associated with the boundary current separation, the net effect of inertia and friction cancel each other validating the linear estimation of the Channel's transport.

Hartelijk bedankt!

First of all, I would like to thank my supervisor, Will de Ruijter, who offered me this PhD position when I was still a student in Argentina. Without his guidance, unfailing encouragement and patience the present work could not have been accomplished. Working at IMAU has enabled me to develop many professional skills, while the experience of living in the Netherlands, in a culture quite different than mine, has helped me to grow a lot as a person. Will, I will always be grateful to you for making it all possible.

I am very grateful to Peter Jan van Leeuwen, who assisted me with my daily problems and corrected my manuscripts. Many thanks also to Henk Dijkstra for his motivation and enthusiasm during several stages of this thesis, and special thanks for providing the model I used in Chapter 5. I particularly enjoyed the discussions with Will, Henk and Peter Jan about this last Chapter. I also thank Huib de Swart for his constructive comments in the large group meetings and corrections of a late version of this thesis.

Many of my colleagues at IMAU have largely contributed to the building up of this thesis. Mathijs, thank you very much for your interest, help with the altimetry data, and fruitful comments over this study. Femke, it was really nice that I could always ask you about my problems with Fortran and NetCDF, many thanks for your help. Janine, thanks for your help with the WOCE data, Matlab files and for your interest in discussing our results. I also thank Arjen, who has patiently answered my questions about the shallow water model during the last months.

I would like to thank many other people at IMAU for their help and nice atmosphere around: Inge, Yvonne, Marcel, Anna, Carlijn, Carina, Lianke, and all the people of the Oceans and Climate group, thank you. Leela and Mihaela, it was very nice to share the office with you in the last months, and Leela many thanks for correcting my English writing!

I also wish to acknowledge my professors in Argentina, Alberto Piola and Carolina Vera, for all their support during my MSc studies and for an invitation to work at Centro de Investigaciones del Mar y de la Atmosfera (CIMA) in July 2004.

My life in Utrecht -since September 2002- would not have been possible without the help, company, fun and friendship of many wonderful people I could meet during this time. Great, great thanks to XuQuan, Victoria, Mark, Remke, Marietta, Olga, Alberto, Edyta, Fernando, Julia, Sebastian, Ana, Jonatan, Klaus, Thijs, Victor, Ruben, Geertje, Olivier, Philip, Andriy, Dimos, and Jan.

My friends in Argentina: Ines, Constanza, Eugenia, Mariana, Josefina, Ana Julia and Virna, you are a big treasure. Thank you for keeping in touch in all possible ways during these years and for the going out marathons in my visits to Buenos Aires!

Hartelijk bedankt!

Mama y papa, without your constant love and support I could not have gone through the difficult times. Thank you for the respect and freedom that you always gave me, I am happy to say that this large distance has brought us closer. Tomas, you are always there; thanks to you, Rosa and Ignacio for the care, love, and all the nice moments in every trip I did.

Finally, thanks to you Ragnar, for your love and understanding that have meant so much to me during the last months of this PhD.

Curriculum Vitae

Virginia Palastanga was born on 7 January 1977 in Buenos Aires, Argentina. In 1994 she graduated from secondary school. The next year she entered the University of Buenos Aires to study Medicine. Motivated by the first courses in physics and mathematics at university, she decided to study Physical Oceanography, which she graduated after defending her Master's thesis in 2002. The master research was performed under a fellowship from the University of Buenos Aires and supervised by Dr. Carolina Vera. After her master, she continued to collaborate with Dr. Vera at Centro de Investigaciones del Mar y de la Atmosfera (CIMA). During that period she worked as teacher assistant at the Department of Atmosphere and Ocean Sciences of the University of Buenos Aires. In September 2002 she started her PhD at the IMAU (Institute for Marine and Atmospheric research, Utrecht) on the oceanic variability around Madagascar, under the supervision of Prof. Will de Ruijter. She attended a summer school (Switzerland), conferences (Nice, Vienna, Hawaii), and participated in a cruise trip to the Mozambique Channel. The main results of the research carried during 4 and half years at IMAU are described in the present thesis.

